Spring 2019

# Receiver function investigations of mantle transition zone and crustal structure in East Africa and Northeast Asia

Muchen Sun



Department: Geosciences and Geological and Petroleum Engineering

# RECEIVER FUNCTION INVESTIGATIONS OF MANTLE TRANSITION ZONE AND CRUSTAL STRUCTURE IN EAST AFRICA AND NORTHEAST ASIA

by

MUCHEN SUN

A DISSERTATION

Presented to the Faculty of the Graduate School of the

MISSOURI UNIVERSITY OF SCIENCE AND TECHNOLOGY

In Partial Fulfillment of the Requirements for the Degree

DOCTOR OF PHILOSOPHY

in

GEOLOGY AND GEOPHYSICS

2019

Approved by:

Stephen S. Gao, Advisor
Kelly H. Liu, Co-advisor
Marek Locmelis
David Wronkiewicz
Xiaofei Fu

## PUBLICATION DISSERTATION OPTION

This dissertation consists of the following four articles, formatted in the style used by the Missouri University of Science and Technology:

Paper I: Pages 4-28 have been published by Geophysical Research Letters.

Paper II: Pages 29-58 have been published by Earth and Planetary Science Letters.

Paper III: Pages 59-88 are intended for submission to Earth and Planetary Science Letters.

Paper IV: Pages 89-112 have been submitted to Geophysical Research Letters.

## ABSTRACT

In spite of numerous geophysical studies have been conducted in East Africa and Northeast Asia, the structure and evolution of the crust, upper mantle, and the mantle transition zone (MTZ) are still controversial. The MTZ discontinuities beneath the study area are imaged by stacking an unprecedented volume of receiver functions (RFs). The normal MTZ thickness beneath the Western Branch of the EARS and Tanzania Craton indicates the absence of present-day thermal upwelling from the lower mantle. In contrast, beneath the Eastern Branch, a significant MTZ thinning reveals the existence of thermal upwelling from either the upper MTZ or the lower mantle. A normal MTZ thickness beneath southern Africa and the negligible disparity of the mean MTZ thicknesses between on and off cratonic regions suggest the absence of thermal influence from the African Superswell and cratonic keels on the MTZ beneath southern Africa. The major volcanoes in northeast China are underlain by a thickened MTZ, which can be interpreted by an anomalously high-water concentration in the MTZ released from the stagnated slab. An abnormally thin MTZ beneath the Hangay Dome suggests the possible existence of thermal upwelling from the lower mantle.

Additionally, the crustal structure in the Malawi Rift Zone (MRZ) has been investigated using RFs and gravity modeling. The small crustal stretching factor is consistent with the general absence of volcanism in the MRZ. The high $V_p/V_s$ beneath the southern MRZ may indicate the existence of partial melting. Abnormally low $V_p/V_s$ along the western boundary of the MRZ may be related to the $CO_2$ suffusion of rift boundary faults.

# ACKNOWLEDGMENTS

I would like to express my sincere gratitude to my advisor, Dr. Stephen S. Gao. He is always open to discussions at any time, which helps me to think deeply into research topics and enrich my knowledge. He has shown me, by his example, what a good professional researcher should be.

I am especially indebted to Dr. Kelly H. Liu, my co-advisor. I have learned how to be an optimistic, strong and rigorous person from her. Thank you for the support, comments, and motivation for conducting experiments and writing this dissertation.

I am especially thankful to my dissertation committee: Dr. Marek Locmelis, Dr. David Wronkiewicz, and Dr. Xiaofei Fu. They guide me through my PhD study. They are always ready for discussion and their expertise always brings me new view to my research.

I am grateful to all of those with whom I have had the pleasure to work during my study. I want to thank my friends, especially Dr. Le Ma and He Li, and colleagues in the geophysics group of Missouri University of Science and Technology.

Sincere gratitude and very special thanks go to my family. They always give me endless love and encouragement when I have needed them the most. My family is always behind me and provides unending support without asking.

# TABLE OF CONTENTS

Page

PUBLICATION DISSERTATION OPTION ..... iii

ABSTRACT ..... iv

ACKNOWLEDGMENTS ..... v

LIST OF ILLUSTRATIONS ..... xi

LIST OF TABLES ..... xiv

SECTION

1. INTRODUCTION ..... 1

PAPER

I. RECEIVER FUNCTION IMAGING OF MANTLE TRANSITION ZONE DISCONTINUITIES BENEATH THE TANZANIA CRATON AND ADJACENT SEGMENTS OF THE EAST AFRICAN RIFT SYSTEM ..... 4

ABSTRACT ..... 4

1. INTRODUCTION ..... 4

2. DATA AND METHODS ..... 8

3. RESULTS ..... 10

4. DISCUSSION ..... 12

4.1. NORMAL MTZ THICKNESS BENEATH THE TC AND WESTERN BRANCH ..... 14

4.2. ANOMALOUSLY THIN MTZ BENEATH THE EASTERN BRANCH ..... 15

4.2.1. Plume Model. ..... 16

4.2.2. Non-plume Model..... 18

4.3. IMPLICATIONS ON RIFTING MECHANISMS..... 19

5. CONCLUSIONS..... 20

APPENDIX A. SUPPLEMENTARY MATERIAL..... 21

REFERENCES..... 21

II. ABSENCE OF THERMAL INFLUENCE FROM THE AFRICAN SUPERSWELL AND CRATONIC KEELS ON THE MANTLE TRANSITION ZONE BENEATH SOUTHERN AFRICA: EVIDENCE FROM RECEIVER FUNCTION IMAGING.. 29

ABSTRACT..... 29

1. INTRODUCTION..... 30

2. DATA AND METHODS..... 34

2.1. DATA..... 34

2.2. MOVEOUT CORRECTION AND STACKING..... 35

2.3. WAVE SPEED CORRECTION..... 37

3. RESULTS..... 40

3.1. APPARENT DISCONTINUITY DEPTHS AND MTZ THICKNESS..... 40

3.2. SPATIAL VARIATION OF STACKING AMPLITUDES..... 41

3.3. WAVE SPEED CORRECTED DEPTHS..... 42

4. DISCUSSION..... 46

4.1. THERMAL STRUCTURE OF THE MTZ..... 46

4.2. UPPER MANTLE WAVE SPEED AOMALIES DERIVED FROM THE APPARENT DISCONTINUITY DEPTHS..... 47

5. CONCLUSIONS..... 52

ACKNOWLEDEGEMENTS..... 53

APPENDIX A. SUPPLEMENTARY MATERIAL ..... 53

REFERENCES ..... 53

III. MANTLE TRANSITION ZONE STRUCTURE BENEATH NORTHEAST ASIA: EVIDENCE FROM RECEIVER FUNCTIONS ..... 59

ABSTRACT ..... 59

1. INTRODUCTION ..... 60

2. DATA AND METHOD ..... 64

2.1. DATA ..... 64

2.2. DATA PROCESSING ..... 66

3. RESULTS ..... 67

4. DISCUSSION ..... 71

4.1. IMPLICATIONS FOR THE DEPTH AND LATERAL EXTENTS OF THE SUBDUCTED PACIFIC SLAB BENEATH SORTHEAST ASIA.. 71

4.2. FORMATION MECHANISM OF CENOZOIC VOLCANOES IN NORTHEAST CHINA ..... 72

4.3. SMALL-SCALE THERMAL UPWELLING ADJACENT TO THE CURRENT PACIFIC SLAB IN THE MTZ ..... 76

4.4. EVIDENCE FOR THE EXISTENCE OF SUBDUCTED ANCIENT PACIFIC SLAB IN THE MTZ ..... 77

4.5. RIFTING MECHANISM OF BAIKAL RIFT ..... 77

4.6. THERMAL UPWELLING BENEATH THE HAGAY DOME AND ALTAI MOUNTAIN ..... 78

5. CONCLUSION ..... 79

APPENDIX A. SUPPLEMENTARY MATERIAL ..... 81

REFERENCES ..... 82

IV. CRUSTAL STRUCTURE IN THE MALAWI AND LUANGWA RIFT ZONES AND ADJACENT AREAS ..... 89

ABSTRACT ..... 89

1. INTRODUCTION ..... 89

2. TECTONIC SETTING ..... 91

3. DATA AND METHODS ..... 93

3.1. H- κ STACKING ..... 94

3.2. RF MIGRATION ..... 95

3.3. RESIDUAL OIL EFFECT ..... 95

4. RESULTS ..... 96

4.1. CRUSTAL THICKNESS AND VP/VS FROM H-κ STACKING ..... 97

4.2. MOHO DEPTH VARIATION FROM MIGRATED RFS ..... 98

4.3. RESULTS FROM GRAVITY MODELING ..... 100

5. DISCUSSION ..... 102

5.1. CONSTRAINTS ON CRUSTAL MAGMATIC INTRUSION AND PARTIAL PELTING BENEATH THE MRZ ..... 102

5.2. MAGMA-DERIVED $CO_2$ SUFFUSION OF BOUNDARY FAULTS IN THE NORTHERN MRZ ..... 103

5.3. POSSIBLE EXISTENCE OF A MESOPROTEROZOIC SUTURE ZONE BENEATH THE MWEMBESHI SHEAR ZONE AND POST-RIFTING HEALING OF THE LRZ ..... 104

6. CONCLUSIONS ..... 106

ACKNOWLEDGEMENTS ..... 107

REFERENCES ..... 108

SECTION

2. CONCLUSIONS ..... 113

BIBLIOGRAPHY ..... 115

VITA…….. 116

# LIST OF ILLUSTRATIONS

Page

PAPER I

Figure 1 Topographic relief map of the study area showing the center of radius = 1° bins (filled circles), and major tectonic boundaries (solid black lines)..... 7

Figure 2 (a) Results of stacking all available normal moveout-corrected RFs in 1° radius bins with a minimum of six high-quality RFs, plotted with the sequentially increasing depth of the d410. (b) Similar to Figure 2a but for sequentially increasing depth of the d660..... 11

Figure 3 (a) Spatial distribution of resulting d410 apparent depths. (b) Same as Figure 3a but for the d660. (c) MTZ thickness measurements. Red triangles represent Cenozoic volcanoes. (d) Standard deviation (SD) of the MTZ thickness measurements. ..... 13

Figure 4 Schematic models to explain the observed depressions of the MTZ discontinuities beneath the Eastern Branch.. ..... 18

PAPER II

Figure 1 Topographic relief map of the study area showing the center of radius =1° bins (filled circles), and major tectonic boundaries (black dashed lines)..... 33

Figure 2 Spatial distribution of earthquake source areas. ..... 34

Figure 3 Results of stacking moveout-corrected RFs within each bin plotted along 20 latitudinal profiles..... 38

Figure 4 (a) Results of stacking all available normal moveout corrected RFs from 1° radius bins with a minimum of 10 high-quality RFs, plotted against the sequentially increasing depth of the d410. (b) Similar to (a) but against the sequentially increasing depth of the d660.. ..... 39

Figure 5 (a) Spatial distribution of resulting d410 depths. (b) Same as (a) but for the d660. (c) MTZ thickness measurements. (d) Standard deviation (SD) of the MTZ thickness measurements..... 43

Figure 6 Correlation plot of apparent d410 and d660 depths. ..... 44

Figure 7 Stacking amplitude (relative to that of the direct P-wave) for (a) d410 and (b) d660. ..... 45

Figure 8 (a) Number of RFs in bins within a 150 km wide band centered at Profile a–b shown in Figure.1. (b) Resulting depth series in the bins.. ..... 49

Figure 9 Required P-wave velocity anomalies (relative to the IASP91 Earth model) in order to correct the observed apparent d410depths to a uniform true depth of 410km..... 50

Figure 10 Estimated lithospheric thickness as a function of P-wave velocity contrast across the LAB beneath the Kaapvaal Craton (red line), Zimbabwe Craton (blue line) and Limpopo Belt (green line)..... 52

PAPER III

Figure 1 Topographic relief map of northeast Asia showing distribution of Cenozoic volcanoes (red triangles), seismic stations (purple triangles), major tectonic provinces, and depth contours of the subducting Pacific slab..... 65

Figure 2 (a) Depth series in 1° radius bins plotted with respect to the sequentially increasing depth of the d410. (b) Same as Figure 2a but for sequentially increasing depth of the d660..... 68

Figure 3 (a) Spatial distribution of resulting d410 depths. (b) Same as (a) but for the d660. (c) MTZ thickness measurements. (d) Standard deviation (SD) of the MTZ thickness measurements..... 69

Figure 4 Correlation plot of apparent d410 and d660 depths. ..... 70

Figure 5 Averaged upper mantle (first row), MTZ (second row), topmost lower mantle (third row) P-wave velocity anomalies, and corrected MTZ thickness (fourth row) by the previous studies..... 73

Figure 6 Stacked receiver functions across 3 latitudinal lines. ..... 74

PAPER IV

Figure 1 Topographic map of the study area showing the distribution of seismic stations (blue triangles) used in the study and major tectonic features. ..... 92

Figure 2 Surface elevation (top panels) and migrated receiver function profiles (bottom panels) along rift-orthogonal (left panels) and rift parallel (right panels) profiles.. ..... 97

Figure 3 (a). Distribution of resulting crustal thickness. (b). Resulting $V_p/V_s$ measurements. Results of modeling of gravity anomaly data along the rift orthogonal profile (c) and the riftparallel profile (d). Red crosses and solid line represent observed and calculated Bouguer gravity anomalies, respectively. ..... 99

# LIST OF TABLES

Page

PAPER III

Table 1 Averaged measurements for each of the subareas ..... 68

# 1. INTRODUCTION

In this study, we analyzed the structure and evolution of the crust, upper mantle, and the mantle transition zone (MTZ) beneath East Africa and Northeast Asia in four parts by stacking an unprecedented volume of receiver functions. The first part demonstrates the rifting mechanism of Western and Eastern Branches of East African Rift System (EARS). The initiation and development of the EARS, which is an archetype of continental rifts, remain enigmatic. The debate is particularly intensive for the central part of the EARS, where the African lithosphere is divided into the Nubian and Somalian plates and the Victoria and Rovuma microplates by the Eastern and Western Branches which are separated by the Archean Tanzania Craton (Chorowicz, 2005). Several studies of the mantle transition zone (MTZ) discontinuities have been conducted in the EARS, frequently with controversial conclusions regarding the thermal state of the MTZ and rifting mechanisms. In this part, we utilized an unprecedented volume of high-quality receiver functions (RFs) to image the MTZ discontinuities beneath the Tanzania Craton and the surrounding Western and Eastern Branches, for the purpose of providing additional constraints on the role that the African superplume may play on the initiation and development of the EARS.

The thermal influence from the African Superswell and cratonic keels on the MTZ beneath southern Africa is discussed in the second part. In spite of numerous observational and geodynamic modeling studies, mechanisms responsible for the anomalously high topography of southern Africa remain controversial (Lithgow-Bertelloni and Silver, 1998; Hu et al., 2018). One of the most commonly invoked

hypotheses is the dynamic effects of the African Superswell, a low-seismic wave speed anomaly in the lower mantle beneath most of the southern hemispheric region of Africa and the neighboring oceanic areas of the African Plate (Lithgow-Bertelloni and Silver, 1998; Romanowicz and Gung, 2002; Ni et al., 2005). Another controversial issue is the depth extent of the cratonic keels and their influence on the temperature distribution in the upper mantle and MTZ. In this part, we applied a non-plane wave assumption approach (Gao and Liu, 2014a) to an expanded data set recorded over the past 27yr to provide an enhanced image of the MTZ discontinuities beneath southern Africa. The results provide tighter and more reliable constraints on the deep structure and temperature and water content of the upper mantle and MTZ beneath southern Africa.

In the third part, a number of critical issues associated with the subducted Pacific slab and its effects on the developments of the Cenozoic volcanisms in northeast Asia are discussed. Despite numerous studies, the geometry and depth extent of the subducted Pacific plate are still inconclusive due to limited vertical resolution of the tomographic inversion techniques (Foulger et al., 2013). The intraplate Cenozoic volcanos in northeast China are mainly distributed along the edges of the Songliao basin, and the mechanisms of these intraplate volcanisms are still much debate. Furthermore, the origins of the Baikal rift and Hangay dome remain mysterious. In this part, we imaged the topography of the d410 and d660 under the non-plane wave assumption using 274,593 P-to-S RFs beneath northeast Asia. The resulted systematic spatial variations of the MTZ thickness and apparent discontinuity depths can provide valuable constraints on these critical issues.

In the last part, we present measurements from a joint receiver function and gravity study using recently recorded broadband seismic and gravity data that we collected as part of an interdisciplinary investigation (Gao et al., 2013) to unveil the crustal characteristics and impact of $CO_2$ and partial melting on $V_p/V_s$ beneath the Malawi and Luangwa rift zones (MRZ and LRZ, respectively) and adjacent areas.

# PAPER

## I. RECEIVER FUNCTION IMAGING OF MANTLE TRANSITION ZONE DISCONTINUITIES BENEATH THE TANZANIA CRATON AND ADJACENT SEGMENTS OF THE EAST AFRICAN RIFT SYSTEM


## ABSTRACT

The mantle transition zone (MTZ) discontinuities beneath the Tanzania Craton and the Eastern and Western Branches of the East African Rift System are imaged by stacking over 7,100 receiver functions. The mean thickness of the MTZ beneath the Western Branch and Tanzania Craton is about 252 km, which is comparable to the global average and is inconsistent with the existence of present-day thermal upwelling originating from the lower mantle. In contrast, beneath the Eastern Branch, an up to 30 km thinning of the MTZ is observed and is attributable to upwelling of higher temperature materials from either the upper MTZ or the lower mantle. The observations are in agreement with the hypothesis that rifting in Africa is primarily driven by gradients of gravitational potential energy and lateral variations of basal traction force along zones of significant changes of lithospheric thickness such as the edges of the Tanzania Craton.


## 1. INTRODUCTION

The initiation and development of the East African Rift System (EARS), which is an archetype of continental rifts, remain enigmatic in spite of numerous studies (Burke & Wilson, 1972; Ebinger & Sleep, 1998; Foulger et al., 2013; Koptev et al., 2015; Rychert

et al., 2012; Stamps et al., 2014, 2015). One of the frequently involved features in rifting models for the EARS is the African superplume, a low-velocity feature in the lower mantle (Nyblade & Robinson, 1994; Ritsema et al., 1999). Previous seismic tomographic studies have reached contrasting conclusions about whether superplume materials have reached the upper mantle, and if they have played a significant role in the development of the EARS (Chang et al., 2015; Corchete, 2012; Debayle et al., 2001; Fishwick, 2010; Mulibo & Nyblade, 2013a; O'Donnell et al., 2013; 2016; Priestley et al., 2008; Ritsema et al., 1998).

The debate is particularly intensive for the central part of the EARS, where the African lithosphere is divided into the Nubian and Somalian plates and the Victoria and Rovuma microplates by the Eastern and Western Branches which are separated by the Archean Tanzania Craton (TC) (Figures 1 and S1 in the supporting information) (Chorowicz, 2005). This controversy is most likely caused by the limited vertical resolution of the tomographic techniques and the pervasive use of relative (rather than absolute) travel time residuals (Foulger et al., 2013), as well as the wave front healing effects of deep and thin (relative to the wavelength) mantle plumes (Montelli et al., 2004).

Petrophysical, geodynamic modeling, and observational studies conducted over the past several decades have demonstrated that the topography of the mantle transition zone (MTZ) discontinuities found ubiquitously at the globally averaged depths of approximately 410 km (d410) and 660 km (d660) are functions of MTZ water content and in situ temperature in the vicinity of the discontinuities (Flanagan & Shearer, 1998; Hirose, 2002; Ringwood, 1991; Shearer & Masters, 1992). Specifically, a depression of the d410 indicates a higher than normal temperature due to the positive Clapeyron slope

of the olivine-wadsleyite transition, while an uplifted d660 is anticipated for areas with thermal upwelling from the lower mantle, as a result of the negative Clapeyron slope of the ringwoodite to bridgmanite and ferropericlase phase transition (Helffrich, 2000; Ringwood, 1975; Tschauner et al., 2014). If the temperature at the bottom of the MTZ increases from the estimated normal value of approximately 1600℃ to higher than 1800℃, the dominant phase transition associated with the d660 becomes the transition from majorite to perovskite, which has a positive Clapeyron slope of +1.0 MPa/K (Hirose, 2002). Anomalously high-water content in the MTZ has similar effects as low temperature, that is, leading to an uplifted d410 and depressed d660 and consequently a thicker than normal MTZ (Litasov et al., 2005; Ohtani et al., 2004).

Several studies of MTZ discontinuities have been conducted in the EARS, frequently with controversial conclusions regarding the thermal state of the MTZ and rifting mechanisms. Owens et al. (2000) and Huerta et al. (2009) imaged the structure of the MTZ beneath the EARS based on the 3-D model of Ritsema et al. (1998) and the 1-D IASP91 model, respectively. Both studies revealed a locally depressed d410 beneath the Eastern Branch and a widely depressed d660 beneath the TC and adjacent areas and suggested the existence of a mantle plume traversing both the d660 and d410 and reaching shallow mantle depths. Mulibo and Nyblade (2013b) corrected the depths of the d410 and d660 by using a 3-D velocity model (Mulibo & Nyblade, 2013a). Their results implied that the superplume induced a thinning of the MTZ beneath a broad area of Eastern Africa, including the Eastern Branch and the central and southern regions of the TC, and advocated for pervasive thermal upwelling of superplume-originated material through the MTZ and its active role in rift development.

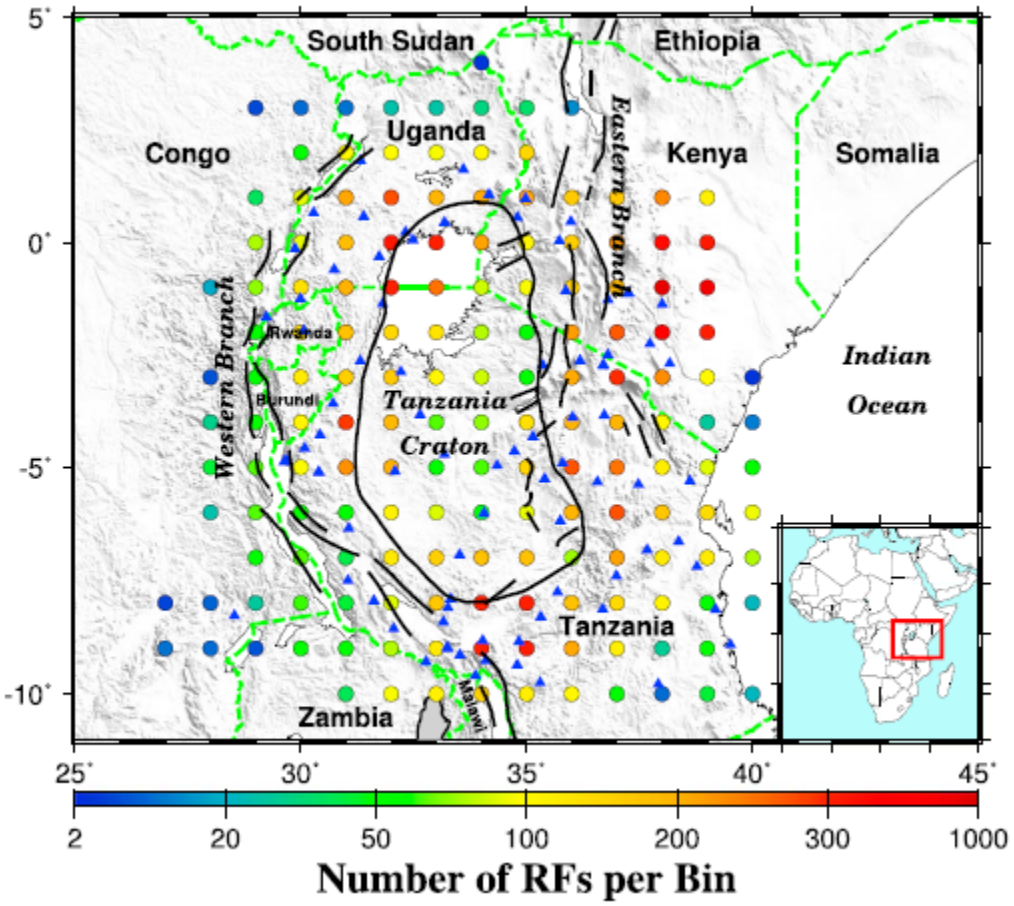


Figure 1 Topographic relief map of the study area showing the center of radius = 1° bins (filled circles), and major tectonic boundaries (solid black lines). The color of the circles represents the number of RFs per bin. The blue triangles are seismic stations used in the study, and the green lines are national boundaries. The red rectangle in the inset map shows the study area.

Results from some other MTZ studies, however, are inconsistent with the existence of mantle plumes rising from the lower mantle traversing the MTZ. Julia and Nyblade (2013) utilized 2,557 P wave receiver functions from 30 permanent broadband stations in Africa to image the MTZ discontinuities and found no significant thinning of the MTZ beneath the EARS. Tauzin et al. (2008) conducted a global study and found no

clear evidence for the thinning of the MTZ beneath the EARS. Beneath the Afar Depression and Ethiopian Plateau, Reed, Gao, et al. (2016) reported that velocity perturbations in the upper mantle are the major factors for an apparent 40-60 km depression of both MTZ discontinuities. Similarly, beneath the nonvolcanic Okavango Rift in Botswana (Yu, Liu, et al., 2015) and the Malawi Rift which is the southward extension of the Western Branch, no significant thinning of the MTZ is observed (Reed, Liu, et al., 2016).

In this study, we utilized an unprecedented volume of high-quality receiver functions (RFs) to image the MTZ discontinuities beneath the TC and the surrounding Western and Eastern Branches, for the purpose of providing additional constraints on the role that the African superplume may play on the initiation and development of the EARS.

## 2. DATA AND METHODS

All the broadband seismic data used in the study were obtained from the Incorporated Research Institutions for Seismology (IRIS) Data Management Center (DMC). We requested all the available teleseismic data (epicentral distance range 30–100°) recorded by broadband stations located in the area of -10°N to 5°N and 25°E to 45°E during the recording period from May 1994 to March 2017. The cutoff magnitude (Mc) is determined using the epicentral distance (Δ) and focal depth (D) according to the equationMc = 5.2+(Δ-30.0)/(180.0-30.0)-D/700.0 (Liu & Gao, 2010). A four-pole, two-pass band-pass Bessel filter with a frequency range of 0.02-0.2 Hz was applied to the

original three-component seismograms. The seismograms with a first-arrival signal-to-noise ratio (SNR) on the vertical component below 4.0 were not used in the study. The SNR is obtained by max |As|/|Ān|, where max |As| is the maximum absolute amplitude on the vertical seismogram 8 s before and 17 s after the predicted IASP91 arrival time for the first P wave, and |Ān| is the mean absolute amplitude in the time window of 10–20 s before the predicted P wave arrival time (Gao & Liu, 2014a, 2014b). The remaining seismograms were converted into radial RFs using the frequency-domain water-level deconvolution procedure with a Gaussian factor of 5.0 (which corresponds to a high-pass corner frequency that is greater than that of the Bessel filter, so that the filtering is solely performed by the latter) and a water level of 0.03 (Ammon, 1991; Clayton & Wiggins, 1976). Before calculating the RFs, we adopted a set of exponential weighting functions to reduce the strong PP arrivals which are found to degenerate the RFs (Gao & Liu, 2014a). A total of 7,139 high-quality RFs from 1,871 events recorded by 87 stations were utilized for this study (Figures 1 and S2).

A non-plane wave assumption approach (Gao & Liu, 2014a) was employed to migrate and stack the P-to-S converted phases generated from the MTZ discontinuities. By considering the difference in ray parameters between the direct P wave and the converted S wave, this approach can more accurately estimate the discontinuity depths and lead to sharper discontinuity images than approaches assuming a plane wave front. Using the 1-D IASP91 Earth model (Kennett & Engdahl, 1991), the geographic coordinates of the ray-piercing point for each of the RFs were computed at the middle of the MTZ (535 km depth). The moveout-corrected RFs within 1° radius circular bins, which are one geographic degree apart from the neighboring bins (Figure 1), were then

stacked to form a depth series for each of the bins. Results from bins with less than six RFs are not used. A bootstrap resampling procedure with 50 resampling iterations (Efron & Tibshirani, 1986; Liu et al., 2003) was used to compute the mean and standard deviation of the MTZ discontinuity depths and MTZ thickness for each bin. Detailed description of the migration and stacking procedures and specific data processing parameters can be found in Gao and Liu (2014a, 2014b).

## 3. RESULTS

For each of the stacked traces, the optimal depth of an MTZ discontinuity is determined using the following steps. First, the depth corresponding to the maximum stacking amplitude in a fixed depth range (380-440 km for the d410 and 650-710 km for the d660) is automatically determined and marked on the trace. Second, the automatically determined depth is visually verified to reject the ones with ambiguous and weak arrivals that are significantly different from neighboring bins. Third, for a small fraction of the traces, the search range is adjusted so that the picked depth is consistent with neighboring bins. A total of 162 bins with clearly observable d410 or d660 peaks were obtained (Figure 2), among which 147, 139, and 124 have reliable peaks for the d410, d660, and both, respectively. Profiles of the resulting depth series along all the 14 latitudinal lines (from 10°S to 3°N with a 1° increment), together with the mean depths and the error bar, are shown in Figure S3, and all the observed depths of the discontinuity arrivals and the MTZ thicknesses are listed in Table S1.

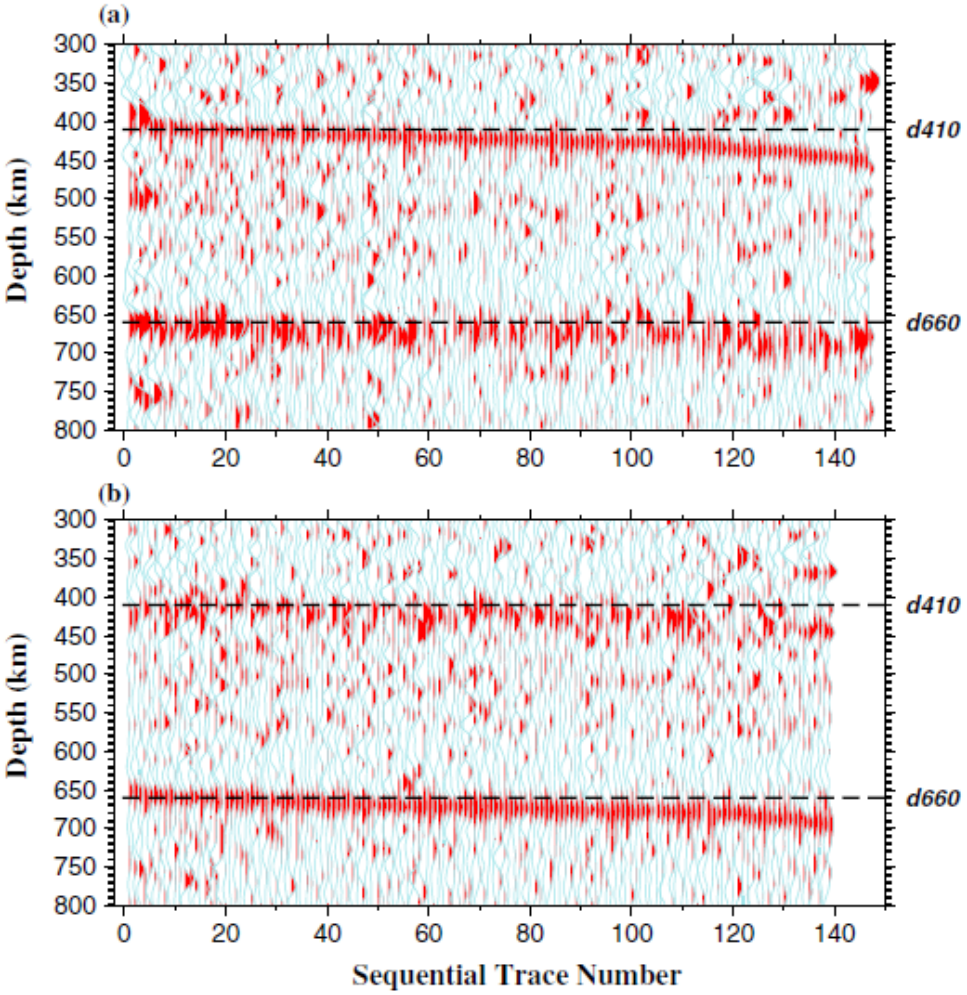


Figure 2 (a) Results of stacking all available normal moveout-corrected RFs in 1° radius bins with a minimum of six high-quality RFs, plotted with the sequentially increasing depth of the d410. (b) Similar to Figure 2a but for sequentially increasing depth of the d660.

The observations (Figure S1) were fitted with a continuous curvature surface gridding algorithm (Smith & Wessel, 1990) (Figure 3) with a tension factor of 0.5, in order to generate spatially continuous images for the observed depths and MTZ thicknesses. The standard deviation of the resultant MTZ thickness is less than 6 km for

the majority of the study area (Figure 3d). The mean apparent depths of the d410 and d660 over the region are 423±12 km and 672±9 km, respectively, and the vast majority of the depths exceed the global averages in the IASP91 Earth model of 410 and 660 km, respectively. The apparent depths of both the d410 and d660 increase systematically toward the northeast part of the study area (Figure 3). The resulting apparent depths of the d410 range from about 390 km beneath the southeastern part of Tanzania to a maximum value of 460 km at the northeastern corner of the study area (Figure 3a). A trend similar to the d410 is observed for the apparent depths of the d660 (Figure 3b).

## 4. DISCUSSION

The depths of the MTZ discontinuities are calculated under the 1-D IASP91 Earth model, and thus, the depths are apparent rather than true depths. The true depths can only be achieved when absolute (rather than relative to the mean values of a study area) velocity anomalies of both the P and S waves are available for the entire crust, upper mantle, and MTZ (e.g., Gao & Liu, 2014b, for the contiguous United States). Due to the discrepancies in previous seismic tomographic studies, as well as the fact that the vast majority of the studies only reported relative P or S wave (but not both) velocity anomalies for the shallow upper mantle (e.g., Adams et al., 2012; Fishwick, 2010; Pasyanos & Nyblade, 2007; Priestley et al., 2008; Slack & Davis, 1994), such corrections using results from any of the existing tomographic studies would not lead to trustful results.

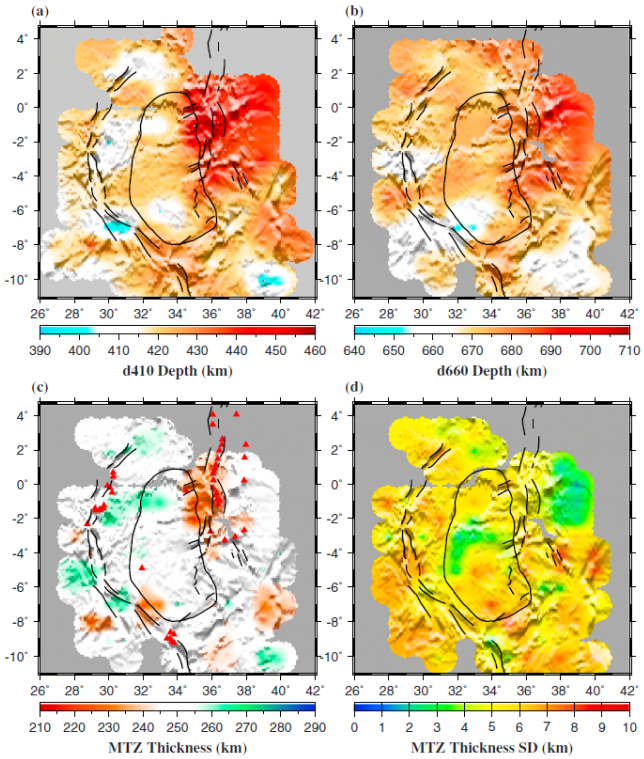


Figure 3 (a) Spatial distribution of resulting d410 apparent depths. (b) Same as Figure 3a but for the d660. (c)MTZ thickness measurements. Red triangles represent Cenozoic volcanoes. (d) Standard deviation (SD) of the MTZ thickness measurements.

Therefore, in the following we utilize the observed apparent discontinuity depths to infer velocity, thermal, and water content anomalies.

As discussed in various previous studies, three factors have been recognized to affect the apparent depths of the MTZ discontinuities (see Mohamed et al., 2014, for a more detailed discussion). The first factor is velocity anomalies in the upper mantle, that is, above the d410 associated with temperature, partial melting, and compositional heterogeneities. The presence of low and high-velocity anomalies in the upper mantle causes simultaneous apparent depressions and uplifts of both the d410 and d660,

respectively, leading to positively correlated apparent d410 and d660 depths, as exemplified by the spatial similarities between the d410 and d660 depths shown in Figures 3a and 3b (correlation coefficient = 0.54). Velocity anomalies in the MTZ can lead to apparent undulations of the d660 but not the d410 and thus reduce the correlation coefficient. The second factor is the temperature anomalies near the d410 and d660, which are related to velocity anomalies by a scaling factor of $dV_p/dT = -4.8\times10^{-4}$ km $s^{-1}$ $℃^{-1}$ (Deal et al., 1999). For example, assuming a Clapeyron slope of +2.9 MPa/K (Bina & Helffrich, 1994) for the d410 and −1.3 MPa/K (Fei et al., 2004) for the d660, a 300℃ temperature increase around the d410 and d660 corresponds to a 25 km depression of the d410 and a 11 km uplift of the d660 for an assumed $V_s$ and $V_p$ relative anomaly ratio ($dln(V_s)/dln(V_p)$) of 1.8 (Gao & Liu, 2014b; Mohamed et al., 2014). Note that because the observed depth undulations are relative to the globally averaged values, for a given depth, the temperature anomalies derived from such undulations are relative to the globally averaged temperature at the same depth. The third factor is the presence of the hydrous materials in the MTZ, which depresses the d660 and uplifts the d410 (Ohtani et al., 2004).

### 4.1. NORMAL MTZ THICKNESS BENEATH THE TC AND WESTERN BRANCH

Beneath the TC, an ~10 km depression for both the d410 (420±7 km) and d660 (672±7 km) and a close-to-normal MTZ thickness are observed (Figure 3). The simplest explanation for the observations is a low-velocity upper mantle with a mean $V_p$ anomaly of -0.86%, which is calculated based on Gao and Liu (2014a) using a $dln(V_s)/dln(V_p)$

value of 1.8, a value that is between that suggested for the stable central United States and the tectonically active western United States (Gao & Liu, 2014b; Schmandt & Humphreys, 2010). Additionally, both the weak deepening of the d410 and the normal thickness of the MTZ suggest negligible effect of temperature on the MTZ (Deuss, 2007; Tauzin et al., 2008). Reed, Gao, et al. (2016) quantitatively discussed the possibility of the existence of a mantle plume rising from the lower mantle beneath an area with a normal MTZ thickness and suggested that a mantle plume only exists under a specific combination of temperature, hydrous materials, and velocity anomalies. However, this specific combination would be difficult to exist everywhere beneath the entire TC. Therefore, we propose a non-plume model with lateral velocity variation in the upper mantle beneath the TC to explain the apparently depressed MTZ discontinuities with a normal MTZ thickness.

The mean MTZ thickness (252±12 km) and the apparent discontinuity depths beneath the Western Branch are comparable to those of the TC. Those observations are consistent with the previously observed similarity in lithospheric thickness between the two areas (Chesley et al., 1999; Vauchez et al., 2005) and imply the absence of both significant thinning of the mantle lithosphere (Davies, 1994; Rychert et al., 2012) and thermal upwelling of lower mantle materials beneath the Western Branch, favoring a passive rifting mechanism for this section of the EARS.

### 4.2. ANOMALOUSLY THIN MTZ BENEATH THE EASTERN BRANCH

The most prominent feature in the study area is an up to 30 km apparent thinning of the MTZ beneath the Eastern Branch. This thinning is associated with a 50 km

apparent depression of the d410 and a 20 km depression of the d660 (Figure 3). Since the depressed d410 and the thinned MTZ can be interpreted as a result of thermally perturbed structure in the upper mantle as well as in the MTZ, two models with and without a thermal upwelling from the lower mantle ("plume and non-plume models") are discussed in the following in order to quantitatively interpret the observed results.

**4.2.1. Plume Model.** The existence of an active mantle plume beneath the Eastern Branch (Figure S4a) has been proposed based on seismic tomography (Mulibo & Nyblade, 2013a), MTZ topography studies (Huerta et al., 2009; Mulibo & Nyblade, 2013b), geodynamic modeling (Koptev et al., 2015), and geochemical studies (Roberts et al., 2012). In order to produce the observed ~50 km depression of the d410, a −1.8% mean $V_p$ and associated high-temperature anomalies in the upper mantle are required. The total depression of 50 km would include a 22 km apparent depression due to the low-velocity upper mantle, and an additional 28 km true depression from the 340℃ temperature increase corresponding to the low-velocity anomaly (estimated using a Clapeyron slope of +2.9 MPa/K; Figure 4a). Similarly, the downward extension of the low-velocity zone into the lower mantle would produce a 35 km apparent depression of the d660, and a 12 km true uplift of d660 (calculated using a Clapeyron slope of -1.3 MPa/K (Fei et al., 2004)), leading to a 23 km net depression of the d660. Therefore, the plume model would produce a net 27 km thinning of the MTZ, which is similar to the observed MTZ thickness beneath the Eastern Branch (Figures 3c and 4a).

One potential problem with the plume model is that the low MTZ velocities associated with the plume may correspond to an anomalously high-temperature environment in the vicinity of the d660, in which the dominant phase transition is

majorite (rather than ringwoodite) to perovskite. Specifically, the normal temperature at the bottom of the MTZ is estimated to be about 1600℃ (Ito & Katsura, 1989), while the plume model (Figure 4a) requires a 340℃ thermal anomaly at the base of the MTZ, leading to a temperature as high as 1940℃. This required temperature is higher than the 1800℃ temperature above which the dominant phase transition becomes majorite to perovskite, which has a positive Clapeyron slope of +1.0 MPa/K (Irifune et al., 1996, Hirose, 2002, Hirose et al., 2001). Applying a +1.0 MPa/K Clapeyron slope for the transition, the d660 would depress about 9 km corresponding to the temperature increase. Together with the 35 km apparent depression of the d660 due to the low-velocity upper mantle and MTZ, the d660 would depress about 44 km in total. Because the d410 has a 50 km depression due to both the velocity and thermal effects, the amount of MTZ thinning under the plume model is about 6 km, which is significantly smaller than the observed ~30 km. It should be noted that those estimates are based on a number of experimentally determined quantities with large uncertainties and variably limiting temperature-pressure conditions, including the velocity and temperature anomaly scaling factor, the $d\ln(V_s)/d\ln(V_p)$ value, and the Clapeyron slopes (see Tauzin & Ricard, 2014, for some of the reported values). The existence of partial melts in the upper mantle and the MTZ can also affect the estimated depths. The required temperature anomaly to produce the apparent depression of the discontinuities would reduce if partial melt exists in the upper mantle and MTZ. If a certain amount of melt is present, the temperature in the vicinity of the d660 could be lower than 1800℃, so that the phase transition across the d660 would be from ringwoodite (rather than majorite) to perovskite. Therefore, the

existence of a thermal upwelling from the lower mantle cannot be confidently ruled out solely based on those arguments.

**4.2.2. Non-plume Model.** In this model (Figure S4b), a low-velocity zone with a $V_p$ anomaly of -1.8%reaches the d410 and only extends to the uppermost MTZ (Figure 4b). The low velocities result in an apparent depression of 22 km for both the d410 and d660. In addition, the high temperature associated with the low velocities leads to an additional 28 km depression of the d410, resulting in a 28 km thinning of the MTZ which is comparable to the observed value beneath the Eastern Branch.

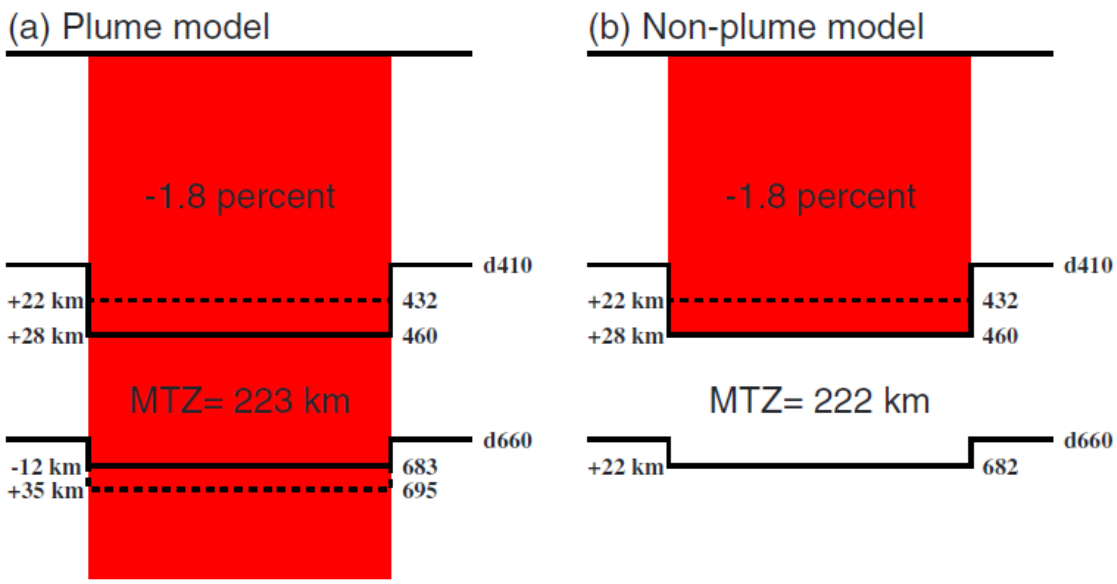


Figure 4 Schematic models to explain the observed depressions of the MTZ discontinuities beneath the Eastern Branch. (a) The plume model, in which a thermal plume with a velocity anomaly of -1.8% and a corresponding thermal anomaly of 340℃ rises from the lower mantle. (b) The non-plume model, in which a velocity anomaly exists in the upper mantle as well as the uppermost MTZ. The dashed lines represent the apparent depths of the discontinuities due to the presence of the low velocities, and the solid lines are the final depths. The models produce a 27-28 km thinning of the MTZ.

Relative to the plume model, the non-plume model is simpler and can more easily explain the spatial correspondence between the surface expression of the rift and the thinned MTZ. However, the cause of the high-temperature anomaly associated with the observed depression of the d410 remains problematic. Upwelling of higher temperature material from the upper MTZ to the upper mantle can certainly increase mantle temperature in the vicinity of the d410, but it is difficult for this process to produce such a high-temperature anomaly. Additionally, this process requires that the MTZ be a thermal boundary layer from which a thermal plume originates, a hypothesis that is inconsistent with geodynamic modeling results (e.g., Schubert et al., 1995).

### 4.3. IMPLICATIONS ON RIFTING MECHANISMS

The above discussions suggest that ambiguities still remain regarding the existence or absence of thermal upwelling from the lower mantle beneath the northern part of the Eastern Branch, and thus, additional studies are needed in order to resolve this critical issue. However, as detailed below, such uncertainty plays an insignificant role when rifting mechanisms are discussed in light of the new MTZ discontinuity measurements presented in this study.

The possible existence of a thermal upwelling from the lower mantle (under the plume model) beneath the northern part of the Eastern Branch seems to be consistent with the active rifting model. However, a lack of such upwelling in the rest of the Eastern Branch and the entire Western Branch makes such a rifting mechanism unlikely for the Eastern and Western Branches. The absence of significant thermal upwelling from the lower mantle beneath other segments of the EARS has also been inferred for the Afar

Depression (Reed, Gao, et al., 2016), the Malawi Rift of the EARS (Reed, Liu, et al., 2016), and the Okavango Rift (Yu, Liu, et al., 2015) and is suggested by geodynamic modeling (Quere & Forte, 2006; Stamps et al., 2014; 2015).

The observations presented in the study are consistent with the hypothesis that rifting in East Africa is driven by gradients of gravitational potential energy probably originating from the African superplume (Lithgow-Bertelloni & Silver, 1998; Moucha & Forte, 2011; Stamps et al., 2014, 2015), and by lateral variations of horizontal basal traction forces applied to the lithosphere in areas with sudden changes of thickness. The latter has recently been exemplified in the EARS by a number of shear wave splitting investigations (Gao & Liu, 2016; Reed et al., 2017; Yu, Gao, et al., 2015). The significant difference in lithospheric thickness (e.g., Ritsema et al., 1998) between the TC and the surrounding rift segments makes the edges of the TC ideal locations for rift development.

## 5. CONCLUSIONS

We have imaged mantle transition zone discontinuities beneath the TC and the surrounding Eastern and Western Branches of the EARS. A parallel 10 km depression of the apparent depths of MTZ discontinuities and normal MTZ thickness reveal a -0.86% mean upper mantle $V_p$ anomaly, and a lack of significant thermal anomaly in the MTZ beneath most of the Tanzania Craton and the Western Branch. In contrast, a 30 km thinning of the MTZ is found beneath the Eastern Branch associated with a 50 km apparent depression of the d410 and a 20 km depression of the d660. Quantitative analyses of the effects of velocity and thermal anomalies on the observed discontinuity

depths suggest that the most plausible and simplest explanation of the observed apparent depressions and the MTZ thinning is a low-velocity zone with a $V_p$ anomaly of -1.8% extending from the surface to the uppermost MTZ. Those observations may suggest the present-day existence of thermal upwelling from either the lower mantle or the uppermost MTZ beneath the northern part of the Eastern Branch and is comparable with the hypothesis that gradients of gravitational potential energy from the African superplume and lateral variations of basal traction force applied to areas with significant changes of lithospheric thickness are probably responsible for rift development in East Africa.

## APPENDIX A. SUPPLEMENTARY MATERIAL

Supplementary material related to this article can be found online at https://doi.org/10.1002/2017GL075485.

## REFERENCES

Adams, A., Nyblade, A. A., & Weeraratne, D. (2012). Upper mantle shear wave velocity structure beneath the East African plateau: Evidence for a deep, plateauwide low velocity anomaly. Geophysical Journal International, 189(1), 123–142. https://doi.org/10.1111/j.1365-246X.2012.05373.x

Ammon, C. J. (1991). The isolation of receiver effects from teleseismic P-waveforms. Bulletin of the Seismological Society of America, 81(6), 2504–2510. Bina, C. R., & Helffrich, G. (1994). Phase transition Clapeyron slopes and transition zone seismic discontinuity topography. Journal of Geophysical Research, 99(B8), 15,853–15,860. https://doi.org/10.1029/94JB00462

Burke, K., & Wilson, J. T. (1972). Is the African plate stationary? Nature, 239(5372), 387–390. https://doi.org/10.1038/239387b0

Chang, S. J., Ferreira, A. M., Ritsema, J., van Heijst, H. J., & Woodhouse, J. H. (2015). Joint inversion for global isotropic and radially anisotropic mantle structure including crustal thickness perturbations. Journal of Geophysical Research: Solid Earth, 120, 4278–4300. https://doi.org/10.1002/2014JB011824

Chesley, J. T., Rudnick, R. L., & Lee, C.-T. (1999). Re-Os systematics of mantle xenoliths from the East African Rift: Age, structure, and history of the Tanzanian craton. Geochimica et Cosmochimica Acta, 63(7), 1203–1217. https://doi.org/10.1016/S0016-7037(99)00004-6

Chorowicz, J. (2005). The east African rift system. Journal of African Earth Sciences, 43(1), 379–410. https://doi.org/10.1016/ j.jafrearsci.2005.07.019

Clayton, R. W., & Wiggins, R. A. (1976). Source shape estimation and deconvolution of teleseismic bodywaves. Geophysical Journal International, 47(1), 151–177. https://doi.org/10.1111/j.1365-246X.1976.tb01267X

Corchete, V. (2012). Shear-wave velocity structure of South America from Rayleigh-wave analysis. Terra Nova, 24(2), 87–104. https://doi.org/10.1111/j.1365-3121.2011.01042X

Davies, G. F. (1994). Thermomechanical erosion of the lithosphere by mantle plumes. Journal of Geophysical Research, 99(B8), 15709–15722. https://doi.org/10.1029/94JB00119

Deal, M. M., Nolet, G., & van der Hilst, R. D. (1999). Slab temperature and thickness from seismic tomography: 1. Method and application to Tonga. Journal of Geophysical Research, 104(B12), 28,789–28,802. https://doi.org/10.1029/1999JB900255

Debayle, E., Leveque, J.-J., & Cara, M. (2001). Seismic evidence for a deeply rooted low-velocity anomaly in the upper mantle beneath the northeastern Afro/Arabian continent. Earth and Planetary Science Letters, 193, 423–436. https://doi.org/10.1016/S0012-821X(01)00509-X

Deuss, A. (2007). Seismic observations of transition zone discontinuities beneath hotspot locations. In G. R. Foulger & D. M. Jurdy (Eds.), Plates, Plumes, and Planetary Processes (Vol. 430, pp. 121–136). Boulder, CO: Geological Society of America. https://doi.org/10.1130/2007.2430(07)

Ebinger, C. J., & Sleep, N. H. (1998). Cenozoic magmatism throughout east Africa resulting from impact of a single plume. Nature, 395(6704), 788–791. https://doi.org/10.1038/27417

Efron, B., & Tibshirani, R. (1986). Bootstrap methods for standard errors, confidence intervals, and other measures of statistical accuracy. Statistical Science, 1(1), 54–75. https://doi.org/10.1214/ss/1177013815

Fei, Y., Van Orman, J., Li, J., van Westrenen, W., Sanloup, C., Minarik, W.,…Funakoshi, K. (2004). Experimentally determined postspinel transformation boundary in Mg2SiO4 usingMgO as an internal pressure standard and its geophysical implications. Journal of Geophysical Research, 109, B02305. https://doi.org/10.1029/2003JB002562

Fishwick, S. (2010). Surface wave tomography: Imaging of the lithosphere-asthenosphere boundary beneath central and southern Africa? Lithos, 120(1), 63–73. https://doi.org/10.1016/j.lithos.2010.05.011

Flanagan, M. P., & Shearer, P. M. (1998). Global mapping of topography on transition zone velocity discontinuities by stacking SS precursors. Journal of Geophysical Research, 103(B2), 2673–2692. https://doi.org/10.1029/97JB03212

Foulger, G. R., Panza, G. F., Artemieva, I. M., Bastow, I. D., Cammarano, F., Evans, J. R.,…Yanovskaya, T. B. (2013). Caveats on tomographic images. Terra Nova, 25(4), 259–281. https://doi.org/10.1111/ter.12041

Gao, S. S., & Liu, K. H. (2014a). Imaging mantle discontinuities using multiply-reflected P-to-S conversions. Earth and Planetary Science Letters, 402, 99–106. https://doi.org/10.1016/j.epsl.2013.08.025

Gao, S. S., & Liu, K. H. (2014b). Mantle transition zone discontinuities beneath the contiguous United States. Journal of Geophysical Research: Solid Earth, 119, 6452–6468. https://doi.org/10.1002/2014JB011253

Gao, S. S., & Liu, K. H. (2016). Rifting initiation through lateral variations of lithospheric basal stress beneath preexisting zones of weakness (Paper No. 229-1). Denver, CO: Geological Society of America Annual Meeting.

Helffrich, G. (2000). Topography of the transition zone seismic discontinuities. Reviews of Geophysics, 38(1), 141–158. https://doi.org/10.1029/1999RG000060

Hirose, K. (2002). Phase transitions in pyrolitic mantle around 670-km depth: Implications for upwelling of plumes from the lower mantle. Journal of Geophysical Research, 107(B4), 2078. https://doi.org/10.1029/2001JB000597

Hirose, K., Fei, Y., Ono, S., Yagi, T., & Funakoshi, K. (2001). In situ measurements of the phase transition boundary in Mg3Al2Si3O12: Implications for the nature of the seismic discontinuities in the Earth’s mantle. Earth and Planetary Science Letters, 184(3), 567–573. https://doi.org/10.1016/S0012-821X(00)00354-X

Huerta, A. D., Nyblade, A. A., & Reusch, A. M. (2009). Mantle transition zone structure beneath Kenya and Tanzania: More evidence for a deep-seated thermal upwelling in the mantle. Geophysical Journal International, 177(3), 1249–1255. https://doi.org/10.1111/j.1365-246X.2009.04092.x

Irifune, T., Koizumi, T., & Ando, J. (1996). An experimental study of the garnet-perovskite transformation in the system $MgSiO_3$-$Mg_3Al_2Si_3O_{12}$. Physics of the Earth and Planetary Interiors, 96(2–3), 147–157. https://doi.org/10.1016/0031-9201(96)03147-0

Ito, E., & Katsura, T. (1989). A temperature profile of the mantle transition zone. Geophysical Research Letters, 16(5), 425–428. https://doi.org/10.1029/GL016i005p00425

Julia, J., & Nyblade, A. A. (2013). Probing the uppermantle transition zone under Africa with P520s conversions: Implications for temperature and composition. Earth and Planetary Science Letters, 368, 151–162. https://doi.org/10.1016/j.epsl.2013.02.021

Kennett, B. L., & Engdahl, E. R. (1991). Traveltimes for global earthquake location and phase identification. Geophysical Journal International, 105(2), 429–465. https://doi.org/10.1111/j.1365-246X.1991.tb06724.X

Koptev, A., Calais, E., Burov, E., Leroy, S., & Gerya, T. (2015). Dual continental rift systems generated by plume-lithosphere interaction. Nature Geoscience, 8(5), 388–392. https://doi.org/10.1038/ngeo2401

Litasov, K. D., Ohtani, E., Sano, A., Suzuki, A., & Funakoshi, K. (2005). Wet subduction versus cold subduction. Geophysical Research Letters, 32, L13312. https://doi.org/10.1029/2005GL022921

Lithgow-Bertelloni, C., & Silver, P. G. (1998). Dynamic topography, plate driving forces and the African superswell. Nature, 395(6699), 269–272. https://doi.org/10.1038/26212

Liu, K. H., & Gao, S. S. (2010). Spatial variations of crustal characteristics beneath the Hoggar swell, Algeria, revealed by systematic analyses of receiver functions from a single seismic station. Geochemistry, Geophysics, Geosystems, 11, Q08011. https://doi.org/10.1029/2010GC003091

Liu, K. H., Gao, S. S., Silver, P. G., & Zhang, Y. K. (2003). Mantle layering across central South America. Journal of Geophysical Research, 108(B11), 2510. https://doi.org/10.1029/2002JB002208

Mohamed, A. A., Gao, S. S., Elsheikh, A. A., Liu, K. H., Yu, Y., & Fat-Helbary, R. E. (2014). Seismic imaging of mantle transition zone discontinuities beneath the northern Red Sea and adjacent areas. Geophysical Journal International, 199(2), 648–657. https://doi.org/10.1093/gji/ggu284

Montelli, R., Nolet, G., Dahlen, F. A., Masters, G., Engdahl, E. R., & Hung, S. (2004). Finite-frequency tomography reveals a variety of plumes in the mantle. Science, 303(5656), 338–343. https://doi.org/10.1126/science. 1092485

Moucha, R., & Forte, A. M. (2011). Changes in African topography driven by mantle convection. Nature Geoscience, 4(10), 707–712. https://doi.org/10.1038/ngeo1235

Mulibo, G. D., & Nyblade, A. A. (2013a). The P and S wave velocity structure of the mantle beneath eastern Africa and the African superplume anomaly. Geochemistry, Geophysics, Geosystems, 14, 2696–2715. https://doi.org/10.1002/ggge.20150

Mulibo, G. D., & Nyblade, A. A. (2013b). Mantle transition zone thinning beneath eastern Africa: Evidence for a whole-mantle superplume structure. Geophysical Research Letters, 40, 3562–3566. https://doi.org/10.1002/grl.50694

Nyblade, A. A., & Robinson, S. W. (1994). The African superswell. Geophysical Research Letters, 21(9), 765–768. https://doi.org/10.1029/94GL00631

O'Donnell, J. P., Adams, A., Nyblade, A. A., Mulibo, G. D., & Tugume, F. (2013). The uppermost mantle shear wave velocity structure of eastern Africa from Rayleigh wave tomography: Constraints on rift evolution. Geophysical Journal International, 194(2), 961–978. https://doi.org/10.1093/gji/ggt13w5

O'Donnell, J. P., Selway, K., Nyblade, A. A., Brazier, R., Tahir, N. E., & Durrheim, R. (2016). Thick lithosphere, deep crustal earthquakes and no melt: A triple challenge to understanding extension in the western branch of the East African Rift. Geophysical Journal International, 204(2), 985–998. https://doi.org/10.1093/gji/ggv492

Ohtani, E., Litasov, K., Hosoya, T., Kubo, T., & Kondo, T. (2004). Water transport into the deep mantle and formation of a hydrous transition zone. Physics of the Earth and Planetary Interiors, 143(1-2), 255–269. https://doi.org/10.1016/j.pepi.2003.09.015

Owens, T. J., Nyblade, A. A., Gurrola, H., & Langston, C. A. (2000). Mantle transition zone structure beneath Tanzania, East Africa. Geophysical Research Letters, 27(6), 827–830. https://doi.org/10.1029/1999GL005429

Pasyanos, M. E., & Nyblade, A. A. (2007). A top to bottom lithospheric study of Africa and Arabia. Tectonophysics, 444(1), 27–44. https://doi.org/10.1016/j.tecto.2007.07.008

Priestley, K., McKenzie, D., Debayle, E., & Pilidou, S. (2008). The African upper mantle and its relationship to tectonics and surface geology. Geophysical Journal International, 175(3), 1108–1126. https://doi.org/10.1111/j.1365-246X.2008.03951.x

Quere, S., & Forte, A. M. (2006). Influence of past and present-day plate motions on spherical models of mantle convection: Implications for mantle plumes and hotspots. Geophysical Journal International, 165(3), 1041–1057. https://doi.org/10.1111/j.1365-246X.2006.02990.x

Reed, C. A., Gao, S. S., Liu, K. H., & Yu, Y. (2016). The mantle transition zone beneath the Afar Depression and adjacent regions: Implications for mantle plumes and hydration. Geophysical Journal International, 205(3), 1756–1766. https://doi.org/10.1093/gji/ggw116

Reed, C. A., Liu, K. H., Chindandali, P., Massingue, B., Mdala, H., Mutamina, D.,…Gao, S. S. (2016). Passive rifting of thick lithosphere in the southern East African Rift: Evidence from mantle transition zone discontinuity topography. Journal of Geophysical Research: Solid Earth, 121, 8068–8079. https://doi.org/10.1002/2016JB013131

Reed, C. A., Liu, K. H., Yu, Y., & Gao, S. S. (2017). Seismic anisotropy and mantle dynamics beneath the Malawi Rift Zone, East Africa. Tectonics, 36, 1338–1351. https://doi.org/10.1002/2017TC004519

Ringwood, A. E. (1975). Composition and petrology of the Earth's mantle (1ed., 672 pp.). New York: McGraw-Hill.

Ringwood, A. E. (1991). Phase transformations and their bearing on the constitution and dynamics of the mantle. Geochimica et Cosmochimica Acta, 55(8), 2083–2110. https://doi.org/10.1016/0016-7037(91) 90090-R

Ritsema, J., Nyblade, A. A., Owens, T. J., Langston, C. A., & VanDecar, J. C. (1998). Upper mantle seismic velocity structure beneath Tanzania, east Africa: Implications for the stability of cratonic lithosphere. Journal of Geophysical Research, 103(B9), 21,201–21,213. https://doi.org/10.1029/98JB01274

Ritsema, J., van Heijst, H. J., & Woodhouse, J. H. (1999). Complex shear wave velocity structure imaged beneath Africa and Iceland. Science, 286(5446), 1925–1931. https://doi.org/10.1126/science.286.5446.1925

Roberts, E. M., Stevens, N., O'Connor, P., Dirks, P., Gottfried, M. D., Clyde, W.,…Hemming, S. (2012). Initiation of the western branch of the East African Rift coeval with the eastern branch. Nature Geoscience, 5(4), 289–294. https://doi.org/10.1038/ngeo1432

Rychert, C. A., Hammond, J. O., Harmon, N., Kendall, J. M., Keir, D., Ebinger, C.,…Stuart, G. (2012). Volcanism in the Afar Rift sustained by decompression melting with minimal plume influence. Nature Geoscience, 5(6), 406–409. https://doi.org/10.1038/ngeo1455

Schmandt, B., & Humphreys, E. (2010). Complex subduction and small-scale convection revealed by body-wave tomography of the western United States upper mantle. Earth and Planetary Science Letters, 297(3), 435–445. https://doi.org/10.1016/j.epsl.2010.06.047

Schubert, G., Anderson, C., & Goldman, P. (1995). Mantle plume interaction with an endothermic phase change. Journal of Geophysical Research, 100(B5), 8245–8256. https://doi.org/10.1029/95JB0003

Shearer, P. M., & Masters, T. G. (1992). Global mapping of topography on the 660-km discontinuity. Nature, 335(6363), 791–796.

Slack, P. D., & Davis, P. M. (1994). Attenuation and velocity of P-waves in the mantle beneath the East African Rift, Kenya. Tectonophysics, 236(1–4), 331–358. https://doi.org/10.1016/0040-1951(94) 90183-X

Smith, W., & Wessel, P. (1990). Gridding with continuous curvature splines in tension. Geophysics, 55(3), 293–305. https://doi.org/10.1190/1.1442837

Stamps, D. S., Flesch, L., Calais, E., & Ghosh, A. (2014). Current kinematics and dynamics of Africa and the East African Rift System. Journal of Geophysical Research: Solid Earth, 119, 5161–5186. https://doi.org/10.1002/2013JB010717

Stamps, D. S., Iaffaldano, G., & Calais, E. (2015). Role of mantle flow in Nubia-Somalia plate divergence. Geophysical Research Letters, 42, 290–296. https://doi.org/10.1002/2014GL062515

Tauzin, B., Debayle, E., &Wittlinger, G. (2008). The mantle transition zone as seen by global Pds phases: No clear evidence for a thin transition zone beneath hotspots. Journal of Geophysical Research, 113, B08309. https://doi.org/10.1029/2007JB005364

Tauzin, B., & Ricard, Y. (2014). Seismically deduced thermodynamics phase diagrams for the mantle transition zone. Earth and Planetary Science Letters, 401, 337–346. https://doi.org/10.1016/j.epsl.2014.05.039

Tschauner, O., Ma, C., Beckett, J. R., Prescher, C., Prakapenka, V. B., & Rossman, G. R. (2014). Discovery of bridgmanite, the most abundant mineral in Earth a shocked meteorite. Science, 346(6213), 1100–1102. https://doi.org/10.1126/science.1259369

Vauchez, A., Dineur, F., & Rudnick, R. (2005). Microstructure, texture and seismic anisotropy of the lithospheric mantle above a mantle plume: Insights from the Labait volcano xenoliths (Tanzania). Earth and Planetary Science Letters, 232(3), 295–314. https://doi.org/10.1016/j.epsl.2005.01.024

Yu, Y., Gao, S. S., Moidaki, M., Reed, C. A., & Liu, K. H. (2015). Seismic anisotropy beneath the incipient Okavango rift: Implications for rifting initiation. Earth and Planetary Science Letters, 430, 1–8. https://doi.org/10.1016/j.epsl.2015.08.009

Yu, Y., Liu, K. H., Moidaki, M., Reed, C. A., & Gao, S. S. (2015). No thermal anomalies in the mantle transition zone beneath an incipient continental rift: Evidence from the first receiver function study across the Okavango Rift Zone, Botswana. Geophysical Journal International, 202(2), 1407–1418. https://doi.org/10.1093/gji/ggv229

# II. ABSENCE OF THERMAL INFLUENCE FROM THE AFRICAN SUPERSWELL AND CRATONIC KEELS ON THE MANTLE TRANSITION ZONE BENEATH SOUTHERN AFRICA: EVIDENCE FROM RECEIVER FUNCTION IMAGING

## ABSTRACT

The depths of the 410 km (d410) and 660 km (d660) discontinuities beneath southern Africa, which is presumably underlain by the lower-mantle African Superswell, are imaged in 1° radius consecutive circular bins using over 6400 P-to-S receiver functions (RFs) recorded by 130 seismic stations over a 27 yr period. When the IASP91 standard Earth model is utilized for moveout correction and time-depth conversion, a normal mantle transition zone (MTZ) thickness of 246 ± 7 km is observed, suggesting that the Superswell has no discernible effect on mantle transition zone temperature. Based on the negligible disparity of the mean MTZ thicknesses between on (246 ± 6 km) and off (246 ± 8 km) cratonic regions, we conclude that the deep Archean cratonic keels possess limited influence on MTZ thermal structure. The apparently shallower-than-normal MTZ discontinuities and the parallelism between the d410 and d660 are mostly the results of upper mantle high wave speed anomalies probably corresponding to a thick lithosphere with a mean thickness of about 245 km beneath the Kaapvaal and 215 km beneath the Zimbabwe cratons. In contradiction to conclusions from some of the previous studies, the resulting spatial distribution of the stacking amplitudes of the P-to-S converted phases at the discontinuities is inconsistent with the presence of an excessive amount of water in the MTZ and atop the d410.

# 1. INTRODUCTION

In spite of numerous observational and geodynamic modeling studies, mechanisms responsible for the anomalously high topography of southern Africa (Figure. 1) remain controversial (Lithgow-Bertelloni and Silver, 1998; Hu et al., 2018). One of the most commonly invoked hypotheses is the dynamic effects of the African Superswell, a low-seismic wave speed anomaly in the lower mantle beneath most of the southern hemispheric region of Africa and the neighboring oceanic areas of the African Plate (Lithgow-Bertelloni and Silver, 1998; Romanowicz and Gung, 2002; Ni et al., 2005). Whether the presumably high temperature from the Superswell has influenced the structure and deformation (especially rifting) of the upper mantle and mantle transition zone (MTZ), a layer of the Earth sandwiched between the 410 km (d410) and 660 km (d660) discontinuities, is still a debated subject (Ritsema et al., 1998; Priestley et al., 2008; Fishwick, 2010; Youssof et al., 2015). Another controversial issue is the depth extent of the cratonic keels and their influence on the temperature distribution in the upper mantle and MTZ. Beneath the Kaapvaal and Zimbabwe cratons, seismic surface wave studies suggested a lithospheric thickness of 160-250 km (Li and Burke, 2006; Chevrot and Zhao, 2007; Priestley et al., 2008; Schaeffer and Lebedev, 2013), while other studies especially those using teleseismic body-waves (James et al., 2001; Youssof et al., 2015) revealed a much thicker lithosphere, down to about 300 to 350 km, which may cause low temperature anomalies in the MTZ (Blum and Shen, 2004). The discrepancy is most likely caused by the limited resolving power and the consequent large uncertainties in the tomographic methods. Body-wave tomographic techniques

pervasively utilize relative (rather than absolute) travel time residuals and thus the resulting wave speed anomalies are relative to the mean over the region investigated (Foulger et al., 2013). Additionally, they suffer from vertical smearing due to the steep ray paths beneath the station. In contrast, surface-wave tomographic techniques produce absolute wave speed anomalies, and have inherently better vertical resolution but poorer horizontal resolution due to lateral smearing.

It has long been recognized that the topography of the d410 and d660 can provide independent constraints on the thermal and wave speed structures of the upper mantle and MTZ (Anderson, 1967; Flanagan and Shearer, 1998). The discontinuities reflect sudden changes in mineralogical phases, from olivine to wadsleyite at the d410, and from ringwoodite to bridgmanite at the d660 (Ringwood, 1975). Due to the opposite sign of the Clapeyron slopes (ranging from +1.5 MPa/K to +4.0 MPa/K for d410 and from -0.2 MPa/K to -4.0 MPa/K for d660; Tauzin and Ricard, 2014), high and low temperature anomalies can result in a thinner-than-normal and thicker-than-normal MTZ, respectively. In addition, the existence of water-saturated minerals in the MTZ could thicken the MTZ (Litasov et al., 2005), and an excessive amount of water tends to broaden the interval of the olivine-wadsleyite phase transition and reduce the sharpness of the d410 (Wood et al., 1996; Smyth and Frost, 2002; van der Meijde et al., 2003). Therefore, variations of the depths and sharpness of the d410 and d660 are effective indicators of spatial variations of thermal perturbations and water content anomalies in the vicinity of the MTZ discontinuities (Ringwood, 1975).

Several MTZ studies have been conducted in southern Africa with controversial conclusions. Gao et al. (2002) estimated an MTZ thickness of 245 km that is comparable

to the global average, and suggested that the lower-mantle African Superswell beneath southern Africa has no observable influence on the MTZ temperature. In contrast, Blum and Shen (2004) detected a 20 km thicker-than-normal MTZ beneath the Archean cratons in southern Africa, and interpreted it as the consequence of the extension of low-temperature, water-saturated Archean cratonic keels to the base of the MTZ. Another MTZ study (Niu et al., 2004) showed a normal MTZ thickness and suggested that the highly depleted root causes an approximately 20 km apparent uplift of the d410 and d660 relative to the global average beneath the Kaapvaal craton. Julia and Nyblade (2013) utilized 2557 P-to-S receiver functions (RFs) from 30 permanent broadband stations in Africa, including 7 stations in our study area (Figure.1), to image the MTZ discontinuities. They reported d410 depths in the range of 405 ±10 km, and d660 depths of 655 ±11 km with a mean MTZ thickness of 250 ±3 km beneath southern Africa. A recent MTZ study across the Okavango Rift zone conducted by Yu et al. (2015) revealed apparently shallower-than-normal MTZ discontinuities beneath the northern Kalahari Craton and a normal MTZ thickness beneath most of the study area, suggesting the absence of mantle plumes beneath the incipient rift.

The discrepancies in the results and conclusions from previous MTZ studies in southern Africa (Gao et al., 2002; Shen and Blum, 2003; Blum and Shen, 2004; Niu et al., 2004) are mostly the results of the limited amount of seismic data and the different methodologies applied by different research groups. In this study, we apply a non-plane wave assumption approach (Gao and Liu, 2014a) to an expanded data set recorded over the past 27 yr to provide an enhanced image of the MTZ discontinuities beneath southern Africa. Relative to methodologies based on the plane-wave assumption, our approach can

lead to sharper MTZ discontinuity arrivals and more accurately determined depths (Gao and Liu, 2014a). In addition to the unprecedented number of high-quality RFs used in this study, the spatial coverage is more extensive than the aforementioned regional-scale studies. The results provide tighter and more reliable constraints on the deep structure and temperature and water content of the upper mantle and MTZ beneath two of the oldest cratons on Earth, and the only continental area that is presumably underlain by a lower-mantle superswell.

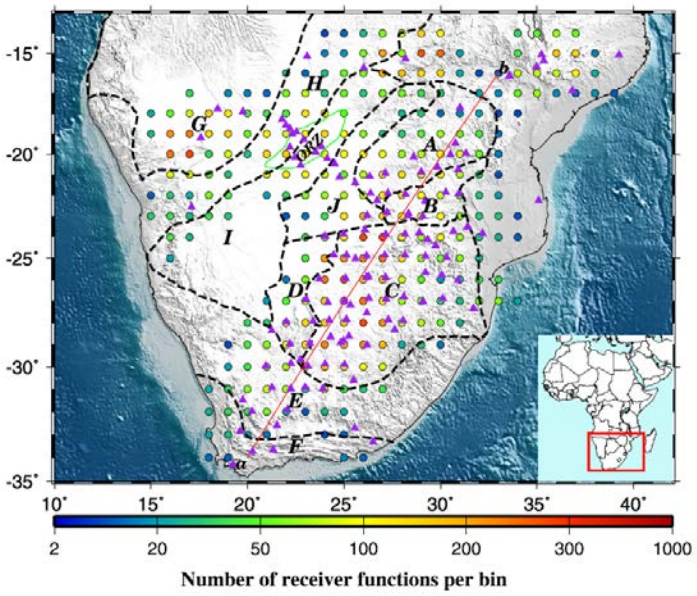


Figure 1 Topographic relief map of the study area showing the center of radius =1° bins (filled circles), and major tectonic boundaries (black dashed lines). The color of the circles represents the number of the RFs per bin. The purple triangles are seismic stations used in the study. The subareas include: A: Zimbabwe Craton; B: Limpopo Belt; C: Kaapvaal Craton; D: Kheiss Belt; E: Namaqua–Natal Belt; F: Cape Fold Belt; G: southern Congo Craton; H: Damara Belt; I: Rehoboth Province; J: Magondi Belt. Line a–b indicates the location of the profile shown in Figure.8. The red rectangle in the inset map shows the study area. (For interpretation of the colors in the figure(s), the reader is referred to the web version of this article.)

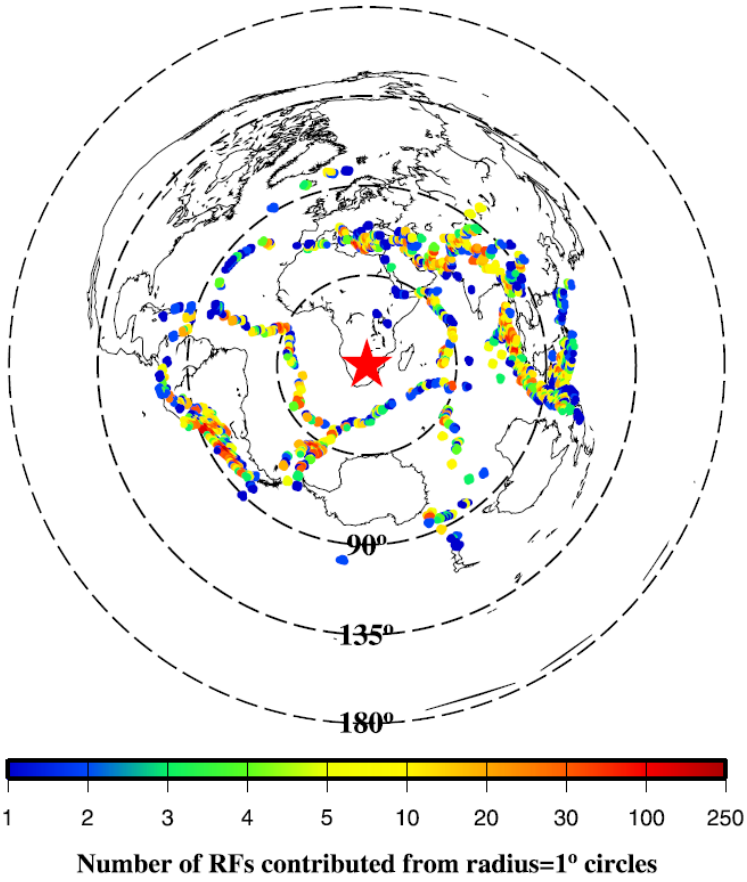


Figure 2 Spatial distribution of earthquake source areas. Each dot represents a radius =1° circular area. The distance between neighboring circles is 1°. The color of the dot represents the number of used RFs originated from earthquakes in the circle. The radius of the concentric dashed circles centered at the central part of the study area (star) indicates the epicentral distance.

## 2. DATA AND METHODS

### 2.1. DATA

All the available teleseismic data recorded by three-component broad-band stations located in the study area (14°S to 35°S, and 15°E to 40°E) during the period

between 1990 and 2017 were requested from the Incorporated Research Institutions for Seismology (IRIS) Data Management Center (DMC). The cut-off magnitude (Mc) for requesting data is determined based on the empirical equation to balance the quality and quantity of the data to be requested, i.e., $Mc=5.2+(\Delta-30.0)/(180.0-30.0)-D/700.0$, where Δ and Dare the epicentral distance (ranging from 30° to 100°) in degrees and focal depth in kilometers, respectively (Liu and Gao, 2010). The requested three-component seismograms with a length of 280 s, including 20 s before and 260 s after the theoretical arrival of the first compressional wave calculated based on the IASP91 Earth model, were filtered in the frequency band of 0.02-0.2Hz. Vertical-component seismograms were assessed for signal-to-noise ratio (SNR) using the method of Gao and Liu (2014a). If the SNR exceeded 4.0, the filtered 3-component seismograms were converted into radial RF following the procedure of Ammon (1991). Then the receiver functions were checked visually to reject the ones without a clear first P pulse, or those with abnormal arrivals that are stronger than the first P pulse. Among the 6907 three-component seismograms with a SNR greater than 4.0, a total of 6472 high-quality RFs recorded by 130 stations from 1302 events (Figure.2) were used in this study. In comparison, the number of RFs used by Gao et al. (2002) and Blum and Shen (2004) in the similar study area is 1300 and 3354, respectively.

## 2.2. MOVEOUT CORRECTION AND STACKING

The data processing steps and parameters used in this study are discussed in detail in Gao and Liu (2014b), and are briefly summarized here. The RFs are grouped into 1◦radius circular bins based on the locations of ray-piercing points computed at the

middle of the MTZ (535 km depth) according to the IASP91 Earth model. The bin size is approximately comparable to that of the first Fresnel zone of shear waves at the MTZ depths. Comparing with the traditional common conversion point stacking approach of grouping the RFs for each depth of assumed discontinuities (e.g., Dueker and Sheehan, 1998; Liu et al., 2003), this approach ensures that both MTZ discontinuities are sampled by the same RFs, minimizing possible biases on the resulting MTZ thickness by upper mantle wave speed heterogeneities (Gao and Liu, 2014b; Dahm et al., 2017).

RFs in each of the bins are moveout corrected and stacked using a non-plane wave assumption approach (Gao and Liu, 2014a) to form a depth series in the depth range of 300-800 km with a vertical grid size of 1 km under the 1-D IASP91 Earth model. Relative to approaches assuming a plane wave front, the non-plane wave assumption approach can more accurately determine the discontinuity depths and result in sharper discontinuity images due to the consideration of the difference in ray parameters between the direct P-wave and the converted S-wave. Only the results from bins with 10 or more RFs are used for the study. The optimal depth of the d410 corresponds to that of the maximum stacking amplitude in the depth range of 380-440 km, and that of the d660 corresponds to the depth of the largest arrival in the range of 630-690 km. For a small fraction (about 5%) of the bins, multiple arrivals with comparable amplitudes are present in the search window. For these bins, the search ranges are manually adjusted to maintain spatial continuity. The mean and standard deviation of the MTZ discontinuity depths and MTZ thickness for each bin are obtained following a bootstrap resampling procedure with 50 resampling iterations (Efron and Tibshirani, 1986).

## 2.3. WAVE SPEED CORRECTION

Since the 1-D IASP91 standard Earth model is utilized to moveout-correct the RFs, the resulting MTZ discontinuity depths are apparent instead of true depths, which can be obtained if P-and S-wave speed models extending through the crust, upper mantle and MTZ are available in digital form. If only the $V_p$ ($V_s$) model is available, a $\gamma$ factor, which is defined as d ln ($V_s$)/d ln ($V_p$), is assumed or searched (e.g., Gao and Liu, 2014b) to generate the $V_s$ ($V_p$) model.

In this study, two wave speed models (Schaeffer and Lebedev, 2013and updated in 04/2018; Youssof et al., 2015), which include both $V_p$ and $V_s$ anomalies in digital forms, are used to conduct the wave speed corrections by following the procedure of Gao and Liu (2014b) for correcting the MTZ discontinuity depths beneath the contiguous United States. To perform the correction, the wave speed anomalies are smoothed using the cubic B-spline function, and the average P-and S-wave speeds are calculated in radius =1° cylinders with a 10 km thickness for the depth range of 0-700 km. Lastly, the equation (Gao and Liu, 2014b)

$$H_T = \frac{(V_{so}+\delta V_s)\times(V_{po}+\delta V_p)}{V_{po}+\delta V_p - V_{so} - \delta V_s} \times \frac{V_{po}-V_{so}}{V_{po}\times V_{so}} H_A \quad (1)$$

is applied to convert the apparent depths ($H_A$) into true depths ($H_T$), where $V_{p0}$ and $V_{s0}$ are the mean P-and S-wave speeds in the layer in the standard Earth model, and $\delta V_p$ and $\delta V_s$ are the absolute P-and S-wave speed anomalies.

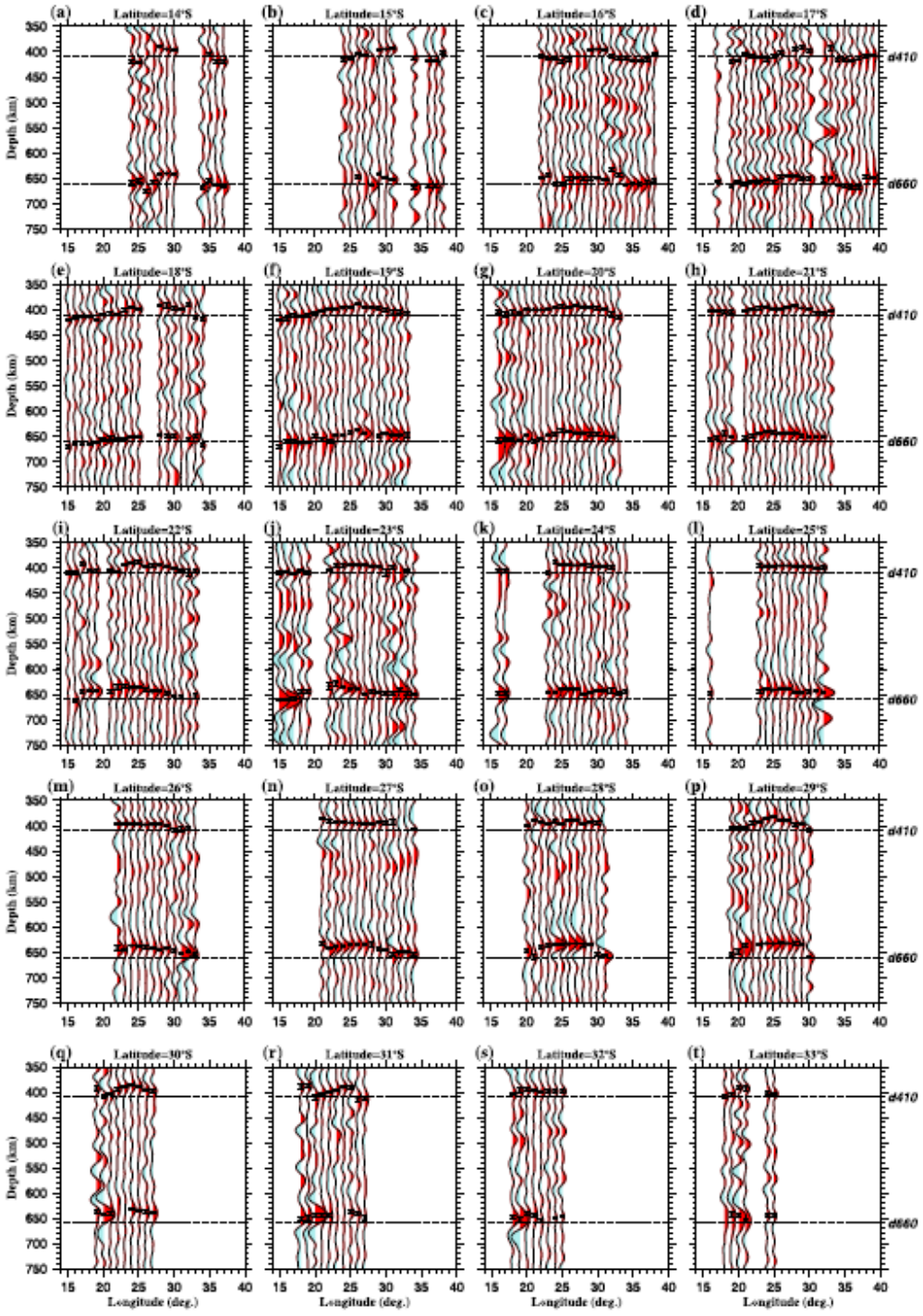


Figure 3 Results of stacking moveout-corrected RFs within each bin plotted along 20 latitudinal profiles. The black traces show the depth series averaged over all the 50 bootstrap iterations. The circles and error bars respectively represent the resulting apparent depths and standard deviations of the depths of the MTZ discontinuities.

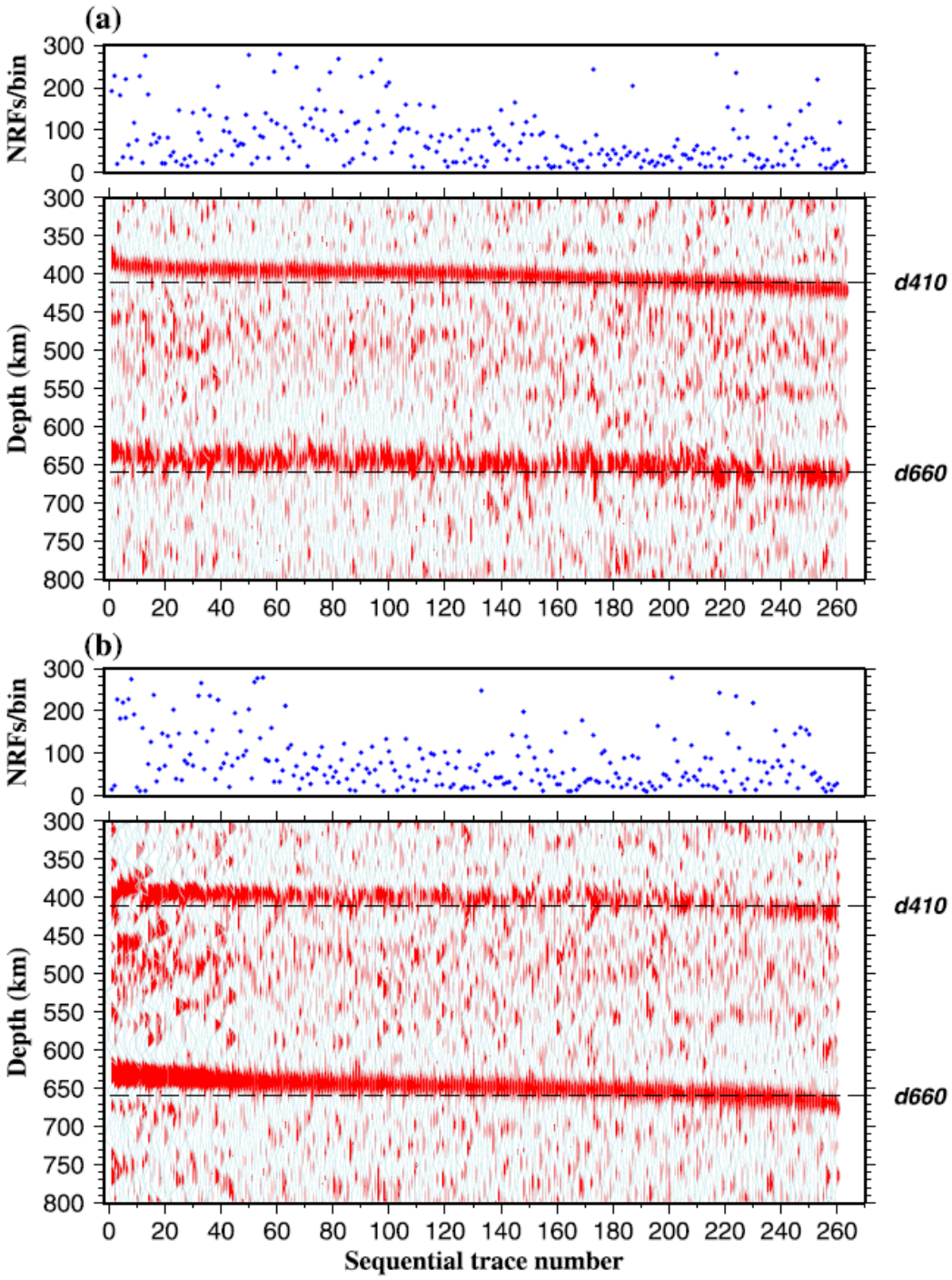


Figure 4 (a) Results of stacking all available normal moveout corrected RFs from 1° radius bins with a minimum of 10 high-quality RFs, plotted against the sequentially increasing depth of the d410. (b) Similar to (a) but against the sequentially increasing depth of the d660. The top panel in (a) and (b) shows the number of RFs per bin.

# 3. RESULTS

All the 20 latitudinal profiles (from 14°S to 33°S) of the resulting depth series in the study area are shown in Figure.3. Robust peaks for the d410 or d660 are observed in a total of 281 bins (Figure.4), among which 263, 260, and 242 possess reliable arrivals from the d410, d660, and both, respectively.

## 3.1. APPARENT DISCONTINUITY DEPTHS AND MTZ THICKNESS

The resulting apparent d410 and d660 depths (Figures.5a and 5b; Table S1) show systematic spatial variations and are positively correlated with a cross correlation coefficient (XCC) of 0.7 (Figure.6). On average, the Kaapvaal and Zimbabwe cratons show a 10-15 km (Figure.5 and Table S2) apparent uplift of both MTZ discontinuities with a maximum value of about 30 km, while the surrounding Proterozoic fold belts demonstrate normal discontinuity depths. For the entire study area, the mean apparent depths are 401±9 km and 648±9 km for the d410 and d660, respectively. The corresponding values are 395±5 km and 640±7 km for the Kaapvaal Craton, and 398±5 km and 647±4 km for the Zimbabwe Craton (Table S2). The boundary of the area with apparently shallower MTZ discontinuities follows the surface expression of the Kaapvaal Craton well, but shifts to the west by about 200 km from the western boundary of the surface expression of the Zimbabwe Craton (Figure.5). In spite of the obvious difference in the apparent d410 and d660 depths between on and off cratonic regions (Table S2), a negligible disparity of the mean MTZ thickness between on (246±6 km) and off (246±8 km) cratonic regions is observed in the study area (Figure.5c).

The average MTZ thickness is 246±7 km (Figure.5c), which is statistically identical to the global average (which ranges from 240 to 250 km) reported by previous global scale studies (Flanagan and Shearer, 1998; Gu et al., 1998; Tauzin et al., 2008). The depths and thickness measurements are generally consistent with most of the previous MTZ studies targeting the Kaapvaal and Zimbabwe cratons (Gao et al., 2002; Niu et al., 2004; Julia and Nyblade, 2013) and the Okavango Rift zone (Yu et al., 2015). They are also in agreement with results from several stations in southern Africa from global scale studies (Flanagan and Shearer, 1998; Chevrot et al., 1999;Tauzin et al., 2008), but are inconsistent with the results of Shen and Blum (2003) and Blum and Shen (2004) who reported a 20 km thicker-than-normal MTZ beneath the Archean cratons in southern Africa due to shallowing of the d410 and deepening of the d660, and interpreted it as the consequence of lowered temperature originating from the cold deep cratonic keels.

### 3.2. SPATIAL VARIATION OF STACKING AMPLITUDES

We use the ratio (R) between the amplitude of the P-to-S converted phase (Pds) from an MTZ discontinuity and that of the direct P -wave as a measure of the wave speed contrast across, and the sharpness of, the discontinuity (Figure. 7). For the entire study area, the average R value is 0.021±0.008 for the d410 and 0.023±0.007 for the d660, both are greater than that beneath tectonically stable central North America (0.018±0.005 for the d410 and 0.019±0.004 for the d660), and active western North America (0.015±0.005 for the d410 and 0.016±0.004 for the d660) (Gao and Liu, 2014b). The stronger stacking amplitudes of the Pds observed beneath southern Africa might indicate the existence of a

less attenuative upper mantle relative to western and central North America. Under this assumption, the absence of a clear correspondence between the R observations and the tectonic provinces (Figure. 7) may suggest that there is no obvious age dependence of upper mantle attenuation.

### 3.3. WAVE SPEED CORRECTED DEPTHS

The P- and S-wave speed models of Schaeffer and Lebedev (2013) and Youssof et al. (2015), which cover the entire and most of the study area, respectively, are utilized for wave speed corrections in this study. As detailed in Gao and Liu (2014b), the accuracy of the wave speed correction can be estimated using the degree of reduction in the XCC between the corrected depths of d410 and d660. This is primarily because of the fact that wave speed anomalies in the upper mantle (above the d410) lead to positive correlations between the apparent depths of the two discontinuities (Figure. 6), while thermally or water content induced wave speed anomalies in the MTZ normally result in negative correlations between the true depths of the two discontinuities. Therefore, if the wave speed anomalies used for the correction are precisely determined, the resulting XCC should reduce to zero if there is no thermal, water content, or other anomalies that affect the depths of the discontinuities; the XCC becomes a negative value if thermal or water content anomalies exist in the MTZ.

The corrected depths and MTZ thickness as well as the resultant XCC values are shown in Figures. S1 and S2. Although the correction by using the models of Schaeffer and Lebedev (2013) reduces the XCC from 0.7 before the correction to 0.58 afterward, the corrected d410 and d660 depths are still positively correlated. The XCC between the

corrected depths by using the models of Youssof et al. (2015) only reduces marginally, from 0.70 to 0.67, indicating that the wave speed corrections did not effectively remove the influence of upper mantle wave speed anomalies on the apparent depths. In comparison, the XCC reduced from 0.84 to 0.41 after the same wave speed correction procedure was applied for the contiguous United States (Gao and Liu, 2014b). We also tried a few other wave speed models (e.g., Priestley et al., 2008) with available $V_p$ and/or $V_s$ anomalies in digital form, and found that none of them was able to significantly reduce the XCC.

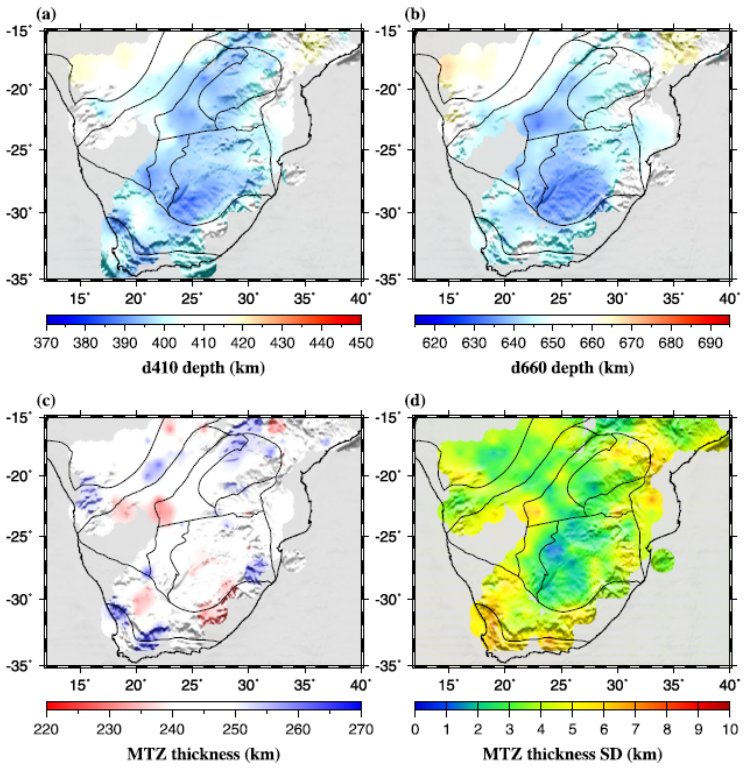


Figure 5 (a) Spatial distribution of resulting d410 depths. (b) Same as (a) but for the d660. (c) MTZ thickness measurements. (d) Standard deviation (SD) of the MTZ thickness measurements.

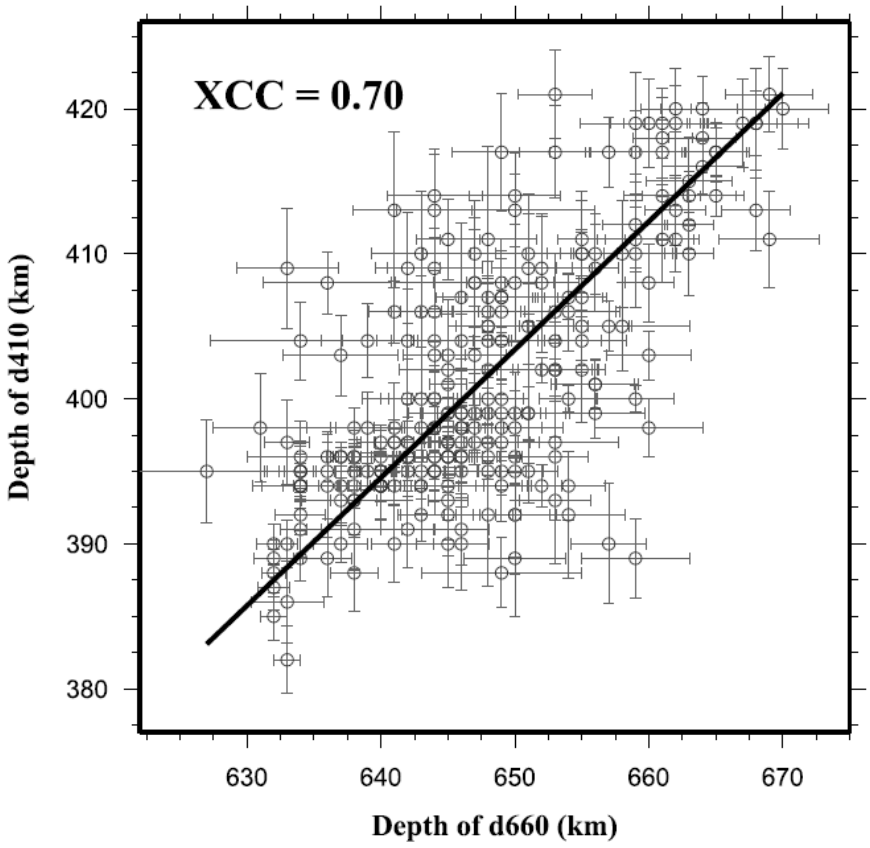


Figure 6 Correlation plot of apparent d410 and d660 depths. The line indicates the optimal bivariate regression with a cross-correlation coefficient of 0.70.

The small reduction in the XCCs between the corrected d410 and d660 depths suggests that the wave speed corrected depths are not reliable, most likely due to large uncertainties in the models and underestimation of the amplitude of the wave speed anomalies. Additionally, considerable discrepancies are present among existing wave speed models (e.g., Figure. S3) and thus it is difficult to determine which of the wave speed corrected results is the most realistic one. Therefore, in the following we discuss the wave speed structure in the upper mantle and the thermal and water content anomalies

in the vicinity of the MTZ discontinuities using the apparent (Figure. 5) rather than the wave speed corrected (Figures. S1 and S2) depths.

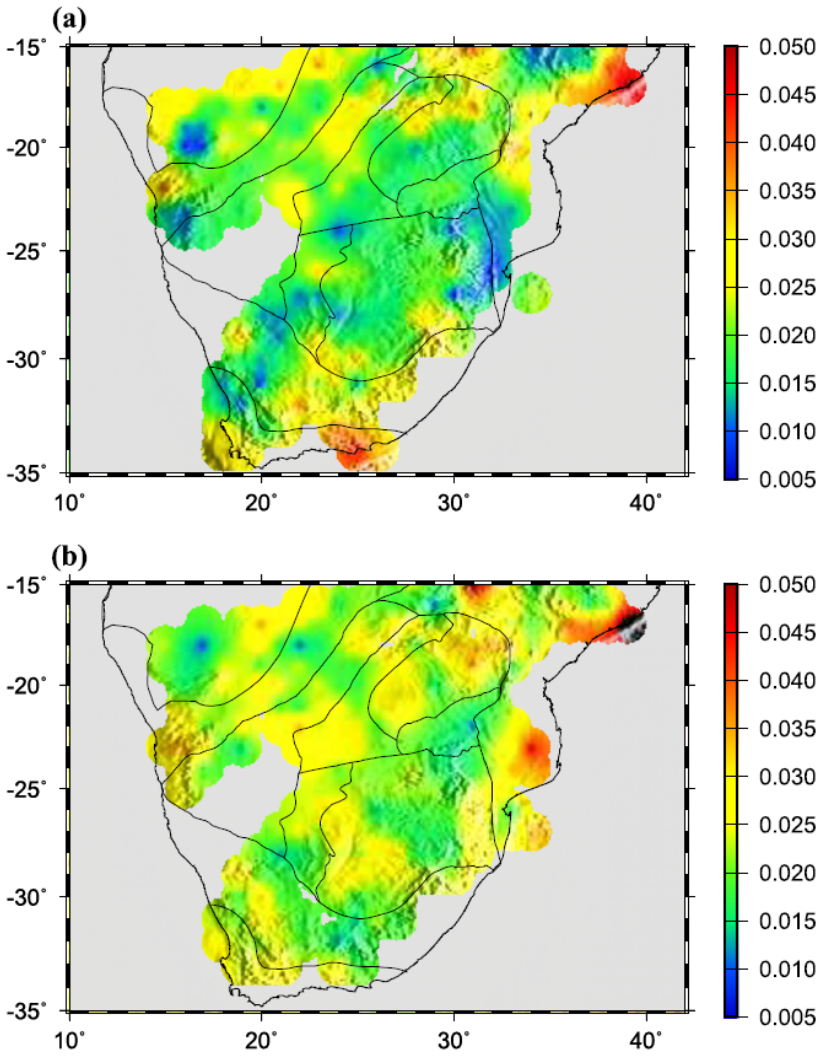


Figure 7 Stacking amplitude (relative to that of the direct P-wave) for (a) d410 and (b) d660.

# 4. DISCUSSION

## 4.1. THERMAL STRUCTURE OF THE MTZ

The simplest explanation for the observed nearly normal MTZ thickness beneath most of southern Africa (Figure. 5c) is that there is no discernible temperature anomaly in the MTZ. However, some specific combinations of temperature and water content anomalies may lead to a normal MTZ thickness (Reed et al., 2016; Sun et al., 2017). The first scenario is when the effect of water (which can uplift the d410 and depress the d660; Litasov et al., 2005) and that of higher-than-normal temperature (which has an opposite effect than water on the discontinuities) coincidentally cancel each other, leading to a normal MTZ thickness. However, these two factors are unlikely to cancel each other almost everywhere across this study area with a diverse set of tectonic provinces and lithospheric ages and thicknesses (Figure. 1). In addition, the lack of an anomalously high amount of water in the MTZ is consistent with the observation that a low wave speed layer is not observed atop the d410 beneath southern Africa (Tauzin et al., 2010), a conclusion that is supported by the stacked RFs from this study (Figures. 3 and 8).

The second scenario to produce a normal MTZ thickness is when the amount of uplift of the d660 caused by the higher-than-normal temperature from the lower mantle superswell matches that of the d410 caused by the lower-than-normal temperature from the deep cratonic keels. However, because the superswell covers a much larger area than the cratons (Ritsema et al., 1999), thinner-than-normal MTZ thickness should be expected beneath the off cratonic areas due to the absence of the effect of the keels. This

prediction is inconsistent with the observed MTZ thicknesses, which are similar between cratonic (246±6 km) and off cratonic (246±8 km) areas (Figure. 5c and Figure. 8).

Therefore, we conclude that the presence of an excessive amount of water or significant thermal anomalies in the MTZ is unlikely. This in turn suggests that neither the lower-mantle African Superswell nor the cratonic keels have a discernible effect on the MTZ temperature. The conclusion that the thermal influence of the cratonic keels is limited to the upper mantle and does not extend to the MTZ is consistent with most previous tomographic studies (James et al., 2001; Wittlinger and Farra, 2007; Priestley et al., 2008; Fishwick, 2010; Youssof et al., 2015). Similarly, the observed dominantly normal MTZ thickness beneath cratonic areas in North America indicates the absence of significant influence of cratonic keels on the thermal structure of the MTZ (Thompson et al., 2011; Gao and Liu, 2014a).

## 4.2. UPPER MANTLE WAVE SPEED AOMALIES DERIVED FROM THE APPARENT DISCONTINUITY DEPTHS

As discussed in the previous section, large scale significant thermal and water content anomalies are unlikely to exist in the MTZ beneath southern Africa. In addition, the parallelism between the shallower-than-normal apparent depths of the d410 and d660 (Figure.5) suggests that high wave speed anomalies situated above the d410 are the simplest explanation for the apparent uplift of both discontinuities. Under the assumption that the true depth of the d410 is 410 km, the apparent depth of the d410 can be used to estimate the mean upper mantle P- and S-wave speed anomalies for an assumed $\gamma$ factor (Gao and Liu, 2014b). For the following calculations, we assume that $\gamma$=1.7, a value that

was estimated for the central and eastern United States (Gao and Liu, 2014b). Application of a different factor would change the absolute wave speed anomalies, but not their spatial variations (Reed et al., 2016).

The resulting average upper mantle P-wave speed anomalies calculated using the relationship between the apparent depths of the MTZ discontinuities and wave speed anomalies (Equation (1)) correspond well with major tectonic boundaries (Figure.9). The mean upper mantle P-wave speed anomaly required to correct the observed average apparent d410 depth (401±8 km) to the depth of 410 km is 0.84±0.84% for the entire study area, and 1.49±0.49%, 1.20±0.49%, and 0.83±0.56% for the Kaapvaal Craton, Zimbabwe Craton, and Limpopo Belt, respectively.

While the spatial variations of the derived wave speed anomalies (Figure.9) are in general agreement with those from most seismic tomographic results (James et al., 2001; Schaeffer and Lebedev, 2013; Figure. S3), the absolute amplitude of the variations obtained from this study is significantly greater than those from seismic tomographic investigations. Such a reduction in the amplitude in tomographically-derived wave speed models could be the result of a high damping factor that is necessary to stabilize the inversion, and for some previous studies, the use of relative rather than absolute travel time residuals (Foulger et al., 2013).

Under the assumption that the wave speed variations derived above are entirely caused by variations in lithospheric thickness, in the following we estimate the depth of the lithosphere–asthenosphere boundary (LAB) across the study area. To perform this task, a reference location on Earth with normal upper mantle wave speeds, a well imaged d410 with a nearly normal depth, and a reliably determined lithospheric thickness is

needed. These conditions are satisfied by most parts of the eastern U.S., where normal apparent d410 depths and near zero average wave speed anomalies in the upper mantle (see Figure.4a in Gao and Liu, 2014b) have been suggested. Additionally, for the easternmost U.S., the most recent S-to-P receiver function study revealed a lithospheric thickness of ~90 km (Liu and Gao, 2018), which is consistent with most of the previous studies (e.g., Rychert et al., 2007; Fischer et al., 2010).

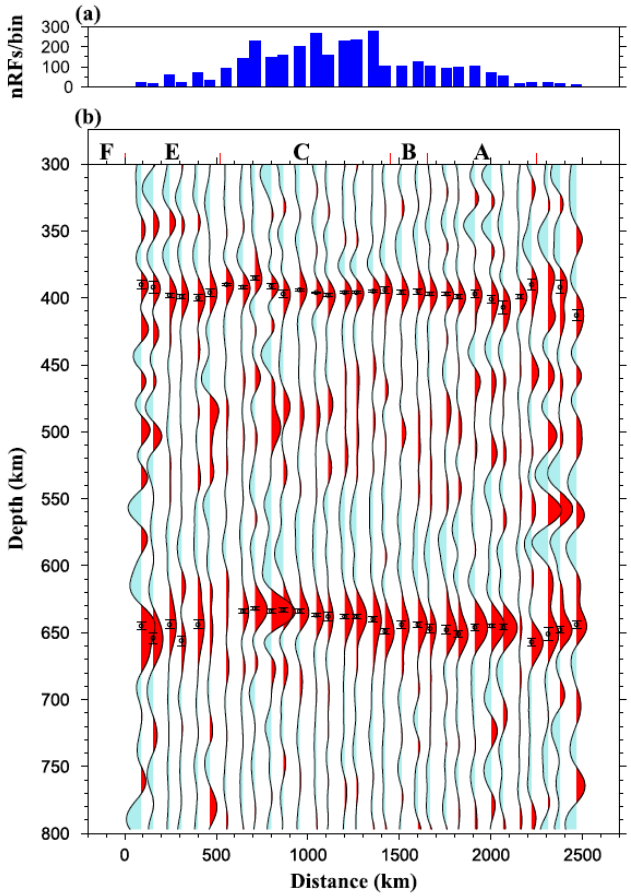


Figure 8 (a) Number of RFs in bins within a 150 km wide band centered at Profile a-b shown in Figure.1. (b) Resulting depth series in the bins. The letters at the top indicate the five subareas in Figure.1.

Once the reference location with normal velocities and d410 depth is determined, the mean lithospheric thickness (L) beneath a given area with a mean relative upper mantle $V_p$ anomaly of A (in percent) can be estimated by partitioning the anomaly from a layer with a thickness of 410 km to a layer of (L−90) km with a $V_p$ anomaly of C% determined in Section 4.2, i.e., (L−90)/A=410/C+90, where 90 is the thickness of the lithosphere in km at the reference location. Obviously, for a fixed wave speed anomaly, a larger wave speed contrast requires a smaller difference in LAB depth relative to the reference location.

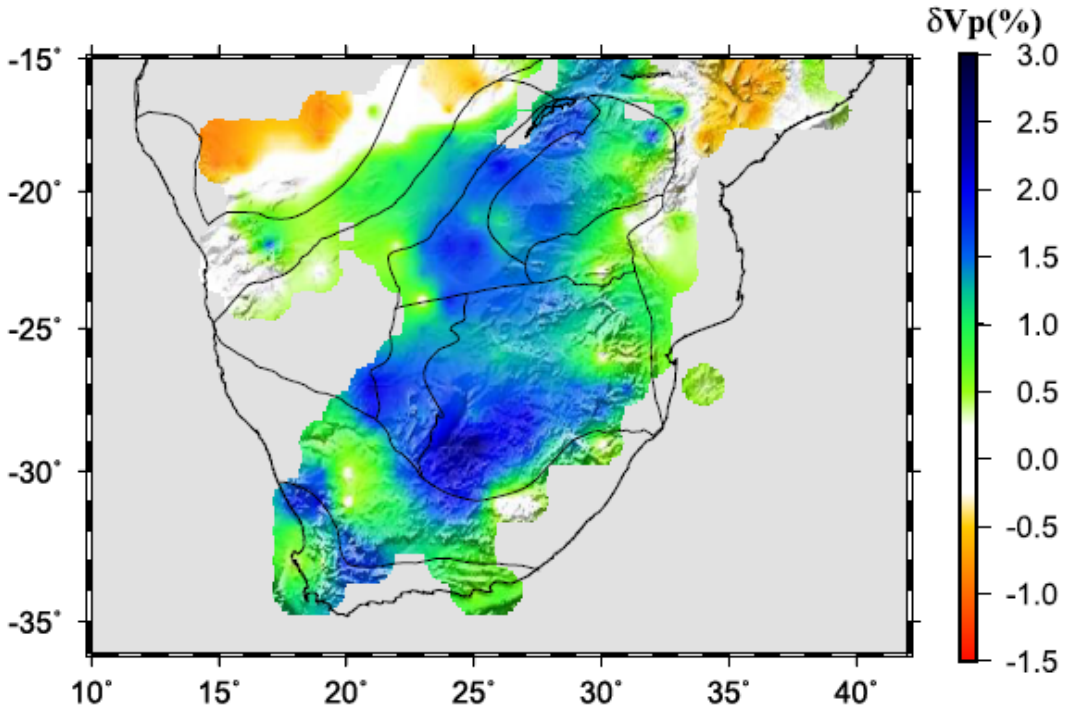


Figure 9 Required P-wave velocity anomalies (relative to the IASP91 Earth model) in order to correct the observed apparent d410 depths to a uniform true depth of 410 km.

Figure.10 shows the resulting mean lithospheric thickness plotted against assumed C values beneath the Kaapvaal and Zimbabwe cratons and the Limpopo Belt, calculated based on the mean upper mantle $V_p$ anomalies shown in Table S2. If we assumed that the $V_p$ contrast between the lithosphere and the asthenosphere is 4%, a value suggested in numerous previous studies (e.g., Li et al., 2003; Rychert et al., 2007; Eaton et al., 2009; Yu et al., 2015), the lithospheric thickness would be about 245 km for the Kaapvaal Craton (Figure.10). This value is generally consistent with most of the previous tomographic and receiver function studies (James et al., 2001; Niu et al., 2004; Wittlinger and Farra, 2007; Youssof et al., 2015). On the other hand, if the high wave speed root beneath the Kaapvaal Craton only extends to less than 200km (Priestley et al., 2008; Fishwick, 2010), the required $V_p$ contrast between the lithosphere and asthenosphere would be greater than 5.6%, a high value that is not suggested by the existing studies for the area. The resulting lithospheric thickness beneath the Zimbabwe Craton and Limpopo Belt is about 215 km and 175 km, respectively, which are also comparable to most of the previous seismic tomographic studies (Li and Burke, 2006; Chevrot and Zhao, 2007). It must be emphasized that the estimated lithospheric thicknesses are under the assumption that there is a sharp boundary between the lithosphere and the asthenosphere, while in reality a gradual rather than sharp transitional zone between the two layers might be present (e.g., Fischer et al., 2010). In this case the estimated depths approximately represent the center of the transitional layer.

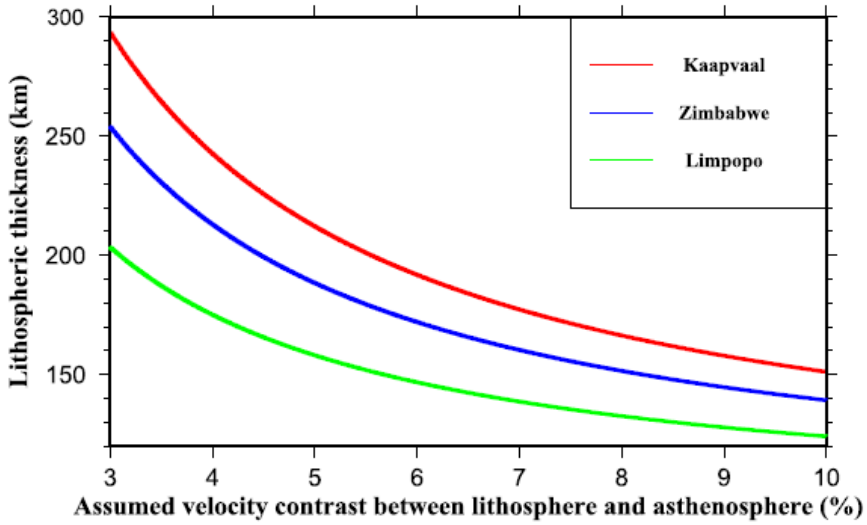


Figure 10 Estimated lithospheric thickness as a function of P-wave velocity contrast across the LAB beneath the Kaapvaal Craton (red line), Zimbabwe Craton (blue line) and Limpopo Belt (green line).

## 5. CONCLUSIONS

Using an unprecedented number of RFs recorded in southern Africa over the past 27 yr, we imaged the topography of the d410 and d660 under the non-plane wave assumption. Beneath most of the study area, the d410 and d660 are apparently shallower than the global average and are parallel to each other, suggesting high wave speed anomalies in the upper mantle. The shallower-than-normal MTZ discontinuities can be sufficiently explained by variations in lithospheric thickness. The resulting MTZ thickness is comparable to the globally averaged value of 250 km, and there is no discernible difference between the on and off cratonic regions. The sharp arrivals associated with both the d410 and d660 imply the absence of an excessive amount of water in the MTZ, and the lack of a robust negative arrival above the d410 is inconsistent

with the presence of a water-saturated layer atop the d410. The observations suggest that both the cratonic keels and the lower mantle African Superswell have a limited influence on the thermal structure of the mantle transition zone beneath southern Africa.

## ACKNOWLEDEGEMENTS

Data used in this study were requested from the IRIS DMC (last accessed: August 2017). We thank two anonymous reviewers and the editor for suggestions that significantly improved the manuscript. The study was partially supported by the Continental Dynamics Program of the U.S. National Science Foundation under grants No. 1009946 and 1321656 to S.G. and K.L., and by the China Scholarship Council to M.S. under award 201508230075.

## APPENDIX A. SUPPLEMENTARY MATERIAL

Supplementary material related to this article can be found online at https://doi.org/10.1016 /j.epsl.2018.09.012.

## REFERENCES

Ammon, C.J., 1991. The isolation of receiver effects from teleseismic P waveforms. Bull. Seismol. Soc. Am.81, 2504–2510.

Anderson, D.L., 1967. Phase changes in the upper mantle. Science157, 1165–1173.

Blum, J., Shen, Y., 2004. Thermal, hydrous, and mechanical states of the mantle transition zone beneath southern Africa. Earth Planet. Sci. Lett.217, 367–378. http://doi.org/10.1016/S0012-821X(03)00628 -9.

Chevrot, S., Vinnik, L., Montagner, J.P., 1999. Global-scale analysis of the mantle Pds phases. J. Geophys. Res., Solid Earth104, 20203–20219. http://doi.org/10.1029/1999JB900087.

Chevrot, S., Zhao, L., 2007. Multiscale finite-frequency Rayleigh wave tomography of the Kaapvaal craton. Geophys. J. Int.169, 201–215. http://doi.org/10.1111/j.1365-246X.2006.03289.x.

Dahm, H.H., Gao, S.S., Kong, F., Liu, K.H., 2017. Topography of the mantle tran-sition zone discontinuities beneath Alaskaand its geodynamic implications: constraints from receiver function stacking. J. Geophys. Res., Solid Earth122, 10352–10363. http://doi.org/10.1002/2017JB014604.

Dueker, K.G., Sheehan, A.F., 1998. Mantle discontinuity structure beneath the Col-orado rocky mountains and high plains. J. Geophys. Res., Solid Earth103, 7153–7169. http://doi.org/10.1029/97JB03509.

Eaton, D.W., Darbyshire, F., Evans, R.L., Grütter, H., Jones, A.G., Yuan, X., 2009. The elusive lithosphere–asthenosphere boundary (LAB) beneath cratons. Lithos109, 1–22. http://doi.org/10.1016/j.lithos.2008.05.009.

Efron, B., Tibshirani, R., 1986. Bootstrap methods for standard errors, confidence in-tervals, and other measures of statistical accuracy. Stat. Sci.1, 54–75. https://doi.org/10.1214/ss/1177013815.

Fischer, K.M., Ford, H.A., Abt, D.L., Rychert, C.A., 2010. The lithosphere–asthenosphere boundary. Annu. Rev. Earth Planet. Sci.38, 551–575. https://doi.org /10.1146 /annurev-earth-040809-152438.

Fishwick, S., 2010. Surface wave tomography: imaging of the lithosphere–asthenosphere boundary beneath central and southern Africa? Lithos120, 63–73. http://doi.org/10.1016/j.lithos.2010.05.011.

Flanagan, M.P., Shearer, P.M., 1998. Global mapping of topography on transition zone velocity discontinuities by stacking SS precursors. J. Geophys. Res., Solid Earth103, 2673–2692. http://doi.org/10.1029/97JB03212.

Foulger, G.R., Panza, G.F., Artemieva, I.M., Bastow, I.D., Cammarano, F., Evans, J.R., Hamilton, W.B., Julian, B.R., Lustrino, M., Thybo, H., Yanovskaya, T.B., 2013. Caveats on tomographic images. Terra Nova25, 259–281. http://doi.org/10.1111/ter.12041.

Gao, S.S., Liu, K.H., 2014a. Imaging mantle discontinuities using multiply-reflected P-to-Sconversions. Earth Planet. Sci. Lett.402, 99–106. http://doi.org/10.1016/j.epsl.2013.08.025.

Gao, S.S., Liu, K.H., 2014b. Mantle transition zone discontinuities beneath the contiguous United States. J. Geophys. Res., Solid Earth119, 6452–6468. http://doi.org/10.1002/2014JB011253.

Gao, S.S., Silver, P.G., Liu, K.H., 2002. Mantle discontinuities beneath southern Africa. Geophys. Res. Lett.29, 129–1–129-4. http://doi.org/10.1029/2001GL013834.

Gu, Y., Dziewonski, A.M., Agee, C.B., 1998. Global de-correlation of the topography of transition zone discontinuities. Earth Planet. Sci. Lett.157, 57–67. http://doi.org/10.1016/S0012-821X(98)00027 -2.

Hu, J., Liu, L., Faccenda, M., Zhou, Q., Fischer, K.M., Marshak, S., Lundstrom, C., 2018. Modification of the Western Gondwana craton by plume–lithosphere interac-tion. Nat. Geosci.11, 203–210. https://doi.org/10.1038/s41561-018-0064-1.

James, D., Fouch, M., VanDecar, J., Van Der Lee, S., 2001. Tectospheric structure beneath southern Africa. Geophys. Res. Lett.28, 2485–2488. http://doi.org/10.1029/2000GL012578.

Julia, J., Nyblade, A.A., 2013. Probing the upper mantle transition zone under Africa with P520sconversions: implications for temperature and composition. Earth Planet. Sci. Lett.368, 151–162. http://doi.org/10.1016/j.epsl.2013.02.021.

Li, A., Burke, K., 2006. Upper mantle structure of southern Africa from Rayleigh wave tomography. J. Geophys. Res., Solid Earth111, B10303. http://doi.org/10.1029/2006JB004321.

Li, A., Forsyth, D.W., Fischer, K.M., 2003. Shear velocity structure and azimuthal anisotropy beneath eastern North America from Rayleigh wave inversion. J. Geophys. Res., Solid Earth108, 2362. http://doi.org/10.1029/2002JB002259.

Litasov, K.D., Ohtani, E., Sano, A., Suzuki, A., Funakoshi, K., 2005. Wet subduction versus cold subduction. Geophys. Res. Lett.32, L13312. http://doi.org/10.1029/2005GL022921.

Lithgow-Bertelloni, C., Silver, P.G., 1998. Dynamic topography, plate driving forces and the African superswell. Nature395, 269. http://doi.org/10.1038/26212.

Liu, K.H., Gao, S.S., 2010. Spatial variations of crustal characteristics beneath the Hoggar swell, Algeria, revealed by systematic analyses of receiver functions from a single seismic station. Geochem. Geophys. Geosyst.11, Q08011. http://doi.org/10 1029/2010GC003091.

Liu, K.H., Gao, S.S., Silver, P.G., Zhang, Y., 2003. Mantle layering across central South America. J. Geophys. Res., Solid Earth108, 2510. http://doi.org/10.1029/2002JB002208.

Liu, L., Gao, S., 2018. Lithospheric layering beneath the contiguous United States constrained by S-to-P receiver functions. Earth Planet. Sci. Lett.495, 79–86. https://doi.org/10.1016/j.epsl.2018.05.012.

Ni, S., Helmberger, D.V., Tromp, J., 2005. Three-dimensional structure of the African superplume from waveform modeling. Geophys. J. Int.161, 283–294. http://doi.org/10.1111/j.1365-246X.2005.02508.x.

Niu, F., Levander, A., Cooper, C.M., Lee, C.-T.A., Lenardic, A., James, D.E., 2004. Seismic constraints on the depth and composition of the mantle keel beneath the Kaapvaal craton. Earth Planet. Sci. Lett.224, 337–346. http://doi.org/10.1016/j.epsl.2004.05.011.

Priestley, K., McKenzie, D., Debayle, E., Pilidou, S., 2008. The African upper man-tle and its relationship to tectonics and surface geology. Geophys. J. Int.175, 1108–1126. http://doi.org/10.1111/j.1365-246X.2008.03951.x.

Reed, C.A., Gao, S.S., Liu, K.H., Yu, Y., 2016. The mantle transition zone beneath the Afar Depression and adjacent regions: implications for mantle plumes and hydration. Geophys. J. Int.205, 1756–1766. http://doI.org/10.1093/gji/ggw116.

Ringwood, A.E., 1975. Composition and Petrology of the Earth's Mantle, vol. 672, 1st ed. McGraw–Hill, New York.

Ritsema, J., Nyblade, A.A., Owens, T.J., Langston, C.A., VanDecar, J.C., 1998. Up-per mantle seismic velocity structure beneath Tanzania, east Africa: implica-tions for the stability of cratonic lithosphere. J. Geophys. Res., Solid Earth103, 21201–21213. http://doi.org/10.1029/98JB01274.

Ritsema, J., van Heijst, H.J., Woodhouse, J.H., 1999. Complex shear wave velocity structure imaged beneath Africa and Iceland. Science286, 1925–1928. http://doi.org/10.1126/science.286.5446.1925.

Romanowicz, B., Gung, Y., 2002. Superplumes from the core–mantle boundary to the lithosphere: implications for heat flux. Science296, 513–516. http://doi.org/10.1126/science.1069404.

Rychert, C.A., Rondenay, S., Fischer, K.M., 2007. P-to-Sand S-to-Pimaging of a sharp lithosphere–asthenosphere boundary beneath eastern North America. J.Geophys. Res., Solid Earth112, B08314. http://doi.org/10.1029/2006JB004619.

Schaeffer, A.J., Lebedev, S., 2013. Global shear speed structure of the upper mantle and transition zone. Geophys. J. Int.194, 417–449. https://doi.org/10.1093/gjI/ggt095.

Shen, Y., Blum, J., 2003. Seismic evidence for accumulated oceanic crust above the 660-km discontinuity beneath southern Africa. Geophys. Res. Lett.30, 1925. http://doi.org/10.1029/2003GL017991.

Smyth, J.R., Frost, D.J., 2002. The effect of water on the 410-km discontinuity: an experimental study. Geophys. Res. Lett.29, 123-1–123-4. http://doi.org/10.1029/2001GL014418.

Sun, M., Liu, K.H., Fu, X., Gao, S.S., 2017. Receiver function imaging of mantle transition zone discontinuities beneath the Tanzania craton and adjacent segments of the east African rift system. Geophys. Res. Lett.44, 12116–12124. http://doi.org/10.1002/2017GL075485.

Tauzin, B., Debayle, E., Wittlinger, G., 2008. The mantle transition zone as seen by global Pds phases: no clear evidence for a thin transition zone beneath hotspots. J. Geophys. Res., Solid Earth113, B08309. http://doi.org/10.1029/2007JB005364.

Tauzin, B., Debayle, E., Wittlinger, G., 2010. Seismic evidence for a global low-velocity layer within the Earth's upper mantle. Nat. Geosci.3, 718–721. http://doi.org/10.1038/ngeo969.

Tauzin, B., Ricard, Y., 2014. Seismically deduced thermodynamics phase diagrams for the mantle transition zone. Earth Planet. Sci. Lett.401, 337–346. http://doi.org/10.1016/j.epsl.2014 .05 .039.

Thompson, D.A., Helffrich, G., Bastow, I.D., Kendall, J.M., Wookey, J., Eaton, D.W., 2011. Implications of a simple mantle transition zone beneath cratonic North America. Earth Planet. Sci. Lett.312, 28–36. https://doi.org/10.1016/j.epsl.2011.09.037.

Van der Meijde, M., Marone, F., Giardini, D., Van der Lee, S., 2003. Seismic evidence for water deep in Earth's upper mantle. Science300, 1556–1558. http://doi.org/10.1126/science .1083636.

Wittlinger, G., Farra, V., 2007. Converted waves reveal a thick and layered tecto-sphere beneath the Kalahari super-craton. Earth Planet. Sci. Lett.254, 404–415. http://doi.org/10.1016 /j.epsl.2006.11.048.

Wood, B., Pawley, A., Frost, D., 1996. Water and carbon in the Eartha's mantle. Phi-los. Trans. R. Soc., Math. Phys. Eng. Sci.354, 1495–1551. http://doi.org/10.1098/rsta.1996.0060.

Youssof, M., Thybo, H., Artemieva, I., Levander, A., 2015. Upper mantle structure beneath southern African cratons from seismic finite-frequency P-and S-body wave tomography. Earth Planet. Sci. Lett.420, 174–186. http://doi.org/10.1016/j.epsl.2015.01.034.

Yu, Y., Liu, K.H., Moidaki, M., Reed, C.A., Gao, S.S., 2015. No thermal anomalies in the mantle transition zone beneath an incipient continental rift: evidence from the first receiver function study across the Okavango Rift Zone, Botswana. Geophys. J. Int.202, 1407–1418. http://doi.org/10.1093/gji/ggv229.

# III. MANTLE TRANSITION ZONE STRUCTURE BENEATH NORTHEAST ASIA: EVIDENCE FROM RECEIVER FUNCTIONS

## ABSTRACT

The 410 and 660 km discontinuities (d410 and d660), which represent the top and bottom boundaries of the mantle transition zone (MTZ), beneath northeast Asia are imaged in successive circular bins with a radius of 1 degree by stacking a total of 274,593 P-to-S radial receiver functions recorded by 799 broadband seismic stations. After moveout correction based on the 1-D IASP91 Earth model, the resulting apparent depths of the discontinuities exhibit significant and spatially systematic variations. From east to west in the study area, three approximately N-S elongated narrow zones with significantly thickened MTZ are observed, which may be associated with the thermal and hydrous effects of subducted Pacific slabs. The major volcanoes in northeast China are underlain by a d660 that is apparently depressed by 20 km. The thickened MTZ beneath the volcanoes can be interpreted by the presence of an anomalously high-water concentration in the lower MTZ released from the stagnated slab. Such a spatial correspondence between the volcanoes and MTZ thickening, when combined with results from seismic tomography studies, is consistent with the hypothesis that the volcanoes are fed by wet and hot upwelling originated from slab dehydration in the MTZ. Beneath the Baikal Rift zone, the thickened MTZ is consistent with a passive rifting mechanism. In contrast, an abnormally thin MTZ is observed beneath the Hangay Dome in central Mongolia mostly associated with an uplifted d660, suggesting the possible existence of thermal upwelling from lower mantle through the MTZ.

# 1. INTRODUCTION

Subduction of the Pacific Plate beneath the eastern margin of the Eurasian plate started from before Jurassic (Sun et al., 2007). Under the assumption that the subduction rate over the past ~150 million years is similar to the current rate of 90 mm/yr (Watson et al., 1987; Davis et al., 2004), a total of 13,500 km of Pacific lithosphere has been subducted. In the northeast China, the subducted Pacific slab has been identified by many seismic tomographic studies (Chen et al., 2017; Huang & Zhao, 2006; Li & Van Der Hilst, 2010; Tang et al., 2014) as a high-velocity zone of about 100 to 200 km wide in the upper mantle. In the mantel transition zone (MTZ), which is bordered by the 410 km (d410) and 660 km (d660) discontinuities, most seismic tomography studies (Fukao et al., 2001; Huang & Zhao, 2006; Li & Van Der Hilst, 2010) imaged the stagnant slab as a sub-horizontal layer of high velocities with a thickness of about 100-200 km. The leading edge of the horizontally deflected slab in the MTZ may reach the eastern margin of Great Xing'an Range (Figure 1).

The intraplate Cenozoic volcanoes in northeast China are mainly distributed along the edges of the Songliao basin (Figure 1, Fan & Hooper, 1991; Liu et al., 2001). In spite of numerous studies aiming at understanding the origins of intraplate volcanoes such as those found in NE China (Turcotte and Shcubert, 1982; Tang et al., 2014; Wei et al., 2018), the physical and chemical processes responsible for these volcanoes remain enigmatic. Turcotte and Shcubert (1982) suggest that the Changbaishan volcanoes (Figure 1) might be associated with a hotspot, while some recent tomographic studies (Wei et al., 2018; Zhao et al., 2009) attribute the Changbaishan volcanoes to wet and hot

upwelling from dehydration of the subducting Pacific slab. Some other studies (e.g., Tang et al., 2014) interpret the Changbaishan volcanoes as the consequence of the decompression melting from subduction-induced upwelling through a slab gap.

Besides the Changbaishan, the origin of other Cenozoic volcanoes in NE China such as the Wudalianchi and Halaha volcanoes also remains controversial. Geochemical investigations (Kuritani et al., 2013) suggest that the Wudalianchi volcano is associated with a hydrous mantle plume originating from the hydrated MTZ, while others (e.g., Zhang et al., 1998) attribute it to shallower processes. Recent seismic tomography studies (Wei et al., 2018) reveal that the widespread high velocity anomalies in the MTZ beneath the Wudalianchi and Halaha volcanoes and most other areas in NE China are underlain by low velocities in the shallow mantle. Wei et al. (2018) propose that the Wudalianchi volcano is fed by a wet upwelling from the stagnant Pacific slab in the MTZ, while the Halaha volcano, which is located above the leading edge of the Pacific slab, is associated with a focused upwelling caused by the sinking of the stagnant Pacific slab into the lower mantle.

The Baikal rift zone (BRZ), which is located between the Siberian platform and the Altai-Sayan fold belt (Figure 1), is characterized by high heat flow (Lysak, 1984), lower than normal mantle velocity (Zhao & Lei, 2006), crustal thinning (Gao et al., 2004), and negative gravity anomalies (Zorin et al., 1989). Although most tomographic studies (e.g., Gao et al., 2003; Petit et al., 1998; Zhao et al., 2006) found low velocity anomalies beneath the BRZ and adjacent areas, the depth extent of this low velocity anomaly remain highly divergent in different studies. Some studies support an active rifting, which is caused by an actively thermal upwelling (Zhao et al., 2006; Zorin et al.,

2003), while others favor a passive origin, which is induced by the driving forces from the collision between the Indian Plate and Eruaisa Plate (Achauer, 2002; Ai, 2000; Zoenshain & Savostin, 1981).

Another controversial issue in the study area is the cause of the anomalously high topography of the Hangay Dome in central Mongolia (Figure 1). Some studies suggest that lithospheric thinning beneath the Hangay Dome is the result of thermal upwelling from the lower mantle impinged on the bottom of the lithosphere (Chen et al., 2015; Zhang et al., 2017; Zorin et al., 2003), probably associated with a mantle plume. However, other studies (Friederich, 2003; Mordvinova et al., 2015) consider that lithospheric delamination induced convective asthenospheric upwelling is responsible for the anomalously elevated topography.

While seismic tomography studies have provided valuable constraints on the spatial distribution of the subducted slabs and mantle upwellings, considerable discrepancies on the lateral and especially vertical extents of the structures remain, leading to significantly different endmember models regarding important questions such as formation of intraplate Cenozoic volcanoes in NE China, mechanisms responsible for the formation of the Hangay Dome, as well as the formation and evolution of the Baikal Rift. The opposite effects of hydration and low temperature that may co-exist in subducted slabs on seismic velocities may also play a role in the ambiguities in the interpretation of the seismic images.

Numerous mineral physical, geodynamic modeling, and geophysical observational investigations have demonstrated that in-situ temperature and presence of water in the MTZ can be revealed by the topography of the d410 and d660, which

represent the phase transition from olivine to spinel, and from ringwoodite to Mg-perovskite + magnesiowustite, respectively (Ringwood, 1975). The former transition has a positive Clapeyron slope, suggesting that a region of cold temperature results in an uplift of the d410 and vice versa, while the latter has a negative Clapeyron slope. The actual magnitude of the Clapeyron slopes, especially which associated with the d660, is debated (Bina & Helffrish, 1994; Fei et al., 2004; Ghosh et al., 2013). Recent studies suggest that water has similar effect on the topography of the MTZ discontinuities as low temperature, but the existence of water in the lower MTZ has a much more significant impact on the depression of the d660 than low temperature (Ghosh et al., 2013). Consequently, significant depressions of the d660 are indicative of the existence of a hydrous lower MTZ (Ghosh et al., 2013; Cao & Levander, 2010; Mohamed et al., 2014).

A number of MTZ studies have been conducted in various regions of northeast Asia to investigate the thermal state and the presence of water in the MTZ. Ai et al. (2003) and Li and Yuan (2003) image the MTZ structure beneath northeast China using similar broadband stations. Both studies show a regionally depressed d660 and thickened MTZ, suggesting that the Pacific slab exists in the MTZ and has reached the lower mantle. Another MTZ study (Liu et al. ,2015) measures the depth variation of the MTZ discontinuities beneath northeast China based on different velocity models, and find a thinned MTZ beneath the Changbaishan volcanoes, indicating the absence of cold slabs in the MTZ and that the volcanoes might be fed by thermal upwelling from lower mantle rather than slab dehydration. In contrast, Tian et al (2017) reveal a thicker than normal MTZ thickness beneath the Changbaishan volcanoes and attribute their formation to dehydration of the subducting Pacific slab in the MTZ. Beneath the BRZ, Liu & Gao

(2003) reveal an uplifted d410, depressed d660 and a thicker than normal MTZ which favor a passive rifting mechanism. Si et al. (2013) utilize receiver functions from two stations (TLY and ULN) to image the MTZ discontinuities beneath BRZ, and find depressed MTZ discontinuities and an about 40 km thickening beneath the BRZ except for a small area with limited MTZ thinning (20 km). They indicated that the development of the BRZ is dominant by the detachment of the lithosphere and the consequent hot upwelling. Using seismic data from 3 stations, Chen et al. (2015) report an MTZ that is 10-20 km thinner than the globally averaged value of 250 km beneath Hangay Dome, and interpret it as the consequence of a slightly warmer thermal anomaly across the MTZ.

Following a receiver function (RF) stacking procedure (Gao & Liu, 2014) developed under the assumption of non-plane wave front, which is capable of more accurately imaging the d410 and d660 than procedures assuming a plane wave front, this study utilizes an unprecedentedly large number (274,593) of P-to-S receiver functions from the d410 and d660 to produce robust images of the MTZ discontinuities beneath northeast Asia, for the purpose of providing additional constraints on a number of significant issues related to slab subduction and thermal upper welling.

## 2. DATA AND METHOD

### 2.1. DATA

The broadband teleseismic data employed in the study were recorded by 799 stations in the study area (97°E to 142°E, and 37°N to 52°N) from a total of 35 different networks (Figure 1). Among the stations, 189 provided publicly-available data through

the IRIS Data Management Center, and the remaining 610 stations were part of the seismic networks managed by various Chinese agencies. The recording duration for the stations is from mid-1986 to September-2018. To achieve an optimal balance between the quality and quantity of the requested data, a variable cut-off magnitude (Mc) is calculated based on the empirical equation, Mc=5.2+(delta–30.0)/(180.0–30.0)–D/700.0, where delta and D represent the epicentral distance (ranging from 30° to 100°) in degree and focal depth in kilometer, respectively (Liu & Gao, 2010).

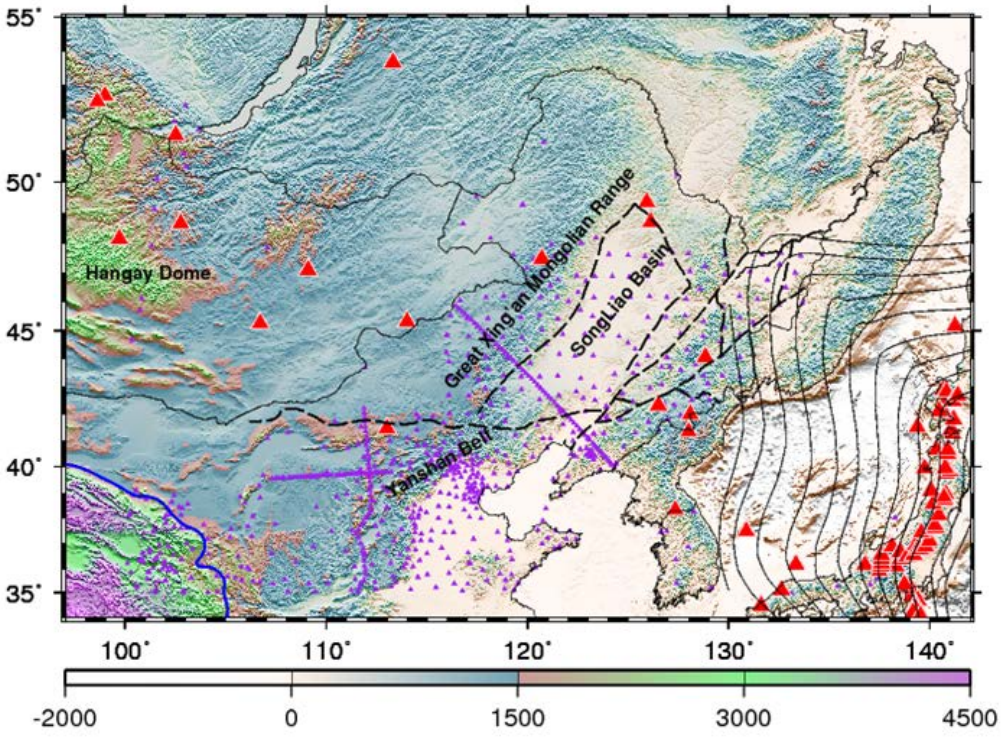


Figure 1 Topographic relief map of northeast Asia showing distribution of Cenozoic volcanoes (red triangles), seismic stations (purple triangles), major tectonic provinces, and depth contours of the subducting Pacific slab

## 2.2. DATA PROCESSING

Detailed description of the procedure for data selection, pre-processing, moveout correction, as well as stacking under a non-plane-wave assumption can be found in the study for the contiguous United States (Gao & Liu, 2014), and is briefly described below. A band-pass filter (0.02-0.2 Hz) was applied to filter the requested seismograms. The signal-to-noise ratio (SNR) of the vertical-component seismograms with a first arrival of the compressional wave were calculated using the method of Gao & Liu (2014). Following the procedure of Ammon (1991), we used all the filtered 3-component seismograms with an SNR exceeds 4.0, to generate the radial RFs. Then visually checking are processed for all the RFs to reject the ones with abnormal arrivals or no clear first P pulse. Finally, a total of 274,593 RFs from 10,129 events were used, a quantity that is unprecedented for any P-to-S receiver function studies in the area.

The coordinates of the ray-piercing points at the depth of 535 km (which is approximately the center of the MTZ) are first calculated, and the RFs with piercing points in each of the radius=1° circular bins are moveout corrected and stacked to form a depth series using the IASP91 earth model. The distance between neighboring bins is 1° and therefore, there is an overlap among neighboring bins. To ensure reliability, results from bins with less than 10 RFs are not used. For each bin, a bootstrap resampling procedure with 50 resampling iterations (Efron and Tibshirani, 1986) was employed to calculate the mean and standard deviation of the MTZ discontinuity depths and MTZ thickness.

Since the RFs were moveout-corrected utilizing the 1-D IASP91 standard Earth model, the resulting MTZ discontinuity depths are apparent rather than true depths. The

true depths can be obtained when accurate P- and S- wave speed anomalies are available for the crust, upper mantle and MTZ. In this study, following the velocity-correction procedure of Gao and Liu (2014), we used one regional (Chen et al., 2017) and two global wave speed models (Schaeffer and Lebedev, 2013; Burdick et al., 2016) to correct the apparent depths.

## 3. RESULTS

A total of 620 bins render robust determinations (Figure 2), including 619 bins for d410, 615 bins for d660, and 614 bins for both. As a result of the high quality and quantity of the RFs, the d410 and d660 arrivals are unambiguously identified for virtually all the bins, except for a few of them on the edges of the study area. All the depth series are plotted along 21 E-W profiles in Figure S1. The resulting d410 depths range from 379 to 444 km with a mean value of 415.7±8.15 km, and for the d660, the corresponding values are 634, 704 and 669.4±10.3 km, respectively. The observed MTZ thickness ranges from 209 to 297 km, with a mean value of 253.1±10.0 km, which is 3 km thicker than the global average of 250 km in the IASP91 Earth model. A continuous curvature surface gridding algorithm with a tension factor of 0.5 (Smith & Wessel, 1990) was used to obtain the spatially continuous images of the discontinuity depths and MTZ thickness (Figure 3). According to the patterns of the resulting discontinuity depths and MTZ thickness, we selected 7 most interesting subareas for discussion (Figure 3), and the averaged measurements for each of the subareas are shown in Table 1.

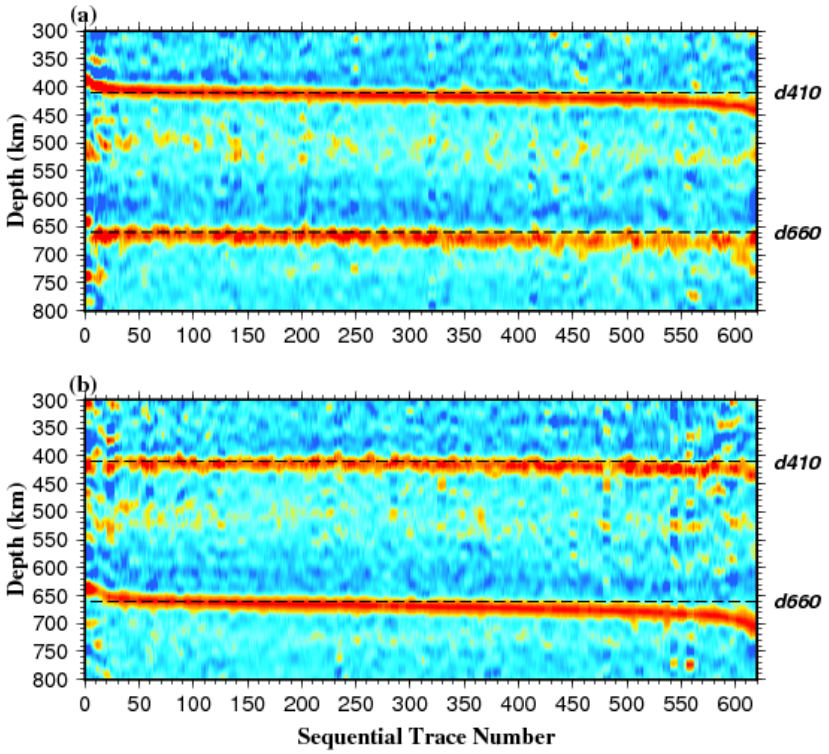


Figure 2 (a) Depth series in 1° radius bins plotted with respect to the sequentially increasing depth of the d410. (b) Same as Figure 2a but for sequentially increasing depth of the d660

Table 1 Averaged measurements for each of the subareas

| Area | d410 (km) | d410_SD (km) | d660 (km) | d660_SD (km) | MTZ (km) | MTZ_SD (km) |
|---|---|---|---|---|---|---|
| Study area | 416 | 8 | 669 | 10 | 253 | 10 |
| A | 393 | 12 | 671 | 5 | 277 | 17 |
| B | 425 | 8 | 667 | 8 | 241 | 7 |
| C | 417 | 11 | 680 | 12 | 262 | 7 |
| D | 414 | 5 | 665 | 6 | 250 | 6 |
| E | 415 | 5 | 674 | 6 | 259 | 6 |
| F | 417 | 10 | 672 | 11 | 255 | 4 |
| G | 420 | 6 | 648 | 11 | 228 | 9 |

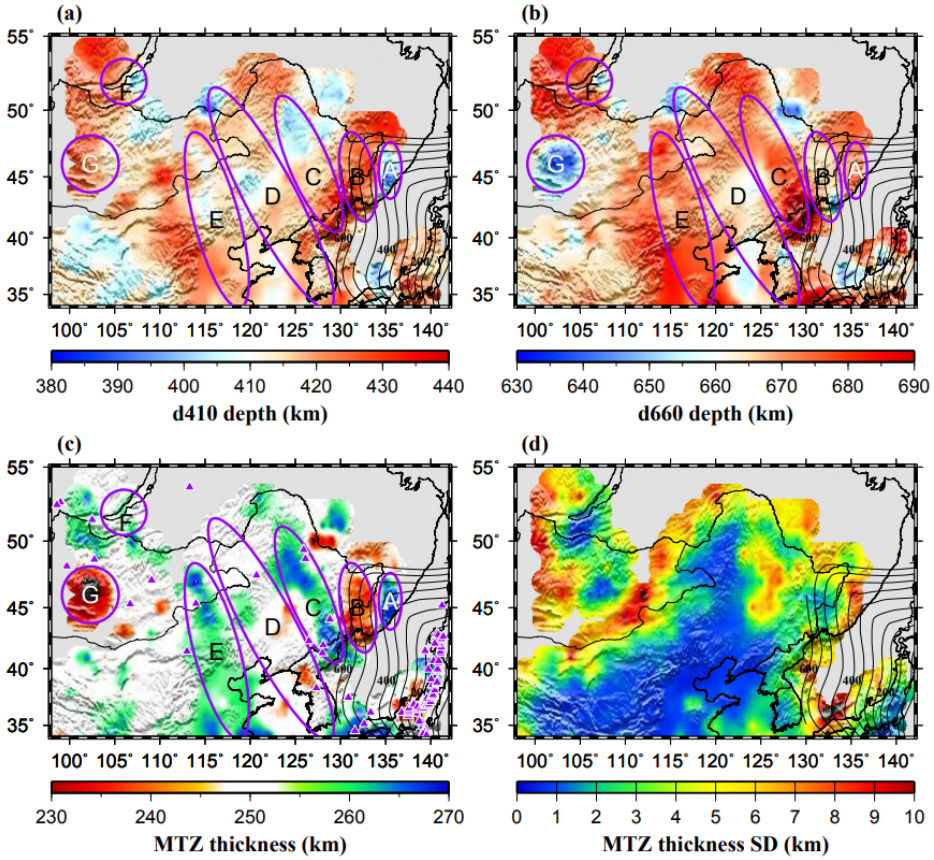


Figure 3 (a) Spatial distribution of resulting d410 depths. (b) Same as (a) but for the d660. (c) MTZ thickness measurements. (d) Standard deviation (SD) of the MTZ thickness measurements

Since velocity anomalies in the upper mantle would increase, while thermal, velocity or water content anomalies in the MTZ would decrease, the cross-correlation coefficient (XCC) between the apparent d410 and d660 depths (Gao & Liu, 2014), the XCC can reflect the effectivity of the velocity correction. The original XCC between the apparent MTZ discontinuities is 0.43 (Figure 4), which is significantly lower than 0.84 for the contiguous United States (Gao & Liu, 2014) and 0.7 for the southern Africa (Sun et al., 2018), indicating the presence of significant thermal, water content or velocity

anomalies in the MTZ. Three velocity models (Chen et al., 2017; Schaeffer & Lebedev, 2013; Burdick et al., 2016) are employed for velocity correction in this study, and the corrected MTZ thickness are shown in Figure 5. The considerable differences in the corrected depths (Figure 5) are indicative of the discrepancies of the velocity models. Since it is impossible to determine which corrected result is the most realistic one, in the following we discuss the thermal, water, and velocity structure mostly based on the apparent depths rather than true depths.

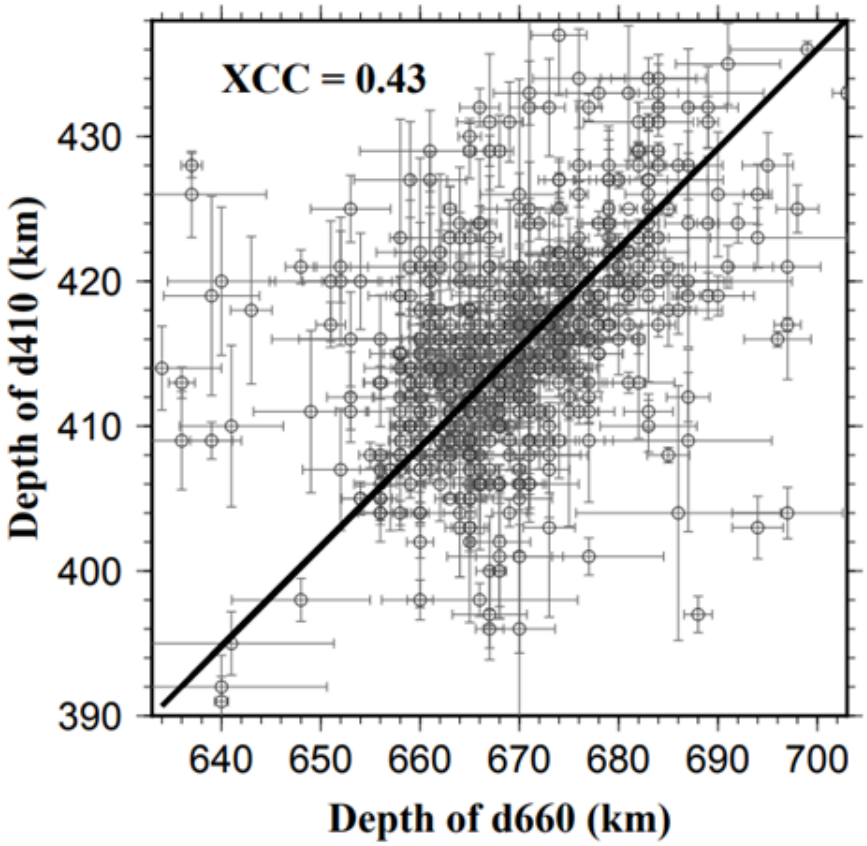


Figure 4 Correlation plot of apparent d410 and d660 depths. The line indicates the optimal bivariate regression with a cross-correlation coefficient of 0.43

# 4. DISCUSSION

## 4.1. IMPLICATIONS FOR THE DEPTH AND LATERAL EXTENTS OF THE SUBDUCTED PACIFIC SLAB BENEATH SORTHEAST ASIA

The resulted systematic spatial variations of the MTZ thickness and apparent discontinuity depths can provide valuable constraints on the geometry and depth extent of the subducted Pacific slab in northeast China. Similar to most previous MTZ studies (Ai et al., 2003; Chen et al., 2013; Tang et al., 2014), a widespread depression of the d660 with magnitude of about 14 km is observed beneath Areas A-C (Figure 3).

Beneath Area A, an ~17 km apparent uplift of the d410 is observed around the depth contour of 400 km of the subducting Pacific slab defined by deep earthquakes and higher-than-normal P wave velocity anomalies (Figure 6) (Chen et al., 2017). The uplifted d410 may be caused by the low temperature associated with the subducted slab due to the positive Claypeyron slope of +2.9 MPa/K (Bina & Helffrish, 1994), which means that the slab segment has possibly penetrated into the MTZ beneath Area A.

In Area B, our results show that the d410 and d660 are apparently depressed by about 15 km and 7 km, respectively, leading to an 8 km thinning of the MTZ on average. The simplest model that can account for the observations in Region B involves a low velocity zone (LVZ) in the upper mantle and a high velocity anomaly in the MTZ associated with the subducting slab. If we assume a $d\ln(V_s)/d\ln(V_p)$ value of 2.0 (Gao & Liu 2014), a low velocity zone with a mean $V_p$ anomaly of about -1.1% in the upper mantle would result in an apparent depression of 15 km for both the d410 and d660, while a high velocity anomaly of about +0.9% in the MTZ from the subducting slab

would uplift the d660 about 7 km, which are similar to the observed in this region. The required velocities anomalies for the upper mantle and MTZ to produce the observed undulations of the discontinuities are in general agreement with those from most previous seismic tomographic studies (Figure 6; Zhao et al., 2009; Chen et al., 2017; Wei et al., 2018).

The largest depression of the d660 (20 km) and significant MTZ thickening (12 km) occur west of the 600 km depth contour line of the subducting Pacific slab (Area C), implying that the subducted slab contacts closely with the d660 in Area C (Figures 3, 6). Previous tomographic studies show that the stagnant Pacific slab in the MTZ reaches the Great Xing'an Range (Huang & Zhao, 2006; Li & Van der Hilst, 2010; Obayashi et al., 2013; Wei et al., 2012). However, the normal MTZ thickness observed in Area D suggests the absence of a cold slab in the MTZ beneath this area. In contrast, the thickened MTZ in region C (Figure 3) reveals that only the northern portion of the leading edge of the subducted Pacific slab in the MTZ has reached the eastern margin of the Great Xing'an Range, while the central and southern portions merely reached the eastern edge of the Songliao basin (Figure 3).

## 4.2. FORMATION MECHANISM OF CENOZOIC VOLCANOES IN NORTHEAST CHINA

The intraplate Cenozoic volcanoes in northeast China, including the Changbaishan, Jingpohu, Longgang, Wudalianchi, Halaha, are mainly distributed in Area C which is characterized by an MTZ that is on average 13 km thicker than normal (Figure 3). The MTZ thickening is due to a 7-km apparent depression of the d410 and a 20 km

depression of the d660 (Figure 3). In the following we use a model involving velocity, thermal, and water content anomalies in the upper mantle and MTZ to quantitatively discuss the observations in this area.

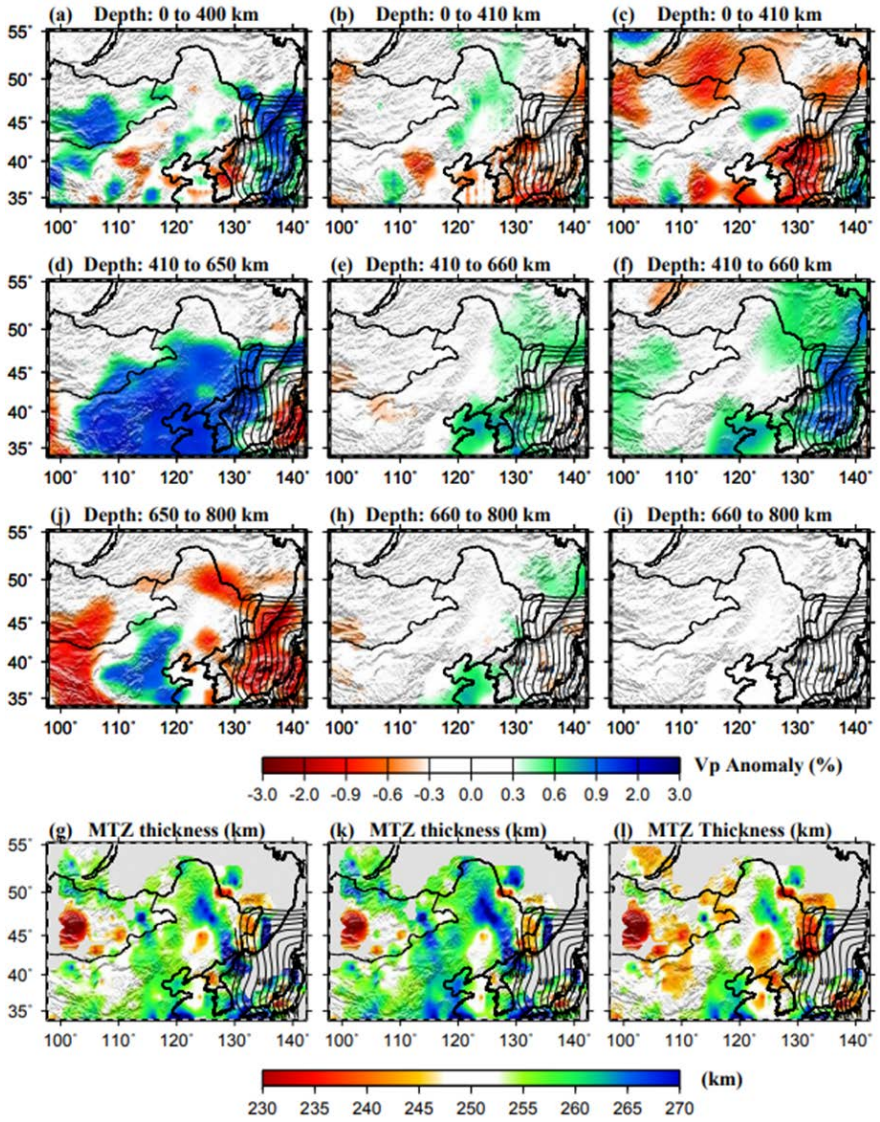


Figure 5 Averaged upper mantle (first row), MTZ (second row), topmost lower mantle (third row) P-wave velocity anomalies, and corrected MTZ thickness (fourth row) by the previous studies (Chen et al., 2017; Schaeffer & Lebedev, 2013; Burdick et al., 2016)

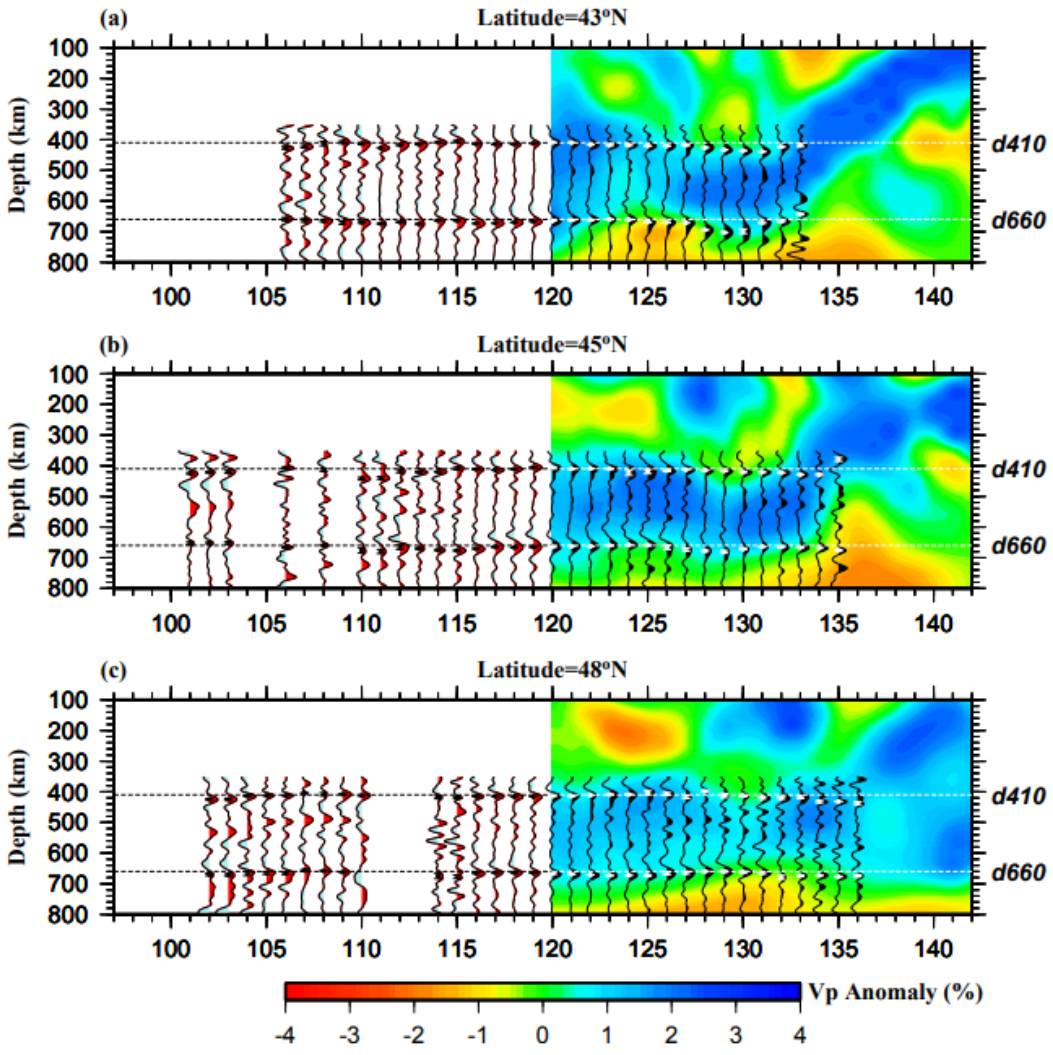


Figure 6 Stacked receiver functions across 3 latitudinal lines. The background image shows P-wave velocity anomalies (Chen et al., 2017)

In this model, if we assume a $d\ln(V_s)/d\ln(V_p)$ value of 2.0 (Gao & Liu 2014), a mean $V_p$ anomaly of -0.5 percent in the upper mantle would lead to an ~7 km apparent depression of both the d410 and d660. In contrast, the high velocities of the slab in the MTZ can lead to an ~7 km apparent uplift of the d660. Additionally, if the scaling

relationship of $dV_p/dT = -4.8\times10^{-4}$ km×$s^{-1}K^{-1}$ (Deal et al., 1999) is used, the +1.6% velocity anomaly associated with the stagnant slab corresponds to a -330 K thermal anomaly, which would result in an additional depression of the d660 by about 12 km if a Claypeyron slope of -1.3 MPa/K (Fei et al., 2004) is used. The net 12 km depression of the d660 is significantly smaller than the 20 km depression observed in this study, implying that the observed depression of the d660 in this area cannot be explained solely by the negative temperature (and corresponding velocity) anomaly related to the stagnant slab in the lower MTZ.

Mineral physics experiments predict that cold and old (≥ 50 Myr) slabs have the capability of carrying water into the MTZ, by hydrous minerals and dense hydrous magnesium silicates (Thompson 1992; Pearson et al., 2014). Water solubility of wadsleyite and ringwoodite in the slabs reduces with increased temperature (Ohtani et al., 2000, 2004), and thus facilitates gradual and long-lasting slab dehydration. Many studies reveal that a high-water content exists in the MTZ beneath some areas above the stagnant slabs in northeast China (Kelbert et al., 2009; Wang et al., 2015), which is considered as the result of the deep dehydration from the stagnant slab. Litasov et al. (2005) indicate that at 1473 K temperature condition, 2 wt. % of water in hydrous peridotite can lead to 15 km depression of the d660. If this is the case, the remaining 8 km depression of the d660 observed in Area C can be attributed to a 1.0 wt. % water content in the lower MTZ, which is close to the 0.8 wt. % value estimated by Wei et al. (2015) based on seismic tomography. The existence of high water concentration in the MTZ and the long-term (~150 million years) subduction history of the Pacific plate are consistent with the hypothesis that the volcanoes in this area may be related to wet upwelling originated from

dehydration of the subddcted Pacific slab, a mechanism that has been proposed to explain the loss of cratonic root beneath North China (Zhu et al., 2012) and the formation of Cenozoic volcanoes and continental floods basalts in northeast China (Chen et al., 2017, Tian et al., 2016; Wei et al., 2018).

### 4.3. SMALL-SCALE THERMAL UPWELLING ADJACENT TO THE CURRENT PACIFIC SLAB IN THE MTZ

Beneath the region D, an about 5 km depression for both the d410 (414±5 km) and d660 (665±6 km) and a close-to-normal MTZ thickness (251±6 km) are observed (Figure 3). The small scaled anomalously thin MTZ observed beneath the center of the Songliao basin and North Korea have estimated averaged thickness of 241 and 240 km, corresponding to an estimated positive thermal anomaly of +76K and +85K, respectively. Numerical models tested by Feccenna et al. (2010) show that the lateral edge of subducting slab can cause a mantle thermal upwelling originating from beneath the slab. This atypical thermal upwelling is revealed by previous MTZ studies in Indochina Peninsula (Yu et al., 2017) and Alaska (Dahm et al., 2017). Therefore, we speculate that the thermal upwelling beneath center of Songliao basin and North Korea might be originated beneath the subducting Pacific slab.

Additionally, an S-wave receiver function study conducted by Zhang et al. (2014) suggests a thinned lithosphere of about 100-120 km in thickness beneath the Songliao basin, which is about 40 km thinner than that beneath the Great Xiangan Range. Previous studies (Zhang et al., 2010; Wei et al., 2018) suggest that this lithospheric thinning might be caused by lithospheric delamination occurred in the Cretaceous. The anticipated

negative temperature anomaly in the sinking lithospheric layer, if it has reached the MTZ, is expected to result in a thicker than normal MTZ. The normal and slightly thinner than normal MTZ in Area D indicates that the lithospheric delamination beneath the Songliao basin, if exists, has no observable influence on the MTZ temperature, implying that the delaminated lithosphere has not reached the MTZ.

## 4.4. EVIDENCE FOR THE EXISTENCE OF SUBDUCTED ANCIENT PACIFIC SLAB IN THE MTZ

In Area E, the MTZ is about 9 km thicker than normal on average, which is caused by a 5 km apparent depression of the d410 and 14 km apparent depression of the d660 (Figure 3). Previous studies (e.g., Fukao et al., 2001) suggest that Area E is underlain by an ancient Pacific slab. Considering similar values of both MTZ discontinuity depths and MTZ thickness between regions C and E, we conclude that the MTZ thickening in the region E is possibly caused by ancient Pacific slab.

## 4.5. RIFTING MECHANISM OF BAIKAL RIFT

The BRZ (Region F) is characterized by depressed d410 and d610 that are 7 and 12 km deeper than normal, respectively, and a slightly thickened MTZ with magnitude of 5 km (Figure 3). Both the weakly depressed MTZ discontinuities observed in this study indicate that a low velocity anomaly exists in the upper mantle, which is consistent with previous tomographic studies (Gao et al., 2003; Zhao et al., 2006). Similar to more localized studies (Liu and Gao, 2003; Si et al., 2013), the observed slightly thickened MTZ suggests the absence of a thermal upwelling perturbing the MTZ directly beneath

the BRZ, which favors a passive rifting mechanism for the BRZ (Achauer, 2002; Ai, 2000; Zoenshain & Savostin, 1981). The observations of the BRZ are consistent with those beneath some other continental rifts with different maturity such as the Okavango rift (Yu et al., 2015), Malawi and Luangwa rifts (Reed et al, 2016) and western branch of the East Africa rift system (Sun et al., 2017).

## 4.6. THERMAL UPWELLING BENEATH THE HAGAY DOME AND ALTAI MOUNTAIN

The most prominent feature in central Mongolia is an on average 22±9 km thinning of the MTZ beneath the Hangay Dome and Altai Mountain in an approximately circular region of about 400 km in diameter. This thinning is centered at the Hangay Dome and is associated with a 10 km apparent depression of the d410 and a 12 km uplift of the d660 (Figure 3).

A recent receiver function study (Chen et al., 2015) has also detected a 10-20 km thinner-than-normal MTZ beneath the Hangay Dome, and interpreted it as the consequence of a slightly warmer thermal anomaly across the MTZ. However, although both studies have found similar magnitude of MTZ thinning beneath the Hangay Dome, there is a significant discrepancy in the distribution of the observed thinned MTZ. In this study, the thinning of the MTZ primarily occurs between 100°E and 105°E, while that revealed in Chen et al. (2015) mainly exists between 104°E and 110°E. The discrepancy in this area is most likely caused by that only 3 stations were used in Chen et al. (2015), while 12 stations were utilized in this study.

One of the simplest mechanisms for the thinner-than-normal MTZ in this area is that thermal anomalies beneath Hangay Dome traverses the whole MTZ from the lower mantle. Assuming Clapeyron slopes of +2.9 MPa/K and -1.3 MPa/K for the d410 and d660 (Bina & Helffrich, 1994; Fei et al., 2004), respectively, the observed 22 km thinning of the MTZ corresponds to a 185K temperature increase in the MTZ.

The presence of thermal anomaly from the lower mantle beneath the Hangay Dome is also evidenced by various studies using different techniques. The integrated seismic study (Chen et al., 2015) find a thinner-than-normal MTZ and low velocity anomalies through the entire MTZ beneath the Hangay Dome, and interprets it as the consequence of a thermal upwelling across the MTZ. A tomographic study (Zhang et al., 2017) focused on the central Mongolia also reveals a low velocity zone beneath Hangay Dome, which is rooted at least 800 km, suggesting that the deep thermal upwelling may cause the uplift of the Hangay Dome and magmatism of the active Khanuy Gol and Middle Gobi volcanoes. Using regional gravity data, Zorin et al. (2003) construct 3-dimensional gravity models and reveal the existence of deep thermal upwelling beneath Mongolia, including the Hangay Dome and the Hentay Mountains.

## 5. CONCLUSION

Using an unprecedented number of RFs recorded in northeast Asia, we imaged the topography of the d410 and d660 under the non-plane wave assumption. Beneath the study area, a low XCC between the apparent depths of the d410 and d660 is obtained, suggesting the presence of the thermal, water content or velocity anomalies in the MTZ.

The current and ancient Pacific slabs might be responsible for the three approximately N-S oriented zones with thickened MTZ. Most of the major Cenozoic volcanoes in Northeast China are underlain by a depressed d660 and thickened MTZ, which can be explained by hot and wet upwelling originated from dehydration of the subducted Pacific slab. The observed thickened MTZ beneath the BRZ is inconsistent with the present-day existence of active thermal upwelling from the lower mantle. In contrast, the presence of a thermal upwelling from lower mantle cross the MTZ is indicated by the observed abnormally thinned MTZ beneath the Hangay Dome.

# APPENDIX A. SUPPLEMENTARY MATERIAL

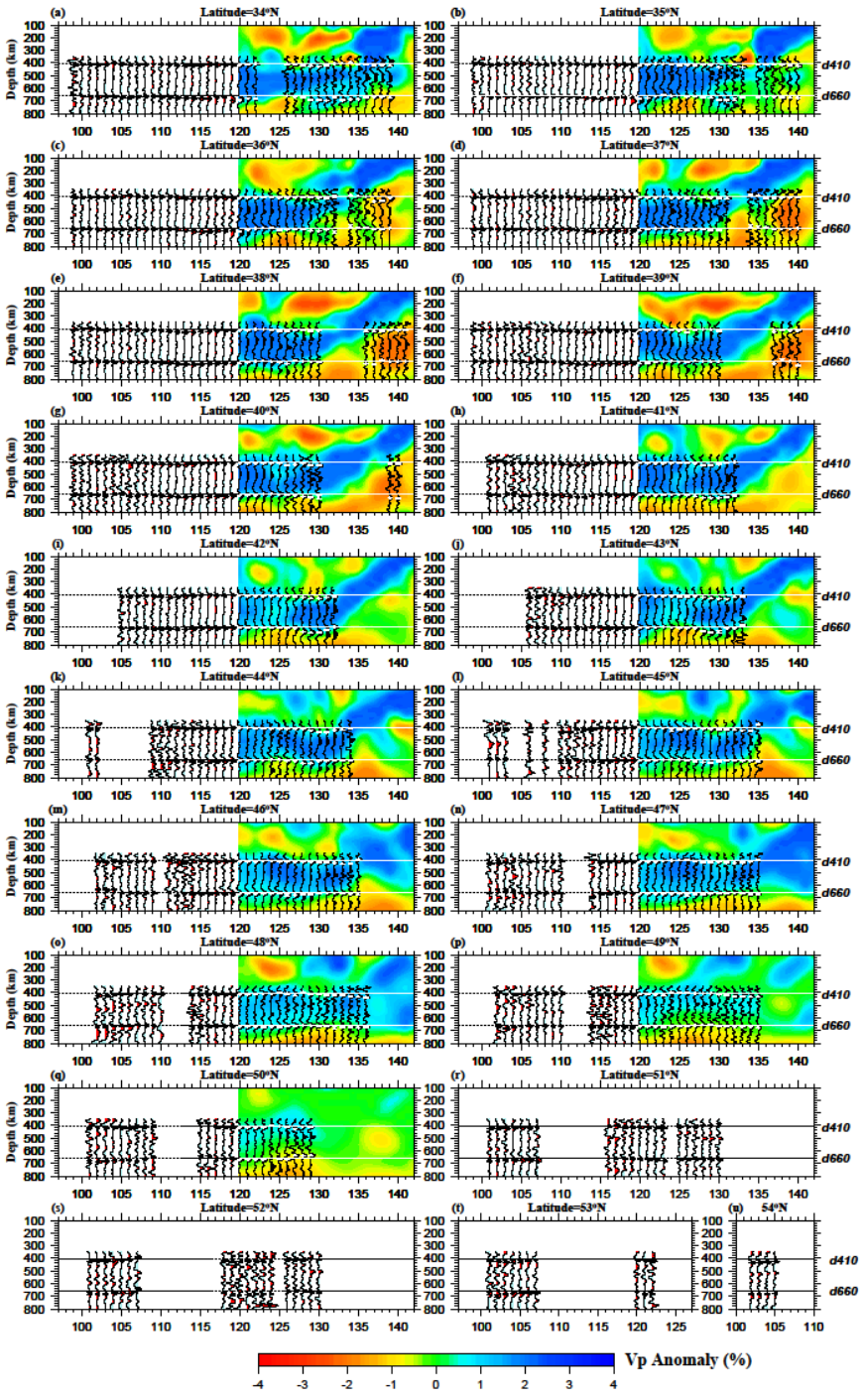


Figure S1 Stacked receiver functions across 21 latitudinal lines. The background image shows P-wave velocity anomalies (Chen et al., 2017)

## REFERENCES

Achauer, U., & Masson, F. (2002). Seismic tomography of continental rifts revisited: from relative to absolute heterogeneities. Tectonophysics, 358(1-4), 17-37.

Ai, Y., Zheng, T., Xu, W., He, Y., & Dong, D. (2003). A complex 660 km discontinuity beneath northeast China. Earth and Planetary Science Letters, 212(1-2), 63-71.

Ammon, Charles J. "The isolation of receiver effects from teleseismic P waveforms." Bulletin-Seismological Society of America 81.6 (1991): 2504-2510.

Bina, C. R., & Helffrich, G. (1994). Phase transition Clapeyron slopes and transition zone seismic discontinuity topography. Journal of Geophysical Research: Solid Earth, 99(B8), 15853-15860.

Burdick, S., Li, C., Martynov, V., Cox, T., Eakins, J., Mulder, T., ... & van der Hilst, R. D. (2008). Upper mantle heterogeneity beneath North America from travel time tomography with global and USArray transportable array data. Seismological Research Letters, 79(3), 384-392.

Cao, A., & Levander, A. (2010). High-resolution transition zone structures of the Gorda Slab beneath the western United States: Implication for deep water subduction. Journal of Geophysical Research: Solid Earth, 115(B7).

Chen, C., Zhao, D., Tian, Y., Wu, S., Hasegawa, A., Lei, J., ... & Kang, I. B. (2017). Mantle transition zone, stagnant slab and intraplate volcanism in Northeast Asia. Geophysical Journal International, 209(1), 68-85.

Chen, M., Niu, F., Liu, Q., & Tromp, J. (2015). Mantle-driven uplift of Hangai Dome: New seismic constraints from adjoint tomography. Geophysical Research Letters, 42(17), 6967-6974.

Davis, G., Xu, B., Zheng, Y. D., & Zhang, W. J. (2004). Indosinian extension in the Solonkersuture zone: The Sonid Zuoqi metamorphic core complex, Inner Mongolia, China. Dixue Qianyuan(Earth Science Frontiers), 11(3), 135-144.

Dahm, H. H., Gao, S. S., Kong, F., & Liu, K. H. (2017). Topography of the mantle transition zone discontinuities beneath alaska and its geodynamic implications: constraints from receiver function stacking. Journal of Geophysical Research: Solid Earth, 122(12).

Deal, M. M., Nolet, G., & van der Hilst, R. D. (1999). Slab temperature and thickness from seismic tomography: 1. Method and application to Tonga. Journal of Geophysical Research: Solid Earth, 104(B12), 28789-28802.

Efron, B., & Tibshirani, R. (1986). Bootstrap methods for standard errors, confidence intervals, and other measures of statistical accuracy. Statistical science, 54-75.

Faccenna, C., Becker, T. W., Lallemand, S., Lagabrielle, Y., Funiciello, F., & Piromallo, C. (2010). Subduction-triggered magmatic pulses: A new class of plumes?. Earth and Planetary Science Letters, 299(1-2), 54-68.

Fei, Y., Van Orman, J., Li, J., Van Westrenen, W., Sanloup, C., Minarik, W., ... & Funakoshi, K. I. (2004). Experimentally determined postspinel transformation boundary in Mg2SiO4 using MgO as an internal pressure standard and its geophysical implications. Journal of Geophysical Research: Solid Earth, 109(B2).

Foulger, G. R., Panza, G. F., Artemieva, I. M., Bastow, I. D., Cammarano, F., Evans, J. R., ... & Yanovskaya, T. B. (2013). Caveats on tomographic images. Terra Nova, 25(4), 259-281.

Friederich, W. (2003). The S-velocity structure of the East Asian mantle from inversion of shear and surface waveforms. Geophysical Journal International, 153(1), 88-102.

Fukao, Y., Widiyantoro, S., & Obayashi, M. (2001). Stagnant slabs in the upper and lower mantle transition region. Reviews of Geophysics, 39(3), 291-323.

Gao, S. S., Liu, K. H., & Chen, C. (2004). Significant crustal thinning beneath the Baikal rift zone: New constraints from receiver function analysis. Geophysical Research Letters, 31(20).

Gao, S. S., & Liu, K. H. (2014). Imaging mantle discontinuities using multiply-reflected P-to-S conversions. Earth and Planetary Science Letters, 402, 99-106.

Gao, S. S., & Liu, K. H. (2014). Mantle transition zone discontinuities beneath the contiguous United States. Journal of Geophysical Research: Solid Earth, 119(8), 6452-6468.

Ghosh, S., Ohtani, E., Litasov, K. D., Suzuki, A., Dobson, D., & Funakoshi, K. (2013). Effect of water in depleted mantle on post-spinel transition and implication for 660 km seismic discontinuity. Earth and Planetary Science Letters, 371, 103-111.

Huang, J., & Zhao, D. (2006). High-resolution mantle tomography of China and surrounding regions. Journal of Geophysical Research: Solid Earth, 111(B9).

Kelbert, A., Schultz, A., & Egbert, G. (2009). Global electromagnetic induction constraints on transition-zone water content variations. Nature, 460(7258), 1003.

Khutorskoy, M. D., & Yarmoluk, V. V. (1989). Heat flow, structure and evolution of the lithosphere of Mongolia. Tectonophysics, 164(2-4), 315-322.

Kuritani, T., Ohtani, E., & Kimura, J. I. (2011). Intensive hydration of the mantle transition zone beneath China caused by ancient slab stagnation. Nature Geoscience, 4(10), 713.

Lei, J., & Zhao, D. (2005). P-wave tomography and origin of the Changbai intraplate volcano in Northeast Asia. Tectonophysics, 397(3-4), 281-295.

Li, C., & Van Der Hilst, R. D. (2010). Structure of the upper mantle and transition zone beneath Southeast Asia from traveltime tomography. Journal of Geophysical Research: Solid Earth, 115(B7).

Li, X., & Yuan, X. (2003). Receiver functions in northeast China–implications for slab penetration into the lower mantle in northwest Pacific subduction zone. Earth and Planetary Science Letters, 216(4), 679-691.

Liu, Z., Niu, F., Chen, Y. J., Grand, S., Kawakatsu, H., Ning, J., ... & Ni, J. (2015). Receiver function images of the mantle transition zone beneath NE China: New constraints on intraplate volcanism, deep subduction and their potential link. Earth and Planetary Science Letters, 412, 101-111.

Liu, K. H., & Gao, S. S. (2010). Spatial variations of crustal characteristics beneath the Hoggar swell, Algeria, revealed by systematic analyses of receiver functions from a single seismic station. Geochemistry, Geophysics, Geosystems, 11(8).

Liu, K. H., & Gao, S. S. (2006). Mantle transition zone discontinuities beneath the Baikal rift and adjacent areas. Journal of Geophysical Research: Solid Earth, 111(B11).

Litasov, K. D., Ohtani, E., Sano, A., Suzuki, A., & Funakoshi, K. (2005). Wet subduction versus cold subduction. Geophysical Research Letters, 32(13).

Lysak, S. V. (1984). Terrestrial heat flow in the south of East Siberia. Tectonophysics, 103(1-4), 205-215.

Mordvinova, V. V., Treussov, A. V., & Turutanov, E. K. (2015). Nature of the mantle plume under Hangai (Mongolia) based on seismic and gravimetric data. In Doklady Earth Sciences(Vol. 460, No. 1, p. 92). Springer Science & Business Media.

Mohamed, A. A., Gao, S. S., Elsheikh, A. A., Liu, K. H., Yu, Y., & Fat-Helbary, R. E. (2014). Seismic imaging of mantle transition zone discontinuities beneath the northern Red Sea and adjacent areas. Geophysical Journal International, 199(2), 648-657.

Obayashi, M., Yoshimitsu, J., Nolet, G., Fukao, Y., Shiobara, H., Sugioka, H., ... & Gao, Y. (2013). Finite frequency whole mantle P wave tomography: Improvement of subducted slab images. Geophysical Research Letters, 40(21), 5652-5657.

Ohtani, E., Litasov, K., Hosoya, T., Kubo, T., & Kondo, T. (2004). Water transport into the deep mantle and formation of a hydrous transition zone. Physics of the Earth and Planetary Interiors, 143, 255-269.

Ohtani, E., Mizobata, H., & Yurimoto, H. (2000). Stability of dense hydrous magnesium silicate phases in the systems Mg 2 SiO 4-H 2 O and MgSiO 3-H 2 O at pressures up to 27 GPa. Physics and Chemistry of Minerals, 27(8), 533-544.

Petit, C., Koulakov, I., & Deverchère, J. (1998). Velocity structure around the Baikal rift zone from teleseismic and local earthquake traveltimes and geodynamic implications. Tectonophysics, 296(1-2), 125-144.

Reed, C. A., Liu, K. H., Chindandali, P. R., Massingue, B., Mdala, H., Mutamina, D., ... & Gao, S. S. (2016). Passive rifting of thick lithosphere in the southern East African Rift: Evidence from mantle transition zone discontinuity topography. Journal of Geophysical Research: Solid Earth, 121(11), 8068-8079.

Ren, J., Tamaki, K., Li, S., & Junxia, Z. (2002). Late Mesozoic and Cenozoic rifting and its dynamic setting in Eastern China and adjacent areas. Tectonophysics, 344(3-4), 175-205.

Ringwood, A. E. (1975). Composition and Petrology of the Earth's Mantle. MacGraw-Hill, 618.

Ren, J., Tamaki, K., Li, S., & Junxia, Z. (2002). Late Mesozoic and Cenozoic rifting and its dynamic setting in Eastern China and adjacent areas. Tectonophysics, 344(3-4), 175-205.

Ringwood, A. E. (1975). Composition and Petrology of the Earth's Mantle. MacGraw-Hill, 618.

Schaeffer, A. J., & Lebedev, S. (2013). Global shear speed structure of the upper mantle and transition zone. Geophysical Journal International, 194(1), 417-449.

Si, S., Tian, X., Zhang, H., & Teng, J. (2013). Prevalent thickening and local thinning of the mantle transition zone beneath the Baikal rift zone and its dynamic implications. Science China Earth Sciences, 56(1), 31-42.

Smith, W. H. F., & Wessel, P. (1990). Gridding with continuous curvature splines in tension. Geophysics, 55(3), 293-305.

Sun, M., Fu, X., Liu, K. H., & Gao, S. S. (2018). Absence of thermal influence from the African Superswell and cratonic keels on the mantle transition zone beneath southern Africa: Evidence from receiver function imaging. Earth and Planetary Science Letters, 503, 108-117.

Sun, M., Liu, K. H., Fu, X., & Gao, S. S. (2017). Receiver function imaging of mantle transition zone discontinuities beneath the Tanzania craton and adjacent segments of the East African Rift system. Geophysical Research Letters, 44(24).

Sun, W., Ding, X., Hu, Y. H., & Li, X. H. (2007). The golden transformation of the Cretaceous plate subduction in the west Pacific. Earth and Planetary Science Letters, 262(3-4), 533-542.

Tang, Y., Obayashi, M., Niu, F., Grand, S. P., Chen, Y. J., Kawakatsu, H., ... & Ni, J. F. (2014). Changbaishan volcanism in northeast China linked to subduction-induced mantle upwelling. Nature Geoscience, 7(6), 470.

Tian, Y., Zhu, H., Zhao, D., Liu, C., Feng, X., Liu, T., & Ma, J. (2016). Mantle transition zone structure beneath the Changbai volcano: Insight into deep slab dehydration and hot upwelling near the 410 km discontinuity. Journal of Geophysical Research: Solid Earth, 121(8), 5794-5808.

Tseesuren, B. (2001). Geothermal resources in Mongolia and potential uses.

Turcotte, D., and G. Schubert (1982), Geodynamics Applications of Continuum Physics to Geological Problems, pp. 1–449, John Wiley, New York.

Wang, X. C., Wilde, S. A., Li, Q. L., & Yang, Y. N. (2015). Continental flood basalts derived from the hydrous mantle transition zone. Nature communications, 6, 7700.

Watson, M. P., Hayward, A. B., Parkinson, D. N., & Zhang, Z. M. (1987). Plate tectonic history, basin development and petroleum source rock deposition onshore China. Marine and Petroleum Geology, 4(3), 205-225.

Wei, W., Hammond, J. O., Zhao, D., Xu, J., Liu, Q., & Gu, Y. (2018). Seismic evidence for a mantle transition zone origin of the Wudalianchi and Halaha volcanoes in Northeast China. Geochemistry, Geophysics, Geosystems.

Wei, W., Xu, J., Zhao, D., & Shi, Y. (2012). East Asia mantle tomography: New insight into plate subduction and intraplate volcanism. Journal of Asian Earth Sciences, 60, 88-103.

Wu, F. Y., Lin, J. Q., Wilde, S. A., Zhang, X. O., & Yang, J. H. (2005). Nature and significance of the Early Cretaceous giant igneous event in eastern China. Earth and Planetary Science Letters, 233(1-2), 103-119.

Yin, A. (2000). Mode of Cenozoic east-west extension in Tibet suggesting a common origin of rifts in Asia during the Indo-Asian collision. Journal of Geophysical Research: Solid Earth, 105(B9), 21745-21759.

Yu, Y., Gao, S. S., Liu, K. H., Yang, T., Xue, M., & Le, K. P. (2017). Mantle transition zone discontinuities beneath the Indochina Peninsula: Implications for slab subduction and mantle upwelling. Geophysical Research Letters, 44(14), 7159-7167.

Yu, Y., Liu, K. H., Moidaki, M., Reed, C. A., & Gao, S. S. (2015). No thermal anomalies in the mantle transition zone beneath an incipient continental rift: Evidence from the first receiver function study across the Okavango Rift Zone, Botswana. Geophysical Journal International, 202(2), 1407-1418.

Zhang, M., Zhou, X. H., & Zhang, J. B. (1998). Nature of the lithospheric mantle beneath NE China: evidence from potassic volcanic rocks and mantle xenoliths. Mantle Dynamics and Plate Interactions in East Asia, 27, 197-219.

Zhang, F., Wu, Q., Grand, S. P., Li, Y., Gao, M., Demberel, S., ... & Sukhbaatar, U. (2017). Seismic velocity variations beneath central Mongolia: Evidence for upper mantle plumes?. Earth and Planetary Science Letters, 459, 406-416.

Zhang, R., Wu, Q., Sun, L., He, J., & Gao, Z. (2014). Crustal and lithospheric structure of Northeast China from S-wave receiver functions. Earth and Planetary Science Letters, 401, 196-205.

Zhao, D., Tian, Y., Lei, J., Liu, L., & Zheng, S. (2009). Seismic image and origin of the Changbai intraplate volcano in East Asia: role of big mantle wedge above the stagnant Pacific slab. Physics of the Earth and Planetary Interiors, 173(3-4), 197-206.

Zhao, D., Lei, J., Inoue, T., Yamada, A., & Gao, S. S. (2006). Deep structure and origin of the Baikal rift zone. Earth and Planetary Science Letters, 243(3-4), 681-691.

Zhu R X, Xu Y G, Zhu G, et al. (2012) Destruction of the North China Craton. Sci China Earth Sci, 55: 1565–1587, doi: 10.1007/s11430-012-4516-y

Zorin, Y. A., Kozhevnikov, V. M., Novoselova, M. R., & Turutanov, E. K. (1989). Thickness of the lithosphere beneath the Baikal rift zone and adjacent regions. Tectonophysics, 168(4), 327-337.

Zorin, Y. A., Turutanov, E. K., Mordvinova, V. V., Kozhevnikov, V. M., Yanovskaya, T. B., & Treussov, A. V. (2003). The Baikal rift zone: the effect of mantle plumes on older structure. Tectonophysics, 371(1-4), 153-173.

Zorin, Y. A., Novoselova, M. R., Turutanov, E. K., & Kozhevnikov, V. M. (1990). Structure of the lithosphere of the Mongolian-Siberian mountainous province. Journal of Geodynamics, 11(4), 327-342.

Zonenshain, L. P., & Savostin, L. A. (1981). Geodynamics of the Baikal rift zone and plate tectonics of Asia. Tectonophysics, 76(1-2), 1-45.

# IV. CRUSTAL STRUCTURE IN THE MALAWI AND LUANGWA RIFT ZONES AND ADJACENT AREAS

## ABSTRACT

Stacking over 2500 P-to-S receiver functions recorded by 34 broadband seismic stations that we installed in the vicinity of the Malawi and Luangwa rift zones (MRZ and LRZ, respectively) and gravity modeling reveal significant crustal thickness and $V_p/V_s$ variations. The resulting crustal stretching factor is about 1.1 for the MRZ, which is significantly lower than that observed in the magmatic eastern branch of the East African rift system (EARS), and is consistent with the general absence of volcanism in the MRZ. The southern MRZ shows a high crustal $V_p/V_s$ of 1.81 or greater and may indicate the existence of partial melting. Abnormally low $V_p/V_s$ values between 1.69-1.71 are observed along the western boundary of the northern MRZ and are attributable to $CO_2$ suffusion of rift boundary faults. The LRZ shows negligible crustal thinning and normal $V_p/V_s$, suggesting that crustal post-rifting healing is nearly completed.

## 1. INTRODUCTION

Continental rifts are widely recognized as linear zones where the entire lithosphere has been pulled apart under extension (Sengor & Burke, 1978). One of the most common features in continental rifts is basaltic volcanism, which originates from either partial melting in the lithosphere or doming convection from the sub-lithospheric mantle (Sengor & Burke, 1978). A recent ambient noise tomographic (ANT) study

(Wang et al., 2019) suggests that, in continental rifts, the magnitude of crustal thinning has a close relationship with the development of rift-related volcanisms. Different from most of the mature segments of the East Africa Rift System (EARS) which have been studied extensively using various techniques, the non-volcanic young Malawi rift and the Mesozoic Luangwa rift have been inadequately investigated. Consequently, the magnitude and extent of crustal deformation, the existence of partial melting or mafic intrusion in the crust, and important characteristics such as the depth penetration and possible $CO_2$ suffusion of the seismically active boundary faults, remain enigmatic.

Laboratory investigations of crustal rock samples (Holbrook et al., 1992) suggest that under average crustal temperature and pressure conditions, felsic, intermediate, and mafic rocks have $V_p/V_s$ values of smaller than 1.76, between 1.76 and 1.81, and greater than 1.81, respectively. While the existence of crustal partial melting and intensive diking can increase the $V_p/V_s$ (e.g., Liu & Gao, 2010; Reed et al., 2014), an increasing number of mineral physical and observational studies have suggested that $CO_2$ released from the mantle through deep and steep lithospheric faults can significantly reduce crustal $V_p/V_s$ (Julian et al., 1998; Lee et al., 2016; Parmigiani et al., 2016; Roecker et al., 2017). Therefore, observations of $V_p/V_s$ values that are below the normal felsic rock value of 1.76 may suggest the presence of mantle derived $CO_2$, and that of lithospheric faults acting as conduits for the $CO_2$.

In this study, we present measurements from a joint receiver function and gravity study using recently recorded broadband seismic and gravity data that we collected as part of an interdisciplinary investigation (Gao et al., 2013) to unveil the crustal

characteristics and impact of $CO_2$ and partial melting on $V_p/V_s$ beneath the Malawi and Luangwa rift zones (MRZ and LRZ, respectively) and adjacent areas.

## 2. TECTONIC SETTING

The Cenozoic MRZ is the southernmost segment of the amagmatic western branch of the EARS. It separates the Nubian plate and the Rovuma microplate (Figure 1) and originated approximately 14 Ma (Roberts et al., 2012). The Rungwe Volcanic Province located at the northern tip of the rift zone is the only volcanic province within the MRZ (Ebinger et al., 1993). A kinematic GPS study (Saria et al., 2014) indicated that the spreading rate between the Nubian plate and the Rovuma microplate decreases gradually from the northern tip (2.2 mm/yr) to the southern tip (0.8 mm/yr) of the MRZ. Broadband seismic studies using the same data set used by this study have shown that there is a normal mantle transition zone thickness (Reed et al., 2016) and a NE-SW oriented seismic azimuthal anisotropy (Reed et al., 2017) under the rift, suggesting that there is no significant rift-related mantle flow and detectable influence of an active plume in the vicinity of the mantle transition zone. Previous geodynamic modeling studies also inferred a lack of significant thermal upwelling from the lower mantle beneath the MRZ, and favor an upper mantle origin of rifting (Stamps et al., 2014; 2015). Relative to the mantle, the crust beneath most part of the MRZ has been inadequately studied. A recent receiver function study for the northern MRZ and the Rungwe Volcanic Province (Borrego et al., 2018) suggests a bulk felsic to intermediate crustal composition and small

variation of crustal thickness, and concludes that crustal thinning in the northern MRZ is highly focused beneath the center of the rifted basin.

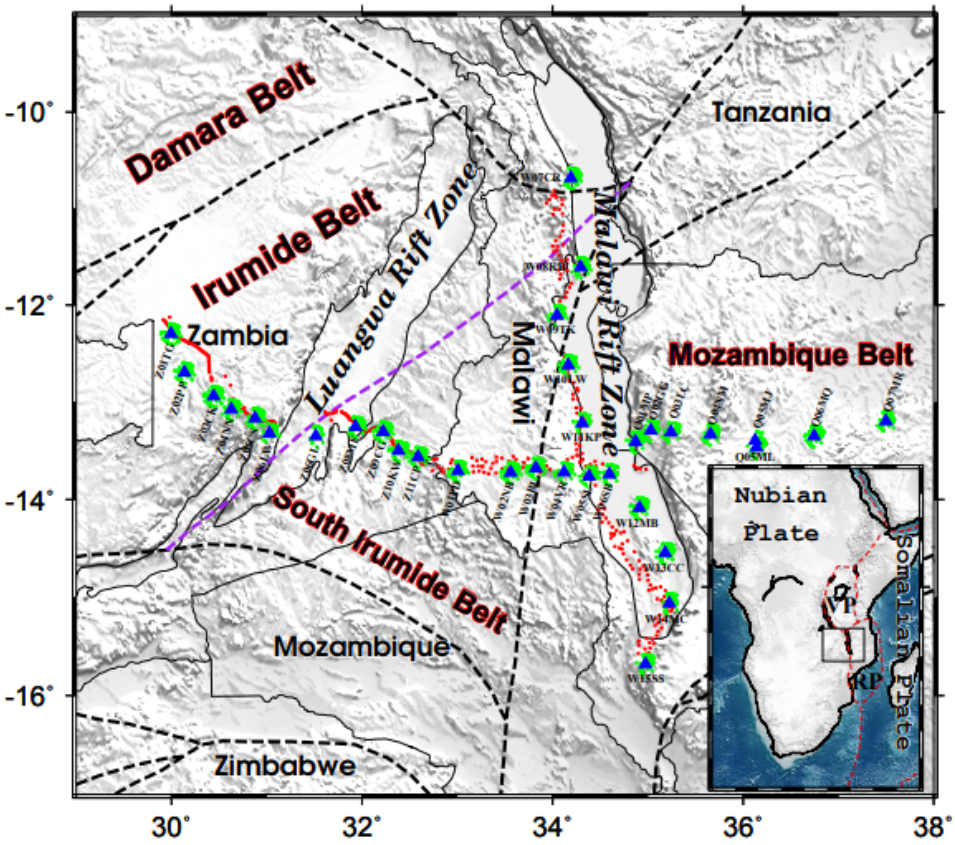


Figure 1 Topographic map of the study area showing the distribution of seismic stations (blue triangles) used in the study and major tectonic features. The red dots indicate the locations of gravity data used in this study, and the green dots are ray-piercing points of P-to-S conversions at the depth of 41.5 km. The dashed lines show the tectonic boundaries, among which the purple dashed line is the Mwembeshi Shear Zone. The rectangle in the inset map indicates the study area

Another major tectonic feature in East Africa is the Permo-Triassic LRZ, which is considered to be a component of the southwestern branch of the EARS (Banks et al.,

1995; Fritz et al., 2013). The Luangwa rifting started in earliest Permian times and ended in the Triassic (Banks et al., 1995; Daly et al., 1989). The southwestern segment of the LRZ follows the ENE-trending Mwembeshi Shear Zone, which separates the Proterozoic Irumide Belt and the South Irumide Belts (SIB), while its northeastern portion is situated in the Irumide Belt (Figure 1). Geochronological studies by Johnson et al. (2005; 2006) indicate that different magmatic events resulted in a significant distinction of the crustal characteristics between these two neighboring orogenic belts. The Mwembeshi Shear Zone separates the lithosphere between the Irumide Belt and SIB, which is evidenced by the observation of an electrically conductive discontinuity in the mantle (Sarafian et al., 2018). This conductive discontinuity might represent a suture zone which is a result of collision between two lithospheric fragments after subduction of an oceanic slab beneath the Irumide Belt (Johnson et al., 2007; Sarafian et al., 2018). Previous integrated studies consider that the left lateral movement on the Mwembeshi Shear Zone dominated the development of the LRZ (Banks et al., 1995; Daly et al., 1989; Orpen et al., 1989). However, this suture zone has not been detected by previous seismological studies (Kachingwe et al., 2015).

## 3. DATA AND METHODS

The teleseismic (epicentral distance ranging from 30° to 180°) data used in the study were recorded by 34 stations (Figure 1) that we installed in Malawi, Mozambique, and Zambia over a 2-year period (2012 - 2014) as a component of the SAFARI (Seismic Arrays for African Rift Initiation; Gao et al., 2013) project. To balance the quality and

quantity of the selected data, a variable cut-off magnitude (Mc) was set by Mc=5.2+(Δ−30.0)/(180.0−30.0)−D/700.0 where Δ and D are the epicentral distance in degree and focal depth in kilometer, respectively (Liu and Gao, 2010). A band-pass filter with a frequency range between 0.04-0.8 Hz was applied to the seismograms, which were windowed 20 s before and 260 s after the theoretical first P-wave arrival based on the IASP91 Earth model (Kennett & Engdahl, 1991). If the signal to noise ratio (S/N) of the first arrival on the vertical component was greater than 4.0, the filtered seismograms were selected to generate P-to-S receiver functions (RFs) following the procedure of Ammon (1991) with a water level value of 0.03. The resulting P-to-S RFs for each of the stations were inspected visually to reject the ones without a clear first 110 P-arrival in the first 2 second window. A total of 2504 high-quality radial RFs from 311 events were selected for determining crustal thickness (H) and $V_p/V_s$ ($\kappa$).

### 3.1. H- $\kappa$ STACKING

Following the H- $\kappa$ stacking procedure of Zhu & Kanamori (2000), the selected RFs were moveout corrected and stacked to grid-search for the optimal pair of the crustal thick ness and $V_p/V_s$, which corresponds to the maximum stacking amplitude. In this study, a crustal mean P-wave velocity of 6.1 km/s was chosen for the H- $\kappa$ stacking, which is consistent with the IASP91 Earth model. Subsequently, following a bootstrap resampling procedure (Efron & Tibshirani, 1986), the mean and standard deviation of the measurements for each station were calculated.

A delay time of approximately 0.4s of the first arrivals and strong multiple reflections in the RFs at one of the stations (Z06GL) located in the LRZ suggest the

presence of a loose sedimentary layer (Yu et al., 2015). Such strong reverberations can mask the P-to-S converted phases from the Moho. For this station, we applied a resonance-removal filter (Yu et al., 2015) to isolate the P-to-S converted phases from the Moho.

### 3.2. RF MIGRATION

To produce a spatially continuous image of the Moho, we migrated the RFs and projected them into a rift orthogonal (W-E) and a rift parallel (S-N) profile, respectively. To produce the cross-sections, the RF raypaths were traced three-dimensionally using an assumed mean crustal $V_p$ of 6.1 km/s and the optimal $V_p/V_s$ value for each station obtained from H-$\kappa$ stacking. We then divided the 25-55 km depth range of the Earth along the profile into rectangular blocks of 1° (longitude for the W-E profile, and latitude for the S-N profile) by 1 km (vertical) with a horizontal and vertical moving step of 0.1° and 0.1 km, respectively. The mean amplitude of the RFs in each of the blocks was calculated and the stacked RFs were normalized by the maximum amplitude in the 25-55 km depth range.

### 3.3. RESIDUAL OIL EFFECT

Bouguer gravity anomaly data consisting of approximately 15,000 stations within the study area were obtained from the National Geospatial and Imaging Agency (NGIA) and detailed surveys by Matende (2013). To remedy the relatively large (greater than 4 km) spacing of the NGIA data in most areas, a detailed gravity survey by Matende (2013) collected data between 1 and 2 kilometers along major roads in Zambia and south ern

Malawi. These new data were processed to complete Bouguer gravity anomalies using the 1967 international gravity formula, sea level as a datum and 2.67 g/cm$^3$ as a Bouguer reduction density, and 1-kilometer DEM to determine terrain corrections. The combined data set was used to create two gravity models that followed the trend of the broadband seismic stations (Figure 1).

The two-dimensional gravity models were constructed using GM-SYS software. Since forward gravity modeling is intrinsically non-unique, constraints were used to determine a better resolved model. Results from previous geological studies (Boniface & Appel, 2017; De Waele et al., 2008; Hansen, 2003) and mapping (Bloomfield & Mason, 1966; Thieme & Johnson, 1975) were used to determine the surface geology and to estimate potential upper crustal bodies. The H- $\kappa$ stacking results for the crustal thickness and $V_p/V_s$ determined from this study were used to constrain crustal thickness and density variations. There were no density measurements or seismic refraction surveys in either the MRZ or LRZ, so the densities were estimated from other gravity studies in the EARS (e.g., Mickus et al., 2007; Simiyu & Keller, 2001; Tesha et al., 1997). The location, geometries and densities of the various bodies were varied by 15% during the modeling process from our initial model.

## 4. RESULTS

Robust P-to-S arrivals are obtained from the migrated RFs (Figure 2), enabling reliable determinations of crustal thickness and $V_p/V_s$ beneath the vast majority of the stations.

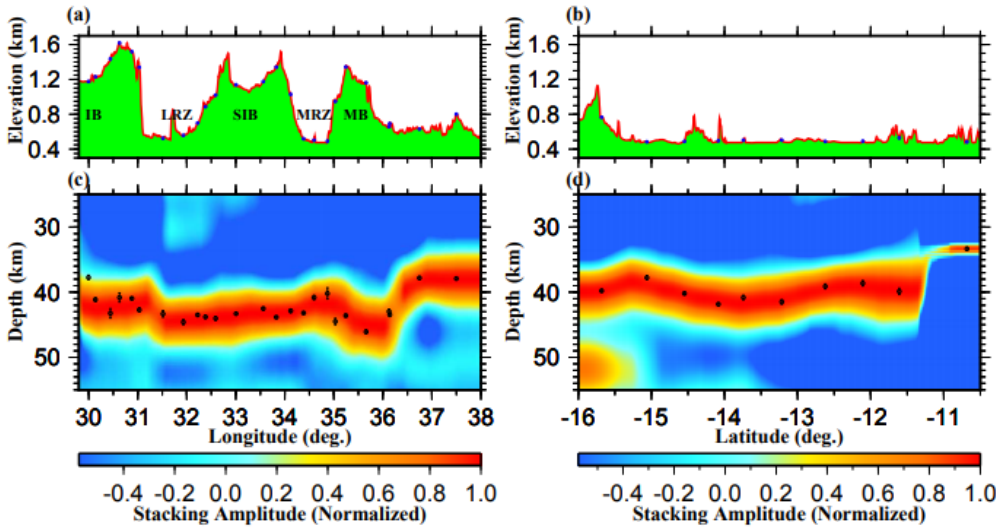


Figure 2 Surface elevation (top panels) and migrated receiver function profiles (bottom panels) along rift-orthogonal (left panels) and rift parallel (right panels) profiles. The black dots indicate results from H-κ stacking.

.

### 4.1. CRUSTAL THICKNESS AND $V_P/V_S$ FROM H-$\kappa$ STACKING

The resulting crustal thicknesses vary from 33.4 km beneath the northern part of the MRZ to 46.1 km beneath the Mozambique belt with an average of 41.5±2.7 km (Figure 3a), and the $V_p/V_s$ values range from 1.69 to 1.84 with 1.67 a mean value of 1.75±0.04 (Figure 3b). The measurements are in general consistent with results from the several stations along the two profiles (Borrego et al., 2018; Kachingwe et al., 2015). Along the rift-orthogonal profile, the crustal thickness in the MRZ is 2-3 km thinner than the surrounding orogenic belts (Figure 2a and 3a), leading to a β (stretching) factor of about 1.1, which is significantly lower than mature segments of continental rifts. The Mozambique Belt has an average thickness of 42.3±2.7 km and $\kappa$ of 1.78±0.04. The mean crustal thickness of the SIB is 43.6±0.6 km, while the $V_p/V_s$ measurements have a

mean value of 1.75±0.01. The crustal thickness observed beneath both the Mozambique Belt and SIB is consistent with the results from a recent ANT study (Wang et al., 2019). H-$\kappa$ stacking from 6 stations in the Irumide Belt leads to a mean crustal thickness of 41.1±1.9 km and $V_p/V_s$ of 1.73±0.03. For the two stations situated in the LRZ, the crustal thickness is 43.3 km at Z06GL and 44.6 km at Z08MF, and the $V_p/V_s$ is 1.75 at both stations.

Along the rift-parallel profile, the averaged crustal thickness is 39.6±2.6 km (Figure 3a). The thinnest crust (33.4 km) was found beneath Station W07CR at the northern end of the profile, while the thickest crust (43.2 km) was observed at Station Z03 in the central part of the MRZ (Figure 3a). The resulting $V_p/V_s$ values observed beneath MRZ fall within the range of 1.69-1.84 with an average of 1.74±0.05 (Figure 3b). Small $V_p/V_s$ values were revealed at 6 stations (W07CR, W08KB, W09TK, W05SL, W11KP, and W10LW) in the northern half of the S-N profile, ranging from 1.69 to 1.72, with a mean of 1.71±0.01.

## 4.2. MOHO DEPTH VARIATION FROM MIGRATED RFS

The spatial variation of crustal thickness and its correspondence with surface elevation can be clearly observed on the migrated and laterally smoothed RF profiles (Figure 2). Along the rift-orthogonal profile (Figures 2a and 2c), the western boundary of the LRZ, which is also approximately the boundary between the Irumide Belt and the SIB, separates the LRZ with a thick crust and the Irumide Belt with relatively thin crust. Contrasting to the commonly observed correspondence between thicker crust and higher elevations, the Irumide Belt, which has a thinner crust, is characterized by an elevation

that is more than 1 km higher than the LRZ. Additionally, although the Irumide Belt and the SIB have similar elevations, the crust beneath the latter is a few km thicker.

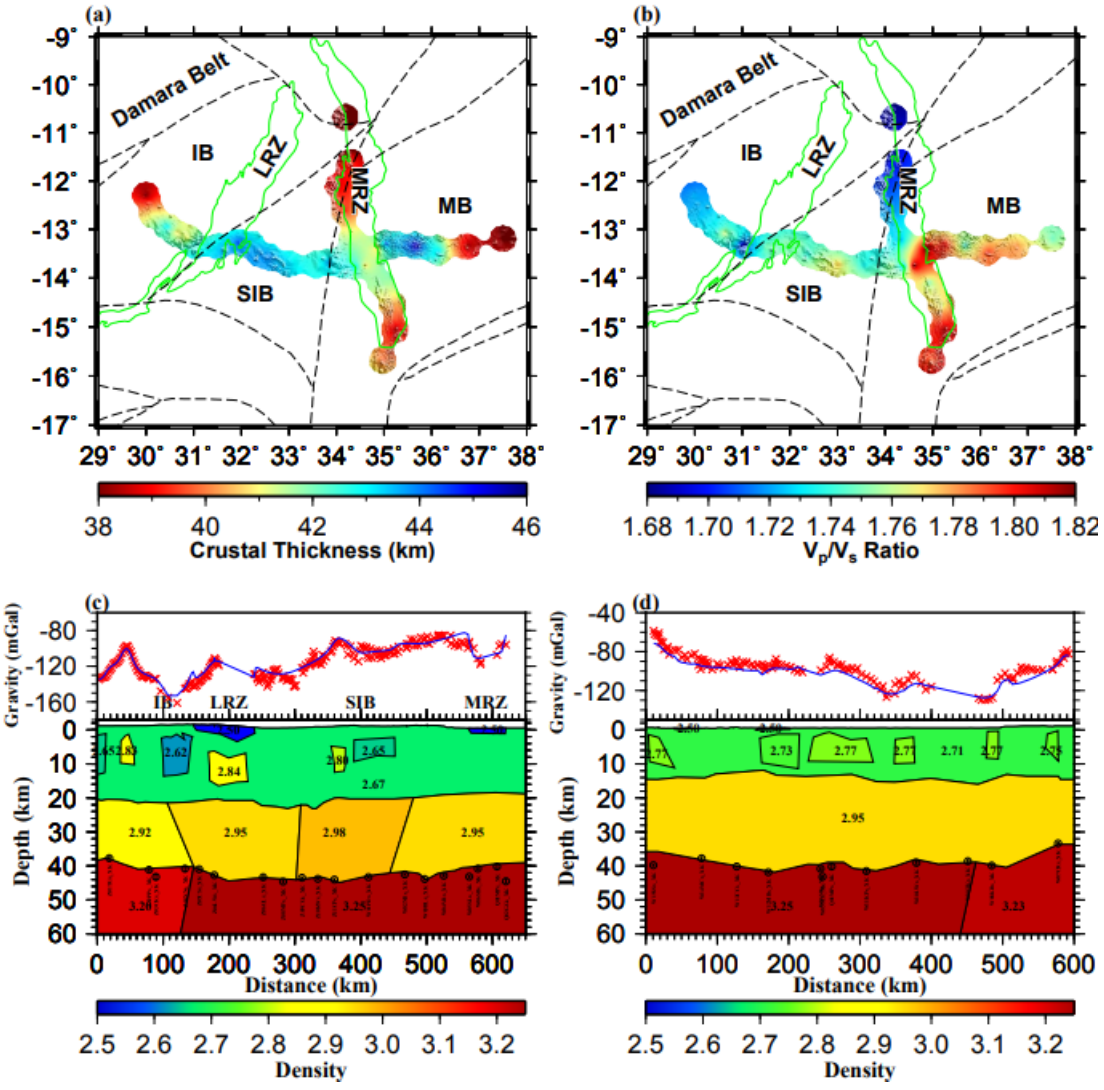


Figure 3 (a). Distribution of resulting crustal thickness. (b). Resulting $V_p/V_s$ measurements. Results of modeling of gravity anomaly data along the rift orthogonal profile (c) and the rift-parallel profile (d). Red crosses and solid line represent observed and calculated Bouguer gravity anomalies, respectively. Densities are in g/cm$^3$. Black open circles with error bars indicate results from H-κ stacking

A different relationship between crustal thickness and surface elevation is revealed in the eastern half of the rift-orthogonal profile, where a thicker crust corresponds to a higher elevation. For instance, the MRZ, which has the lowest elevation in the study area, corresponds to a crustal thinning of a few kilometers relative to the adjacent SIB, and the high elevation area on the Mozambique Belt adjacent to the MRZ is characterized by a thick crust. A sudden thinning of the crust further east corresponds to a significant elevation reduction.

The along-rift variation of crustal thickness is delineated by the migrated RFs (Figure 2d). The major features include a crustal thickening at the high-elevation southern terminus of the MRZ, as well as a sudden crustal thinning beneath the northern end of the profile. Caution must be taken that for stations northern of 14°S, the stations were located on the western edge of the MRZ, while the rest of the stations along the NS profile were approximately in the axial area (Figure 1). Therefore, if the area with the maximum crustal thinning is limited underneath the surface expression of the rift, the observed crustal thickness beneath the northern stations might be larger than the axial area. However, it is worth to realize that the difference in the resulting crustal thickness between Station W05SL, which, similar to the rest of the northern stations, was on the rift shoulder, and Station W06SB, which was approximately in the axial area, is less than 3 km.

### 4.3. RESULTS FROM GRAVITY MODELING

Figure 3c shows an east-west trending model that starts within the Irumide Belt and crosses LRZ, SIB and MRZ. Of interest is that there is no obvious crustal thinning or

magmatic underplating beneath the LRZ which was constrained by the receiver function results. However, in order to explain the long wavelength, low amplitude gravity maximum over the LRZ without crustal thinning, some type of density increase must be included beneath the LRZ. We used a slightly higher density lower crust (relative to the Irumide Belt at the western end of the profile) combined with a higher density body within the upper crust. The $V_p/V_s$ values do not show an increase under the LRZ so having the entire density increase within the lower crust did not make geophysical sense. Additionally, a higher crustal density region was required under the SIB as this region is associated with a relative gravity maximum. Commonly, Proterozoic terranes are associated with thicker, denser lower crust, however this region has been subjected to two adjacent rifting events in the Permian-Triassic and the current rifting in Malawi.

The upper mantle density beneath the region between the LRZ and the MRZ has relatively average densities (3.25 $g/cm^3$) with no gravity or seismic evidence for a lower density upper mantle seen in other portions of the East African Rift (Mickus et al., 2007; Simiyu & Keller, 2001). The lower density crust and upper mantle under the Irumide Belt are necessary to fit the more felsic and thinner crust, as well as the high elevation, which are consistent with the more felsic lithologies that are seen in the surface rocks (De Waele et al., 2009).

The north-south gravity model (Figure 3d) indicates slightly thinner crust of approximately 39 km on the north and south ends of the model compared to an average of 42 km for the rest of the model. The crustal thickness in northern Malawi agrees with the thicknesses (39 km) to the north of the profile under the Rungwe Volcanic Province (Borrego et al., 2018). While this region is associated with a low velocity zone in the

mantle (Borrego et al., 2018), there is no evidence of high $V_p/V_s$ values and/or crustal thinning associated with rifting and the presence of partial melt. The slightly thinner crust in southern Malawi is associated with higher $V_p/V_s$ values.

# 5. DISCUSSION

## 5.1. CONSTRAINTS ON CRUSTAL MAGMATIC INTRUSION AND PARTIAL PELTING BENEATH THE MRZ

Borrego et al. (2018) observed negligible crustal thinning beneath the shoulder of the northern MRZ, suggesting that crustal thinning in the northern MRZ must be highly focused beneath the centers of rift basin segments. In this study, a relatively flat Moho (39.6±2.6 km) was found under most stations in the MRZ including the central and southern parts of the MRZ. This seems to indicate that, relative to other parts of the EARS, crustal thinning within the MRZ is relatively minor even within the central portion of the MRZ. This relatively low magnitude crustal thinning beneath the MRZ is consistent with the absence of volcanism on the surface except for the Rungwe Volcanic Province.

In contrast to the small variations of crustal thickness along the axis of the MRZ, the resulting $V_p/V_s$ values observed within the MTZ varies greatly from 1.69 at the northernmost part to 1.85 in the central part of the MRZ (Figure 3b), implying significant along-rift variations of crustal composition, degree of partial melting, or temperature. The high $V_p/V_s$ ($\geq$ 1.81) determined at stations Q01MP, W06SB, and W14MC (Figure 3b), which are situated in the central and southern parts of the MRZ, implies the possible

existence of magmatic intrusion in the lower crust or partial melting in the crust beneath some areas of the MRZ. High crustal densities and higher than- normal Vs in the crust are expected, if the high $V_p/V_s$ is caused by magmatic intrusion in the crust from mantle. However, the gravity model in this study shows normal crustal densities beneath most parts of the MRZ (Figure 3d). On the other hand, a recent ANT study (Wang et al., 2019) revealed lower-than-normal Vs beneath these areas. All these observations, when combined with the evidence of the absence of crustal thickening from magmatic addition observed in this study (Figure 2b), are inconsistent with the possibility of the presence of magmatic intrusion of high-density mantle material into the crust beneath the central and southern parts of the MRZ.

Broadband seismic studies have observed a normal mantle transition zone thickness (Reed et al., 2016) and NE-SW oriented seismic azimuthal anisotropy which is similar to that observed across the rest of southern Africa (Reed et al., 2017; Silver et al., 2001), suggesting that absence of rifting-related mantle flow beneath the MRZ. These observations suggest that the high $V_p/V_s$ values could be related to partial melting and elevated temperatures induced by lithospheric stretching decompression rather than ascending magma from an active mantle plume.

## 5.2. MAGMA-DERIVED $CO_2$ SUFFUSION OF BOUNDARY FAULTS IN THE NORTHERN MRZ

Anomalously low $V_p/V_s$ values ranging from 1.69 to 1.71 with a mean value of 1.70±0.01 were determined at six stations (W05, W07, W08, W09, W10, and W11) along the western boundary of the MRZ. The most commonly cited cause for such low $V_p/V_s$

values is the presence of rocks with a high silicon content (Christensen, 1996), which, to our knowledge, is not found by previous studies in the study area. A recently proposed alternate mechanism for low $V_p/V_s$ is magma-derived $CO_2$ released from the mantle through deep and steep lithospheric faults (e.g., Foly & Fischer, 2017; Julian et al., 1998; Lee et al., 2016; Parmigiani et al., 2016; Roecker et al., 2017). Parmigiani et al. (2016) suggest that a magmatic volatile phase is prone to migrate from the crystal-rich regions to the crystal-poor parts, and accumulate large volumes of low density bubbles at the roof of the crystal-poor magma reservoir. The deep boundary faults beneath the edges of the rift zones, if they connect to the magma reservoir in the mantle, could be infiltrated by the magma-derived volatiles (Foly & Fischer, 2017; Roecker et al., 2017), which can affect the pore-fluid compressibility, and consequently, reduce the crustal $V_p/V_s$ (Julian et al., 1998).

Considering the enormous quantity of recently recognized $CO_2$ outgassing along the faults in the EARS (Lee et al., 2016) and similar observations of low $V_p/V_s$ values along the edges of the EARS in northern Tanzania and southern Kenya (Roecker et al., 2017), we speculate that a viable explanation for the anomalously low $V_p/V_s$ observed in the northern part of the MRZ is $CO_2$ suffusion of deep rift boundary faults.

## 5.3. POSSIBLE EXISTENCE OF A MESOPROTEROZOIC SUTURE ZONE BENEATH THE MWEMBESHI SHEAR ZONE AND POST-RIFTING HEALING OF THE LRZ

Along the rift-orthogonal profile, if we assume uniform densities for the crust and upper mantle, the relationship between crustal thicknesses determined by the receiver function analysis and surface topography could generally fit an Airy isostatic model

except for the LRZ and the Irumide Belt to the west (Figure 2b). The Irumide Belt which has the highest elevation is associated with crust that is 37.7 km thick, which is obviously thinner than that under the SIB which has a lower elevation. Simple calculations based on Airy's isostatic model suggest that, relative to the SIB, the crust beneath the Irumide Belt must be underlain by a lower density upper mantle and/or lower density crust. While a variety of gravity models under the Irumide Belt were attempted, the final model shown in in Figure 3c best fit the observed gravity data, the receiver function models and the low $V_p/V_s$ values (Figure 3b). This model includes both relatively lower upper mantle and lower crustal densities than the surrounding terranes.

The density contrast boundary in the gravity model (which is approximately located at 100-130 km along the horizontal axis in Figure 3c) is located at the boundary between the Irumide Belt and the SIB (Figure 1) and might represent the suture zone which is the result of the collision of the two lithospheric fragments after ocean closure occurred during the Irumide Orogeny (Johnson et al., 2007). Previous studies suggested that this suture zone beneath the Mwembeshi Shear Zone dominated the development of the LRZ (Banks et al., 1995; Daly et al., 1989; Orpen et al., 1989). This conclusion is supported by geochronological studies (Johnson et al., 2005; 2006), which found significant difference in metamorphism types and magmatism histories between Irumide Belt and SIB, suggesting that the crust underlying the SIB is not the southward extension of the crust beneath the Irumide Belt. Moreover, a recent magnetotelluric study (Sarafian et al., 2018) observed an electrical conductivity discontinuity in the mantle beneath the Mwembeshi Shear zone, indicating that the tectonic effects of this shear zone might extend through the entire lithosphere.

Unlike the tectonically active MRZ, the resulting crustal thickness beneath the Mesozoic LRZ, the southern part of which was developed in the Mwembeshi Shear Zone, is not significantly thinner than that beneath the adjacent orogenic belts. In spite of the currently higher level of tectonic activity relative to the surrounding areas and the speculation that the LRZ has been reactivated (Banks et al., 1995; Daly et al., 1989; Orpen et al., 1989), the observed negligible crustal thinning and insignificant variation of $V_p/V_s$ beneath the LRZ relative to the surrounding area suggest that post rifting healing of the rifted crust beneath the LRZ has completed since the cessation of the rifting event.

## 6. CONCLUSIONS

Crustal thickness and $V_p/V_s$ beneath 34 SAFARI stations located along two profiles in the vicinity of the MRZ and LRZ were imaged by stacking 2504 highquality RFs and gravity modeling. The crustal thickness measurements are generally consistent with sparsely spaced previous measurements. The new observations show that relative to the adjacent orogenic belts, the crust beneath the MRZ is thinned by about 3 km. This low magnitude crustal stretching is consistent with the absence of volcanisms in the main portions of the MRZ. Some areas in the MRZ show a high crustal $V_p/V_s$ of 1.81 or greater, which, when combined with the observations from other broadband seismic studies and gravity modeling, may indicate the existence of partial melting probably associated with lithospheric stretching decompression. One of the most significant observations from this study is the spatially consistent low $V_p/V_s$ measurements in the range of 1.69-1.71 along the western edge of the northern MRZ, which could be

interpreted by the suffusion of magma-derived $CO_2$ into lithospheric normal faults. Moreover, the ancient suture zone beneath the Mwembeshi Shear Zone is represented by a density contrast boundary between the Irumide Belt and the South Irumide Belt. Based on the negligible crustal thinning and insignificant variation of $V_p/V_s$ beneath the LRZ relative to the surrounding area, we propose that post-rifting healing of the rifted crust beneath the LRZ has completed, and the recent reactivation of tectonic activities in the failed rift represents localization of regional strain along preexisting zones of mechanical weakness in the rifted crust.

## ACKNOWLEDGEMENTS

We thank the IRIS DMC for archiving the data used in the study, and the Portable Array Seismic Studies of the Continental Lithosphere Instrument Center for providing equipment and logistical support. All the data used in the study were obtained from the IRIS DMC (last accessed: August 2018). Field assistance provided by Shane Ingate, Patrick R. N. Chindandali, Belarmino Massingue, Hassan Mdala, and Daniel Mutamina, as well as by various government agencies and universities in Malawi, Mozambique, and Zambia are greatly appreciated. This study was partially supported by the U.S. National Science Foundation under grants 1009946 and 1460516 to S.G. and K.L., and by the China Scholarship Council to M.S. under award 201508230075.

# REFERENCES

Ammon, C. J. (1991). The isolation of receiver effects from teleseismic Pwaveforms. Bulletin of the Seismological Society of America, 81(6), 2504-2510.

Banks, N. L., Bardwell, K. A., & Musiwa, S. (1995). Karoo rift basins of the Luangwa Valley, Zambia. Geological Society, London, Special Publications, 80(1), 285-295. https://doi.org/10.1144/GSL.SP.1995.080.01.13

Bloomfield, S., & Mason, T., 1966, Geological Map of Malawi. Geological Survey of Malawi, 1966.

Boniface, N., & Appel, P. (2018). Neoproterozoic reworking of the Ubendian Belt crust: Implication for an orogenic cycle between the Tanzania Craton and Bangweulu Block during the assembly of Gondwana. Precambrian Research, 305, 358-385. https://doi.org/10.1016/j.precamres.2017.12.011

Borrego, D., Nyblade, A. A., Accardo, N. J., Gaherty, J. B., Ebinger, C. J., Shillington, D. J., et al. (2018). Crustal structure surrounding the northern Malawi rift and beneath the Rungwe Volcanic Province, East Africa. Geophysical Journal International, 215(2), 1410-1426. https://doi.org/10.1093/gji/ggy331

Christensen, N. I. (1996). Poisson's ratio and crustal seismology. Journal of Geophysical Research: Solid Earth, 101(B2), 3139-3156. https://doi.org/10.1029/95JB03446

Daly, M. C., Chorowicz, J., & Fairhead, J. D. (1989). Rift basin evolution in Africa: the influence of reactivated steep basement shear zones. Geological Society, London, Special Publications, 44(1), 309-334. https://doi.org/10.1144/GSL.SP.1989.044.01.17

De Waele, B., Fitzsimons, I. C. W., Wingate, M. T. D., Tembo, F., Mapani, B., & Belousova, E. A. (2009). The geochronological framework of the Irumide Belt: A prolonged crustal history along the margin of the Bangweulu Craton. American Journal of Science, 309(2), 132-187. https://doi.org/10.2475/02.2009.03

De Waele, B., Johnson, S. P., & Pisarevsky, S. A. (2008). Palaeoproterozoic to Neoproterozoic growth and evolution of the eastern Congo Craton: its role in the Rodinia puzzle. Precambrian Research, 160(1-2), 127-141. https://doi.org/10.1016/j.precamres.2007.04.020

Ebinger, C. J., Deino, A. L., Tesha, A. L., Becker, T., & Ring, U. (1993). Tectonic controls on rift basin morphology: evolution of the Northern Malawi (Nyasa) Rift. Journal of Geophysical Research: Solid Earth, 98(B10), 17821-17836. https://doi.org/10.1029/93JB01392

Efron, B., & Tibshirani, R. (1986). Bootstrap methods for standard errors, confidence intervals, and other measures of statistical accuracy. Statistical science, 54-75.

Foley, S. F., & Fischer, T. P. (2017). An essential role for continental rifts and lithosphere in the deep carbon cycle. Nature Geoscience, 10(12), 897. https://doi.org/10.1038/s41561-017-0002-7

Fritz, H., Abdelsalam, M., Ali, K. A., Bingen, B., Collins, A. S., Fowler, A. R., et al. (2013). Orogen styles in the East African Orogen: a review of the Neoproterozoic to Cambrian tectonic evolution. Journal of African Earth Sciences, 86, 65-106. https://doi.org/10.1016/j.jafrearsci.2013.06.004

Gao, S. S., Liu, K. H., Reed, C. A., Yu, Y., Massinque, B., Mdala, H., et al. (2013). Seismic arrays to study African rift initiation. Eos, Transactions American Geophysical Union, 94(24), 213-214. https://doi.org/10.1002/2013EO240002

Hanson, R. E. (2003). Proterozoic geochronology and tectonic evolution of southern Africa. Geological Society, London, Special Publications, 206(1), 427-463. https://doi.org/10.1144/GSL.SP.2003.206.01.20

Holbrook,W. S., Mooney,W. D., & Christensen, N. I. (1992). The seismic velocity structure of the deep continental crust. Continental lower crust, 23, 1-43.

Johnson, S. P., De Waele, B., & Liyungu, K. A. (2006). U-Pb sensitive highresolution ion microprobe (SHRIMP) zircon geochronology of granitoid rocks in eastern Zambia: Terrane subdivision of the Mesoproterozoic Southern Irumide Belt. Tectonics, 25(6). https://doi.org/10.1029/2006TC001977

Johnson, S. P., De Waele, B., Tembo, F., Katongo, C., Tani, K., Chang, et al., (2007). Geochemistry, geochronology and isotopic evolution of the Chewore-Rufunsa Terrane, Southern Irumide Belt: a Mesoproterozoic continental margin arc. Journal of Petrology, 48(7), 1411-1441. https://doi.org/10.1093/petrology/egm025

Johnson, S. P., Rivers, T., & DeWaele, B. (2005). A review of the Mesoproterozoic to early Palaeozoic magmatic and tectonothermal history of south-central Africa: implications for Rodinia and Gondwana. Journal of the Geological Society, 162(3), 433-450. https://doi.org/10.1144/0016-764904-028

Julian, B. R., Pitt, A. M., & Foulger, G. R. (1998). Seismic image of a $CO_2$ reservoir beneath a seismically active volcano. Geophysical Journal International, 133(1), F7-F10. https://doi.org/10.1046/j.1365-246X.1998.1331540.x

Kachingwe, M., Nyblade, A., & Julia, J. (2015). Crustal structure of Precambrian terranes in the southern African subcontinent with implications for secular variation in crustal genesis. Geophysical Journal International, 202(1), 533-547. https://doi.org/10.1093/gji/ggv136

Kennett, B. L. N., & Engdahl, E. R. (1991). Traveltimes for global earthquake location and phase identification. Geophysical Journal International, 105(2), 429- 465. https://doi.org/10.1111/j.1365-246X.1991.tb06724.x

Lee, H., Muirhead, J. D., Fischer, T. P., Ebinger, C. J., Kattenhorn, S. A., Sharp, Z. D., & Kianji, G. (2016). Massive and prolonged deep carbon emissions associated with continental rifting. Nature Geoscience, 9(2), 145. https://doi.org/10.1038/ngeo2622

Liu, K. H., & Gao, S. S. (2010). Spatial variations of crustal characteristics beneath the Hoggar swell, Algeria, revealed by systematic analyses of receiver functions from a single seismic station. Geochemistry, Geophysics, Geosystems, 11(8). https://doi.org/10.1029/2010GC003091

Matende, K. N. (2015). Magmatic under-plating beneath the Luangwa Rift Valley, Zambia? (Doctoral dissertation, Oklahoma State University).

Mickus, K., Tadesse, K., Keller, G. R., & Oluma, B. (2007). Gravity analysis of the main Ethiopian rift. Journal of African Earth Sciences, 48(2-3), 59-69. https://doi.org/10.1016/j.jafrearsci.2007.02.008

Njinju, E., Atekwana, E., Stamps, D., Abdelsalam, M. Atekwana, E., Mickus, K., Kolawole, F., and Hyalugwe, V., 2018, Submitted to Tectonophysics.

Orpen, J. L., Swain, C. J., Nugent, C., & Zhou, P. P. (1989). Wrench-fault and half-graben tectonics in the development of the Palaeozoic Zambezi Karoo Basins in Zimbabwe - the ”Lower Zambezi” and ”Mid-Zambezi” basins respectively - and regional implications. Journal of African Earth Sciences (and the Middle East), 8(2- 4), 215-229. https://doi.org/10.1016/S0899-5362(89)80026-0

Parmigiani, A., Faroughi, S., Huber, C., Bachmann, O., & Su, Y. (2016). Bubble accumulation and its role in the evolution of magma reservoirs in the upper crust. Nature, 532(7600), 492. https://doi.org/10.1038/nature17401

Roecker, S., Ebinger, C., Tiberi, C., Mulibo, G., Ferdinand-Wambura, R., Mtelela, K., et al (2017). Subsurface images of the Eastern Rift, Africa, from the joint inversion of body waves, surface waves and gravity: investigating the role of fluids in early-stage continental rifting. Geophysical Journal International, 210(2), 931-950. https://doi.org/10.1093/gji/ggx220

Reed, C. A., Almadani, S., Gao, S. S., Elsheikh, A. A., Cherie, S., Abdelsalam, M. G., et al. (2014). Receiver function constraints on crustal seismic velocities and partial melting beneath the Red Sea rift and adjacent regions, Afar Depression. Journal of Geophysical Research: Solid Earth, 119(3), 2138-2152. https://doi.org/10.1002/2013JB010719

Reed, C. A., Liu, K. H., Chindandali, P., Massingue, B., Mdala, H., Mutamina, D., et al. (2016). Passive rifting of thick lithosphere in the southern East African Rift: Evidence from mantle transition zone discontinuity topography. Journal of Geophysical Research: Solid Earth, 121(11), 8068-8079. https://doi.org/10.1002/2016JB013131

Reed, C. A., Liu, K. H., Yu, Y., & Gao, S. S. (2017). Seismic anisotropy and mantle dynamics beneath the Malawi Rift Zone, East Africa. Tectonics, 36(7), 1338-1351. https://doi.org/10.1002/2017TC004519

Roberts, E. M., Stevens, N. J., O'Connor, P. M., Dirks, P. H. G. M., Gottfried, M. D., Clyde, W. C., et al. (2012). Initiation of the western branch of the East African Rift coeval with the eastern branch. Nature Geoscience, 5(4), 289. https://doi.org/10.1038/ngeo1432

Sarafian, E., Evans, R. L., Abdelsalam, M. G., Atekwana, E., Elsenbeck, J., Jones, A. G., & Chikambwe, E. (2018). Imaging Precambrian lithospheric structure in Zambia using electromagnetic methods. Gondwana Research, 54, 38-49. https://doi.org/10.1016/j.gr.2017.09.007

Saria, E., Calais, E., Stamps, D. S., Delvaux, D., & Hartnady, C. J. H. (2014). Present-day kinematics of the East African Rift. Journal of Geophysical Research: Solid Earth, 119(4), 3584-3600. https://doi.org/10.1002/2013JB010901

Sengor, A. M & Burke, K. (1978). Relative timing of rifting and volcanism on Earth and its tectonic implications. Geophysical Research Letters, 5(6), 419-421. https://doi.org/10.1029/GL005i006p00419

Silver, P. G., Gao, S. S., Liu, K. H., & Kaapvaal Seismic Group. (2001). Mantle deformation beneath southern Africa. Geophysical Research Letters, 28(13), 2493- 2496. https://doi.org/10.1029/2000GL012696

Simiyu, S. M., & Keller, G. R. (2001). An integrated geophysical analysis of the upper crust of the southern Kenya rift. Geophysical Journal International, 147(3), 543-561. https://doi.org/10.1046/j.0956-540x.2001.01542.x

Stamps, D. S., Flesch, L. M., Calais, E., & Ghosh, A. (2014). Current kinematics and dynamics of Africa and the East African Rift System. Journal of Geophysical Research: Solid Earth, 119(6), 5161-5186. https://doi.org/10.1002/2013JB010717

Stamps, D. S., Iaffaldano, G., & Calais, E. (2015). Role of mantle flow in Nubia-Somalia plate divergence. Geophysical Research Letters, 42(2), 290-296. https://doi.org/10.1002/2014GL062515

Tesha, A. L., Nyblade, A. A., Keller, G. R., & Doser, D. I. (1997). Rift localization in suture-thickened crust: evidence from Bouguer gravity anomalies in northeastern Tanzania, East Africa. Tectonophysics, 278(1-4), 315-328. https://doi.org/10.1016/S0040-1951(97)00110-8

Thieme, J., & Johnson, R., 1975, Geologic Map of Zambia, Zambia Geological Survey.

Wang, T., Feng, J., Liu, K. H., & Gao, S. S. (2019). Crustal structure beneath the Malawi and Luangwa Rift Zones and adjacent areas from ambient noise tomography. Gondwana Research, 67, 187-198. https://doi.org/10.1016/j.gr.2018.10.018

Yu, Y., Song, J., Liu, K. H., & Gao, S. S. (2015). Determining crustal structure beneath seismic stations overlying a low-velocity sedimentary layer using receiver functions. Journal of Geophysical Research: Solid Earth, 120(5), 3208-3218. https://doi.org/10.1002/2014JB011610

Zhu, L., & Kanamori, H. (2000). Moho depth variation in southern California from teleseismic receiver functions. Journal of Geophysical Research: Solid Earth, 105(B2), 2969-2980. https://doi.org/10.1029/1999JB900322

# SECTION

# 2. CONCLUSIONS

In this study, we have imaged MTZ discontinuities beneath the Tanzania Craton (TC), the Eastern and Western Branches of the East Africa Rift System (EARS), southern Africa and northeast Asia. The normal MTZ thickness reveals a lack of significant thermal anomaly in the MTZ beneath most of the Tanzania Craton and the Western Branch. In contrast, a 30 km thinning of the MTZ beneath the Eastern Branch associated with a 50 km apparent depression of the d410 and a 20 km depression of the d660 suggest that the present-day existence of thermal upwelling from either the lower mantle or the uppermost MTZ beneath the northern part of the Eastern Branch. The observed normal MTZ thickness beneath southern Africa suggest that both the cratonic keels and the lower mantle African Superswell have a limited influence on the thermal structure of the MTZ beneath southern Africa. The most major Cenozoic volcanos in northeast China are underlain by a depressed d660 and thickened MTZ, which can be explained by hot and wet upwelling originated from dehydration of subducted Pacific slab. The observed thickened MTZ beneath the BRZ indicates a low temperature around MTZ structure, which rules out the possibility of the active rifting mechanism. In contrast, the presence of the thermal upwelling from lower mantle cross the whole MTZ is proved by the observed abnormally thinned MTZ beneath the Hangay Dome.

The crustal thickness measurements show that relative to the adjacent orogenic belts, the crust beneath the MRZ is thinned by about 3 km. This low magnitude crustal

stretching is consistent with the absence of volcanisms in the main portions of the MRZ. Some areas in the MRZ show a high crustal $V_p/V_s$ of 1.81 or greater, which, when combined with the observations from other broadband seismic studies and gravity modeling, may indicate the existence of partial melting probably associated with lithospheric stretching decompression. One of the most significant observations from this study is the spatially consistent low $V_p/V_s$ measurements in the range of 1.69-1.71 along the western edge of the northern MRZ, which could be interpreted by the suffusion of magma-derived $CO_2$ into lithospheric normal faults. Moreover, the ancient suture zone beneath the Mwembeshi Shear Zone is represented by a density contrast boundary between the Irumide Belt and the South Irumide Belt. Based on the negligible crustal thinning and insignificant variation of $V_p/V_s$ beneath the LRZ relative to the surrounding area, we propose that post-rifting healing of the rifted crust beneath the LRZ has completed, and the recent reactivation of tectonic activities in the failed rift represents localization of regional strain along preexisting zones of mechanical weakness in the rifted crust.

# BIBLIOGRAPHY

Chorowicz, J. (2005). The east African rift system. Journal of African Earth Sciences, 43(1), 379–410. https://doi.org/10.1016/ j.jafrearsci.2005.07.019

Lithgow-Bertelloni, C., Silver, P.G., 1998. Dynamic topography, plate driving forces and the African superswell. Nature395, 269. http://doi.org /10.1038/26212.

Hu, J., Liu, L., Faccenda, M., Zhou, Q., Fischer, K.M., Marshak, S., Lundstrom, C., 2018. Modification of the Western Gondwana craton by plume–lithosphere interac-tion. Nat. Geosci.11, 203–210. https://doi .org /10.1038/s41561-018-0064-1.

Romanowicz, B., Gung, Y., 2002. Superplumes from the core–mantle boundary to the lithosphere: implications for heat flux. Science296, 513–516. http://doi.org/1.1126/science.1069404.

Ni, S., Helmberger, D.V., Tromp, J., 2005. Three-dimensional structure of the African superplume from waveform modeling. Geophys. J. Int.161, 283–294. http://doi.org /10.1111/j.1365-246X.2005.02508.x.

Gao, S.S., Liu, K.H., 2014a. Imaging mantle discontinuities using multiply-reflected P-to-Sconversions. Earth Planet. Sci. Lett.402, 99–106. http://doi.org/10.1016/j.epsl.2013.08.025.

Foulger, G. R., Panza, G. F., Artemieva, I. M., Bastow, I. D., Cammarano, F., Evans, J. R., ... & Yanovskaya, T. B. (2013). Caveats on tomographic images. Terra Nova, 25(4), 259-281.

Gao, S. S., Liu, K. H., Reed, C. A., Yu, Y., Massinque, B., Mdala, H., et al. (2013). Seismic arrays to study African rift initiation. Eos, Transactions American Geophysical Union, 94(24), 213-214. https://doi.org/10.1002/2013EO240002

# VITA

Muchen Sun received his Bachelor of Science degree in Exploration Technology from Northeast Petroleum University, Daqing, China in 2012. Then he joined Dr. Stephen S. Gao's research group in August 2013 and worked as a teaching assistant in Geology and Geophysics program at Missouri University of Science and Technology, Rolla, Missouri. He received his Master of Science degree in Geology and Geophysics in 2014. He continued to pursue his Ph.D. degree in Geology and Geophysics in August 2015. In May 2019, he received his Doctor of Philosophy in Geology and Geophysics from Missouri University of Science and Technology at Rolla, Missouri.